University of Stavanger

Faculty of Science and Technology

MASTER'S THESIS

Study program/Specialization: Petroleum Geosciences Engineering	Spring, 2016 Open
Writer: Diana Carolina Castillo Valencia	…… (Writer's signature)
Faculty supervisor: Nestor Cardozo Charlotte Botter External supervisor(s):	
Title of thesis: Seismic imaging of salt-influenced compressional folds	
Credits (ECTS): 30	
Keywords: Compressional folds Salt detachment Thrust faults Geomechanical modeling Finite strain Seismic imaging	Pages: 108 +enclosure: CD Stavanger, 14th June, 2016

Seismic imaging of salt-influenced compressional folds

by

Diana Carolina Castillo Valencia

Master Thesis

Presented to the Faculty of Science and Technology

The University of Stavanger

The University of Stavanger

June 2016

Acknowledgements

I would like to express my gratitude to my supervisors Nestor Cardozo and Charlotte Botter, who have made this thesis possible, and with their knowledge, experience, and continuous advice added significantly to the project.

I should also acknowledge Stuart Hardy (ICREA, University of Barcelona), who kindly provided the cdem2D code used in this project. Likewise, the software SSPX by Cardozo and Allmendinger (2009) and SeisRoX (NORSAR) were freely available and essential for the project implementation.

I am indebted to the Petroleum Geosciences Engineering Department of the University of Stavanger providing a solid education during my stay here, and I give my sincere thanks to the entire teaching staff.

Most importantly, this accomplishment would not have been possible without the love and patience of my family, who gave me their unfailing support and continuous encouragement throughout these two years of study and through the process of developing and writing this thesis.

Finally, I also appreciate the support and care of my closer friends, who helped me to overcome setbacks and stay focused on my graduate study. I greatly value their friendship and I deeply appreciate their belief in me.

Abstract

Seismic imaging of salt-influenced compressional folds

Diana Carolina Castillo Valencia

University of Stavanger, 2016

Supervisors: Nestor Cardozo

Charlotte Botter

Fold-and-thrust belts (FTB) detaching on salt have a high potential for developing trap structures and host large oil and gas fields. Due to their high structural complexity and often low-quality seismic data, their understanding is limited. Furthermore, the presence of salt adds challenges for seismic imaging because of strong acoustic impedance at the salt boundaries. Hence, seismic characterization of these structures has high uncertainty, giving room to different interpretations. The main objective of this study is to present a methodology to forward model seismic images of compressional folds influenced by a salt layer, and in addition syn-sedimentation, in order to study the evolution of these structures and evaluate acquisition and processing parameters for better seismic imaging and interpretation. The methodology consists of a geomechanical modeling of the FTB using a 2D discrete element method (DEM), finite strain computation in the DEM, update of the base seismic properties of the DEM based on finite strain, and seismic imaging of the DEM using a ray-based pre-stack depth migration (PSDM) algorithm. This workflow is illustrated for a 2D DEM model consisting of a brittle siliciclastic – ductile salt sequence under imposed lateral shortening, which initiates and propagates thrust faulting through the siliciclastic sequence. To investigate the influence of salt and syn-sedimentation, three models are considered: Model 1 with no salt, Model 2 with salt, and Model 3 including salt, and syn-sedimentation. All simulations produce realistic although different FTB geometries. Seismic images are modeling for the pre-

growth/growth interlayered sequence of sandstone and shale for four different wave frequencies from 10 to 40 Hz, and three different illumination directions (specular, right and left side). At 30 Hz and side illumination, the complexity of the larger thrust faults and the geometry and internal organization of syn-sedimentation can be better represented than at the lower 10 Hz frequency images. As a result, by combining several acquisition and processing parameters (illumination direction and wave frequency), it is possible to improve seismic imaging of salt-influenced compressional folds.

Table of Contents

List of Tables

List of Figures

1. Introduction

Salt (evaporites) plays a key role in the deformation style and evolution of fold-and-thrust belts (FTB) (Davis and Engelder 1985; Letouezey et al., 1995; Buttler et al 1987; Jaume and Lillie, 1988; Jackson and Talbot, 1991; Cotton and Koyi, 2000; Costa and Vendeville, 2002; Rowan et al 2004). There are at least 12 FTB around the world that detach over a ductile salt layer (Jackson and Talbot, 1991; Cotton and Koyi, 2000), and most of them have been the subject of multiples studies such as the Appennines (Coward et al., 1999), the central Appalachian (Davis and Engelder, 1985, 1987), the Jura (Laubscher, 1977; Philippe et al., 1996), the Mediterranean ridge offshore Libya (Von Huene, 1997; Mascle et al., 1999), the Parry Islands fold-and-thrust belt in the Canadian Arctic (Harrison and Bally, 1988; Harrison, 1995), the Romanian Carpathians (Stephanescu et al., 2000), the Salt Range in Pakistan (Butler et al., 1987; Davis and Lillie, 1994), and the Sierra Madre Oriental in northeast Mexico (Camerlo, 1998; Fischer and Jackson, 1999; Marrett, 1999) (cited in Costa and Vendeville, 2002). These well-studied examples, and the use of analogue modeling (Koyi, 1988; Cobbold et al., 1989; Dixon and Liu 1992; Huiqi et al. 1992; Letouezey et al., 1995; Koyi, 1998; Cotton and Koyi, 2000; Costa and Vendeville, 2002) have given us insight into the effects of salt detachments in the dynamical evolution of FTB. Generally, when FTB form in salt provinces, the structures that form are distinctly different from those in typical thin-skinned settings with siliciclastic detachments (Figure 1). The primary difference is the geometry of the entire FTB, since in the case of salt-detached FTB the deformation is mainly by folding with few symmetric high-angle reverse faults. Besides, FTB on salt have low critical tapers (≈1° or less) (Figure 2), and they do not present a preferred vergence (Jaume and Lillie, 1988; Costa and Vendeville, 2002). These remarkable differences are all explained by the fact that salt rocks have mechanical properties different from other lithologies (Buttler et al 1987; Jackson and Vendeville 1994; Hudec and Jackson, 2012). Besides the impact of salt in the rates and styles of deformation of FTB, its presence has also remarkable implications in the high potential that FTB have to develop trap structures and host large oil and gas fields (Fossen, 2010), in addition to severally influence the thermal maturation and migration pathways of hydrocarbons (Costa and Vendeville, 2002). All these facts represent a motivation to

study the geometry and kinematics of their associated structures, in order to obtain a better understanding of their hydrocarbon accumulations.

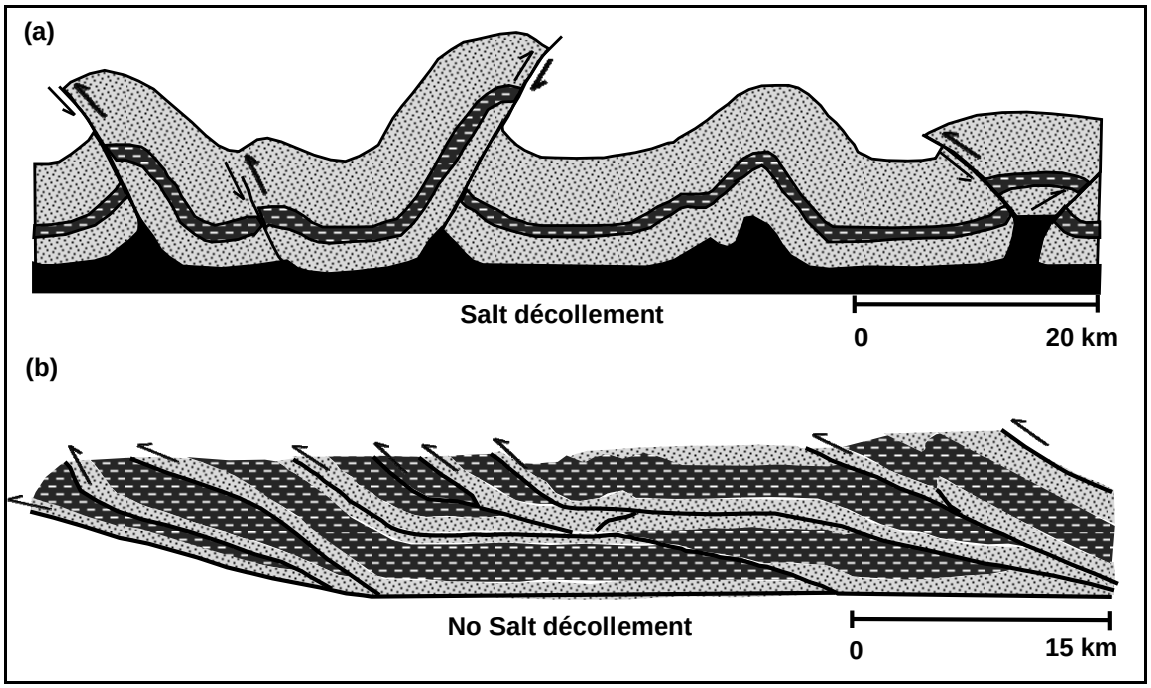

Figure 1. *Cartoons showing differences in structural style between FTB underlain (a) and not underlain (b) by a salt detachment level. Picture modified from Jackson and Talbot, 1991.*

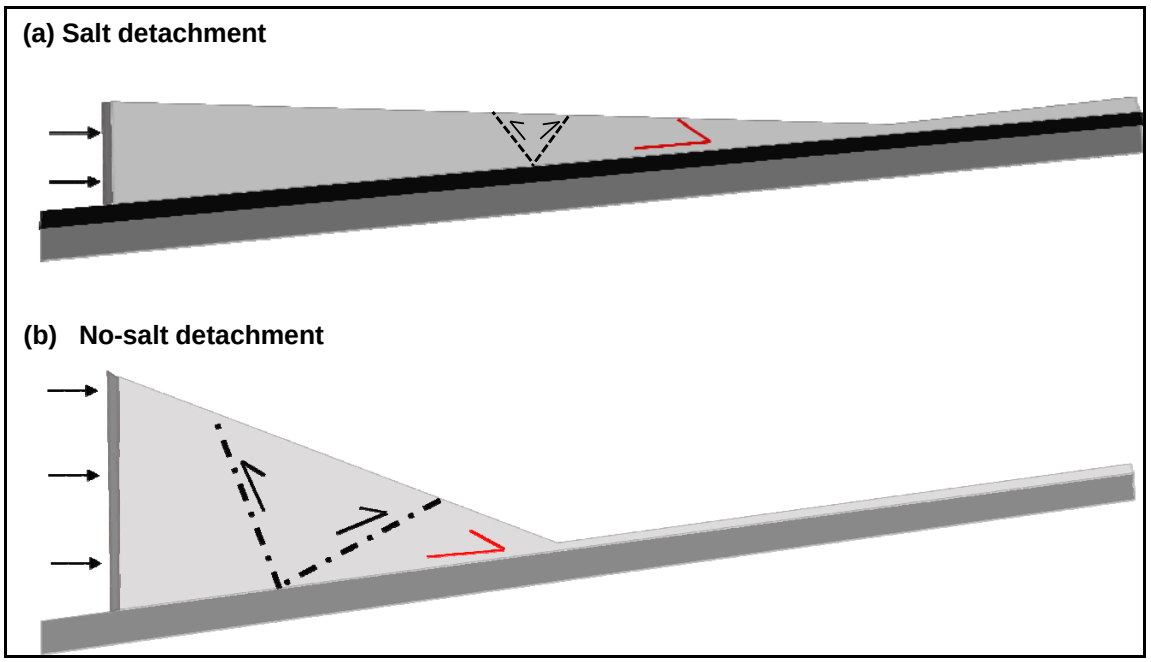

Figure 2. *Critical wedge taper theory, in which a weak detachment (a) results in a low taper angle, while stronger detachment (b) results in a high taper angle. Picture modified from Jaumé and Lillie, 1988*

However, despite of the identification of these structural features, their understanding is still limited largely due to FTB detaching on salt are part of orogenic belts that represent large-scale structures, which generally have a disharmonic style of deformation, and do not consent the extrapolation of their characteristics to a simple particular case of study. Moreover, much of the information known about FTB comes from field geology, normally only an upper part of the structure is exposed at the surface. High topographic variations, and the FTB irregular folded and faulted spatial distribution, do not allow to have a complete section. Therefore, the comprehension of such type of large-scale structures (m to km displacement) requires a seismic dataset. The objective of seismic acquisition and processing is to reveal the subsurface geological structures. However, in difficult geological scenarios as FTB, seismic imaging often is a challenge, and seismic images are of low-quality, not allowing reliable interpretations (Goffey et al., 2010). This reduction in seismic quality is caused by the presence of complex structures in the FTB detaching on salt, such as steeply dipping beds, overturned beds, complex thrust fault geometries, symmetrical/asymmetrical tight folds, and detachment levels (Figure 3). Structures with large dip angles produce several technical issues in seismic acquisition and processing. Furthermore, the presence of salt adds challenges for seismic imaging because of strong acoustic impedance at the salt boundaries (Hudec and Jackson, 2012). Therefore, seismic imaging of FTB detaching on salt is expected to be challenging, depending on vertical and lateral resolution, and how much can be actually illuminated. In consequence, a moderate analysis of regional and trap-scale structural geometries remains highly problematic, and dependent more on the knowledge of structural styles (Mitra and Fisher, 1992), and not on what can be extracted from the seismic data itself. Hence, the poor seismic characterization of these structures results in high uncertainty, and gives room for different interpretations. Bearing these facts in mind, the investigation of seismic imaging of FTB detaching on a salt layer might help to resolve these issues to improve the quality of seismic images and thereby their interpretation.

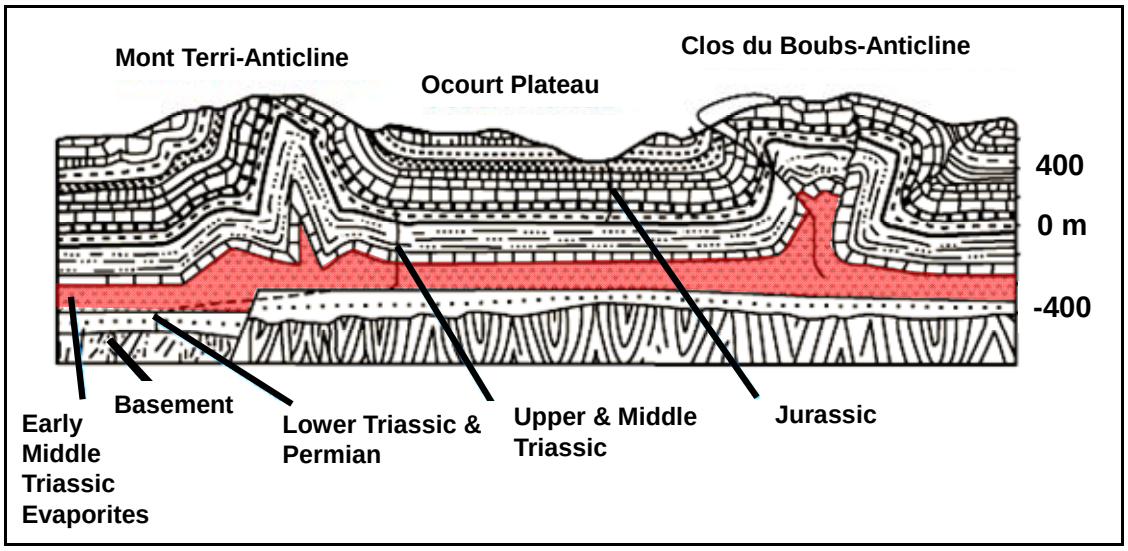

Figure 3. *Classic section through the Jura Mountains of eastern France showing steep, boxlike folds developed above a ductile salt layer. Picture modified from Laubscher, 1961.*

The main objective of this thesis is to forward model seismic images of compressional folds influenced by a salt layer, and syn-sedimentation to assess the impact of these variables in the structure and properties on the resulting seismic images. A second objective is to study the acquisition and processing challenges (illumination direction and wave frequency) involved in imaging these structures. Therefore, the idea is to use an approach that integrate the difficulties explained above to find a better way for imaging compressional folds. For this, it is necessary to understand the complexity, and properties of the structure, determinant to select the best strategy (acquisition and processing parameters) for better seismic imaging and interpretation. The use of geomechanical models consistent with the real geological data, and subsequent seismic modeling results are indispensable to identify and evaluate the imaging problems. To achieve these goals, the methodology used consists of four steps: 1) geomechanical modeling of the FTB using a 2D discrete element method (DEM) (Hardy et al., 2009); 2) finite strain computation using SSPX software (Cardozo and Allmendinger, 2009); 3) change of initial elastic properties based on finite volumetric strain computed from the DEM model (Botter et al., 2014); and 4) seismic imaging simulation, using a pre-stack depth migration (PSDM) simulator (Lecomte, 2008). This workflow is applied to a km-scale, 2D sequence of brittle, frictional siliciclastic sediments and ductile, viscous sequence of salt below. Also, to investigate the influence of the salt layer, and syn-sedimentation in the

evolution of the resulting geometry, and seismic imaging of the compressional folds, three different assemblages are run: Model 1 with no salt, Model 2 with salt, and Model 3 including salt, and syn-sedimentation. This study will constitute an attempt to first understand the geometry and kinematics of compressional folds, and, second to derive the best combination of different parameters such as illumination direction and wave frequency to reproduce the best properties of the structure, and especially to have a better seismic characterization of compressional folds. Ultimately, seismic modeling of geomechanical models will help geologists to resolve interpretation issues, besides to validate, and better assess their seismic interpretation, especially for complex structures such as salt-influenced compressional folds on real seismic data.

2. Methodology

This project uses the methodology of Botter et al. (2014) to forward model seismic images of compressional folds influenced by a salt layer, and a syn-sedimentation package, in order to study the evolution of structures, and evaluate acquisition and processing parameters for better seismic imaging and interpretation. This technique considers the complexity of the structure, the large finite strain resulting from its evolution, and the impact of overburden. The methodology consists of four steps (Figure 4): 1) geomechanical modeling of the compressional fold using a 2D discrete element method (DEM) (Hardy et al., 2009); 2) finite strain computation using SSPX software (Cardozo and Allmendinger, 2009); 3) modification of seismic properties based on finite strain (Botter et al., 2014); and 4) seismic imaging simulation, using a pre-stack depth migration (PSDM) simulator (Lecomte, 2008), taking into account the effects of frequency and illumination direction. This workflow is applied to a km-scale 2D DEM model sequence of brittle, frictional siliciclastic sediments and a ductile, viscous sequence of salt below. To investigate the influence of the salt layer, and syn-sedimentation in the evolution of the resulting structures, and seismic imaging of compressional folds, three different assemblages are run: Model 1 with no salt, Model 2 with salt, and Model 3 with salt, and syn-sedimentation.

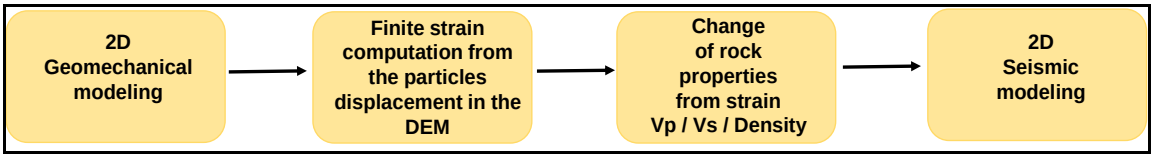

Figure 4. *Methodology used to model seismic images of salt-influenced compressional folds (from Botter et al., 2014).*

2.1 Mechanical modeling

Discrete element method – DEM

The discrete element method –DEM is a discontinuum method (Cundall and Strack, 1979) used commonly to study the evolution of an assemblage of discrete elements or particles under applied forces and displacement boundary conditions (Gray et al., 2014). These discrete elements interact with each other by simple contact laws, and their motion is updated using Newton´s equations (Hardy et al., 2009). The DEM allows observing the dynamical evolution of the particles system, and explore

problems where the growth of discontinuities (e.g. shear zones, faults, joints, or fractures) are significant (Gray et al., 2014). Furthermore, this technique allows to track the location/displacement of the particles through time. Hence, the displacement path, and kinematic evolution of the system can be recognized at any phase of the model (Vidal-Royo et al., 2011). For these reasons, this method has been used in many geological problems, especially involving the analysis of high-strain brittle deformation in the sedimentary cover such as normal faulting in layered sequences (Schöpfer et al., 2006, 2007a, 2007b; Egholm et al., 2008; Botter et al., 2014), fault bend folding (Strayer et al., 2004; Benesh et al., 2007), fault-propagation folding (Finch et al., 2003, 2004; Cardozo et al., 2005; Hardy and Finch 2006, 2007), fold and thrust belts (Burbridge and Braun 2002; Strayer and Suppe 2002), detachment folding (Hardy and Finch, 2005), and doubly vergent thrust wedges (Hardy et al., 2009), to name some examples. In all these cases, the results have a strong correspondence to the deformation seen in the field and seismic. Thus, the DEM is regarded to be a suitable method to study the geometry and kinematics of compressional folds, from initiation, propagation and development including the change from faulting to folding in a realistic way.

Discrete element model – cdem2D

The 2D DEM code (cdem2D) to use in this project was developed and provided by Stuart Hardy (ICREA, University of Barcelona), and it is based on the *lattice solid model* of Mora and Place (1993), later extended by Hardy and Finch (2005, 2006), and Hardy et al. (2009). cdem2D models the dynamic evolution of a rock volume treated as an assemblage of a large number of separate, rigid-circular particles in 2D (Figure 5a-b), whose interaction is explicitly considered. Particles are influenced by gravitational, elastic, frictional, and viscous (in the case of salt) forces and obey Newton's equation of motion (Hardy et al., 2009). The particles can have different physical (size and density), and mechanical properties (elastic and frictional). In kilometer scale simulations like the ones in this thesis, particles are meter size and do not represent the sedimentary rock grains. However, the DEM is able to produce a reasonable FTB geometry that can be used as an input for the following steps of seismic imaging. The model consists of a ductile-brittle sequence (Figure 5a-b). The vertical layering represents the ductile salt and the horizontal layers represent the brittle siliciclastic sequence. The brittle cover (siliciclastic) has only a frictional

behavior (zero strength at zero confining pressure and no tensile strength) (Hardy, 2013), and in the ductile salt layer the viscous force is proportional to the derivative of the velocity field. Furthermore, cdem2D allows temporal changes to the initial configuration such as syn-sedimentation. The impact of these variables are analyzed on the resulting evolution of the compressional folds. Finally, imposed horizontal displacement is applied to the boundary particles in the left wall in order to initiate, and develop the compressional fold in the model. The left side boundary particles are displaced 5 meters to the right every increment.

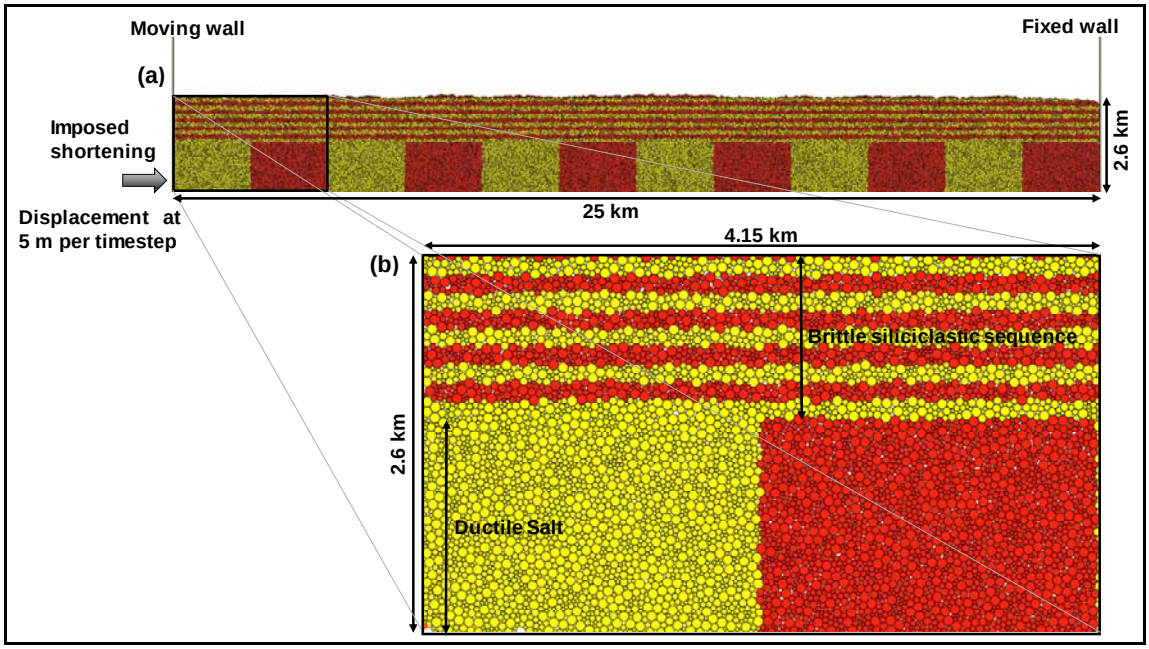

Figure 5. *(a) Illustration of the initial configuration and boundary conditions of the DEM used in this project (for Model 2, and 3). Note the ductile (vertical layering) and brittle (horizontal layering) sequences. (b) Packing of particles before deformation with different radii. Rightwards displacement on the left wall increases at 5m/increment.*

2.2 Finite strain computation

The use of the DEM enables to extract additional information such as strain in space and time. Incremental or total displacement of the particles, which are known from the DEM model at each time step, is used to compute strain in SSPX software (Cardozo and Allmendinger, 2009) using a nearest-neighbor routine that divides the assemblage into a grid of regular cells. The strain is computed from the displacement of n-particles within a radius from the cell center. This computation assumes that

strain is homogeneous within each cell, therefore the heterogeneous strain in the compressional fold is adapted to a cell-based homogeneous strain. Therefore, it is important to use an appropriate cell size to capture the complexity of the compressional fold related strain. The application of SSPX to the 2D DEM model described above can be observed in Figure 6. This figure shows the total strain distribution of the DEM after 1.25 (Figure 6a) and 5 km (Figure 6b) shortening. Maximum shear strain displays the 2D variation of the resultant strain in the assemblage showing a complex area of deformation, especially at the latest stage of the model (Figure 6b). The shear strain zones are stronger and wider at the thrusts and associated folds, suggesting that the shortening was mainly accommodated in these areas. Figure 6 is an intermediate step to transfer the data from the geomechanical model to the seismic model.

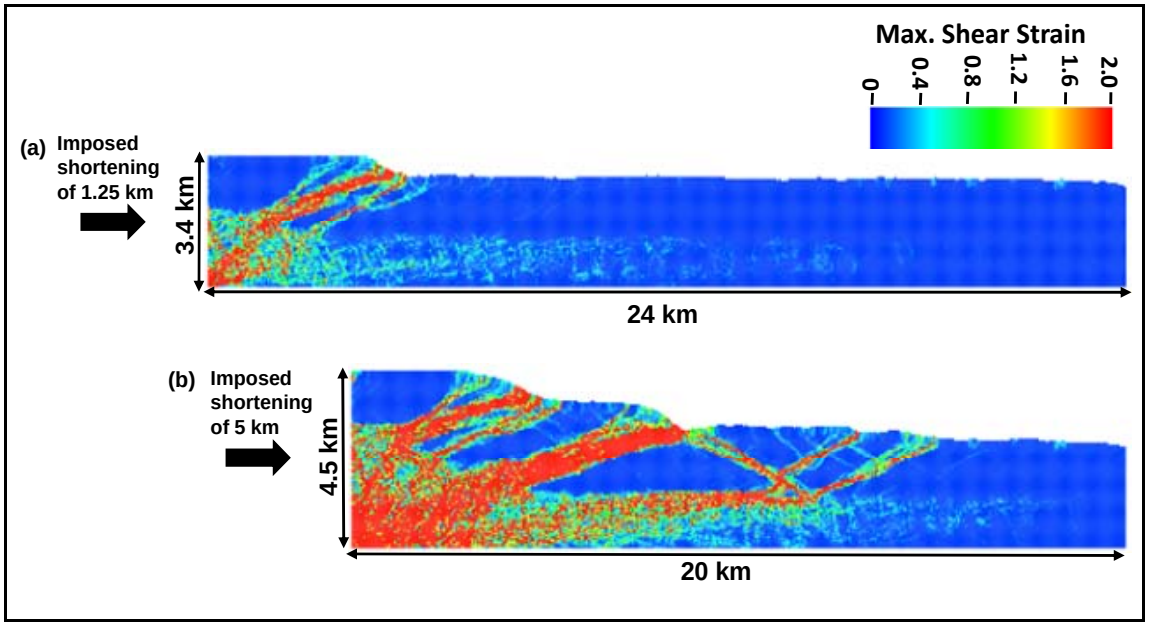

Figure 6. *Finite strain computation of DEM Model 2 after (a) 1.25 and (b) 5 km shortening. Strain was computed in 25x25m cells using a nearest neighbor algorithm with 6 particles neighbors and maximum radius 130 m. (Cardozo and Allmendinger, 2009).*

2.3 Modification of seismic properties based on finite strain

Seismic imaging requires an input reflectivity grid computed from elastic properties. The 2D distribution of strain such as shear and volumetric strain can be used to condition the change of rock properties, including density and seismic velocities in

the seismic model (Botter et al., 2014). Nonetheless, under large and permanent deformations, it is not possible to use standard, continuum rock physics equations to predict the change of elastic properties due to large finite strains (Botter et al., 2014). Therefore, based on the few available studies about the impact of compaction on seismic properties (e.g., Holt et al., 2008, Sigernes, 2004 Skurtveit et al., 2013), we can use very simple empirical relationships between finite strain (e.g. volumetric strain) and changes in the rocks physical properties, similar to those of Botter et al. (2014). Thus, to start porosity (ϕ), density (ρ), P-wave (*Vp*), and S-wave (*Vs*) velocities are assigned to the rock material corresponding to sandstone and shale (pre-growth, and growth sequences) in the DEM before deformation (Table 1). Even though, for geomechanical modeling the sedimentary cover is considered as a homogeneous brittle sequence, for seismic imaging it is divided into sandstone and shale to obtain different reflectivities and make the image more remarkable. Secondly, density and seismic velocities of the pre-growth sandstone and shale are modified only by volumetric strain (ϵ*v*), and finally simple empirical relations (Equations 1-4) of Botter et al. (2014) according to the curves presented in Figure 7 are applied to the geomechanical model in order to modify its initial elastic properties by volumetric strain (ϵ*v*) computed from the DEM.

Porosity (ϕ) is modified from its initial value (ϕ_{ini}), and volumetric strain (ϵ*v*), according to a linear relation (Figure 7 and Equation 1), then density (ρ) is computed from porosity (ϕ), considering saturated conditions (Equation 2):

$$\phi = \phi_{ini}\,(0.25\,\epsilon v + 1), \quad -1 \leq \epsilon v \leq 1 \qquad \textbf{(1)}$$

$$\rho = \rho g\,(1 - \phi) + \rho w\,\phi \qquad \textbf{(2)}$$

ρg, ρw Represent grain and fluid density respectively.

P-wave velocity *Vp* follows a sigmoidal relation (Equation 3, and Figure 7), and highlights that the assumed change of P-wave velocity with volumetric strain is more relevant at lower than at large strains:

$$Vp = \begin{cases} Vpini\,(-0.25\,\epsilon v\,\hat{}\,2 - 0.5\,\epsilon v + 1) & -1 \leq \epsilon v \leq 0 \text{ (compactation)} \\ Vpini\,(0.25\,\epsilon v\,\hat{}\,2 - 0.5\,\epsilon v + 1) & 0 \leq \epsilon v \leq 1 \text{ (dilation)} \end{cases} \qquad \textbf{(3)}$$

Finally, S-wave velocity is related to P-wave using Han's relation:

$$Vs = 0.794Vp - 0.787 \quad \textbf{(4)}$$

These empirical relations are probably not accurate, but are enough to get a realistic reflectivity grid to use as an input in the seismic modeling. These changes are only applied to the siliciclastic layers (pre-growth sequence). Initial values for the growth strata are kept constant, since these strata are unconsolidated and behaves differently than the pre-growth strata. The properties of the salt are also not modified as few physical changes are expected in the salt due to its very ductile behavior. The main purpose of this workflow is to simulate seismic imaging of the salt boundary (not the internal structure of the salt), and the compressional folds in the siliciclastic layers.

	Porosity (ϕ)	Density (g/cm^3)	P-wave (Vp) (km/s)		S-wave (Vs) (km/s)	
Halite		**2.1**	**5.5**		**3.1**	
Sandstone	**0.15**	**2.4**	**4**		**2.39**	
Shale	**0.3**	**2.7**	**2**		**0.80**	
Syn-sedimentary			**Ss**	**Sh**	**Ss**	**Sh**
			3	**1.5**	**1.79**	**0.6**

Table 1. *Elastic properties assumed for the undeformed siliciclastic sequence, the salt, and the syn-sedimentary sequence. Values for the salt and the growth strata are kept constant (Mavko et al., 2009).*

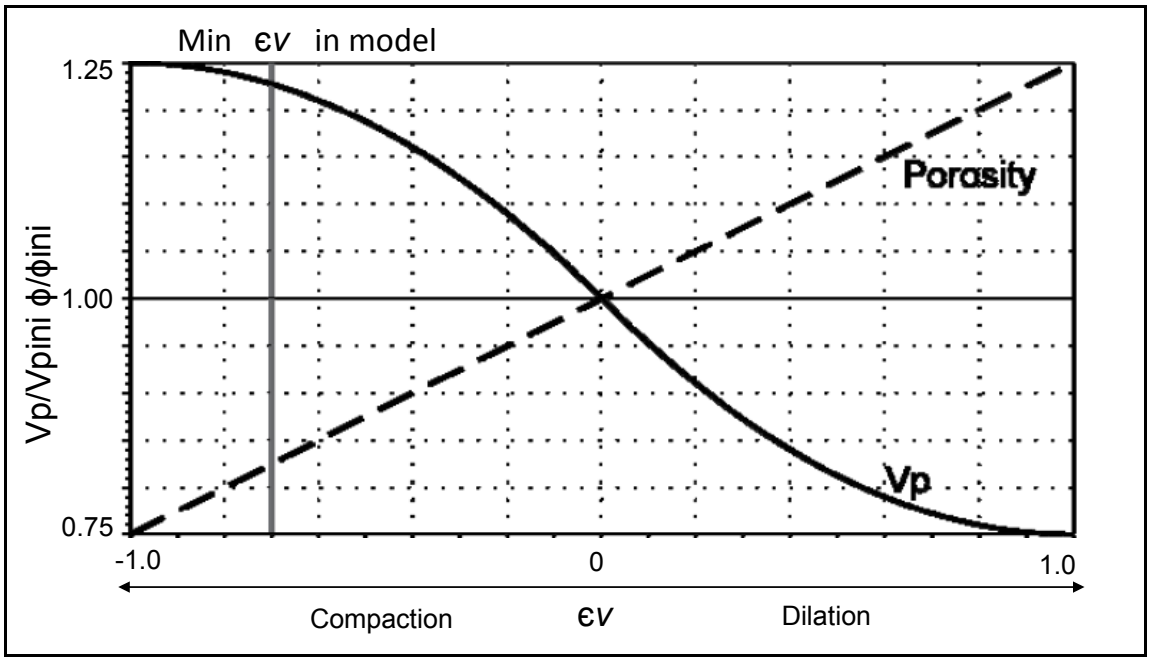

Figure 7. *Assumed change of porosity (ϕ) and P-wave velocity (*Vp*) with volumetric strain (*εv*). ϕ_{ini} and* Vp_{ini} *are porosity and P-wave velocity before deformation. Picture modified from Botter et al. (2014).*

2.4 Seismic imaging simulation, using a pre-stack depth migration (PSDM) simulator

The last step is modelling the seismic images to assess the impact of the salt, and syn-sedimentation in the structure and properties of the modeled compressional folds on the resulting seismic images. The technique to be used is a 3D (PSDM) pre-stack depth migration simulator (Lecomte, 2008) that acts as an image processing approach by distorting the input reflectivity grid to recreate the effects of seismic imaging (Figure 8). The PSDM simulator works in the pre-stack domain and in depth, and appropriately manipulates 3D effects in resolution (lateral reflector continuity) and illumination (survey geometry) (Botter et al., 2014), including lateral resolution effects such as those resulting from faults or other discontinuities (Lecomte, 2008). This technique takes as an input an angle dependent reflectivity grid (Figure 8a) computed from elastic properties (Vp, Vs, and density), obtained from the previous step (Botter et al., 2014). From a ray-based method (Gjøystdal et al., 2007) illumination vectors (Lecomte, 2008), are calculated (Figure 8b) at the center of a selected target in the model (e.g., center of the model), and they are function of velocity model, seismic survey, wave type, overburden, frequency, and other PSDM

associated factors; in other words, they are dependent on acquisition parameters. The calculation of these illumination vectors is important, since their direction displays the dipping reflectors that will be seen by the seismic waves (Botter et al., 2014). The illumination vectors combined with a specific wavelength are then used to calculate particular PSDM filters in the wavenumber domain (using a Fast Fourier Transform – FFT; Figure 8c). Figure 8c shows three different PSDM filters, (C1) equivalent to a full covering survey acquisition illuminating an extensive range of dips, (C2) and (C3) use a sub-selection of the survey to create an off-side illumination towards the right or left side (the vertical band in the PSDM filter is not considered, therefore illumination from the flat reflectors is avoided), respectively. Finally, PSDM filters are applied to the reflectivity grid in the wavenumber domain to simulate the final seismic image back in the space domain (through a reverse Fast Fourier Transform – FFT^{-1}; Figure 8d). Furthermore, an inverse FFT^{-1} of the wavenumber PSDM filters produces a so-called Point-Spread Function (PSF) in the spatial domain (Figure 8e), that is the PSDM responses of point scatterers in the considered model at the reference point (Lecomte, 2008), and for the chosen survey, model, wave type and frequency. The response of the PSF of the structure is an indication of the imaging capability of the PSDM, allowing to have a quantifiable evaluation of the vertical and lateral resolution of the point scatterers that finally indicate the resolution of the simulated PSDM seismic images for the specific target considered.

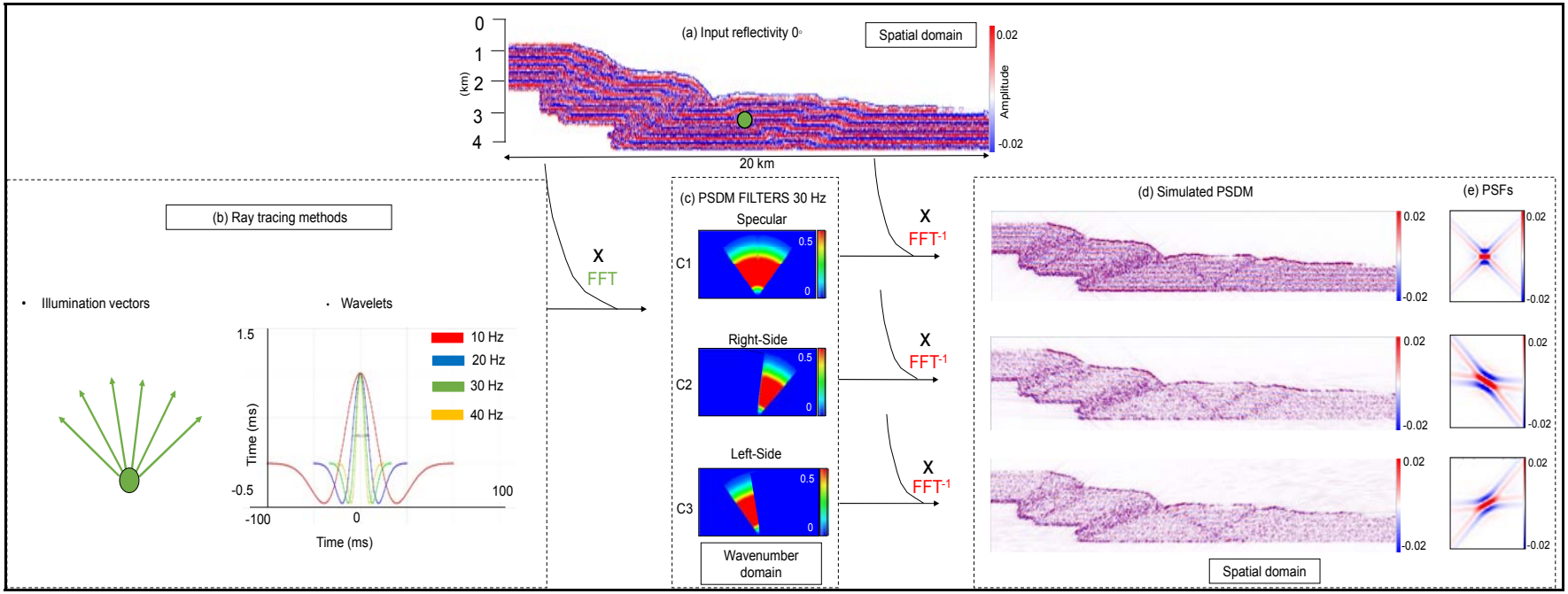

Figure 8. *Illustration of the PSDM simulator. (a) Reflectivity grid used as an input in the spatial domain. (b) Ray-based methods calculate illumination vectors at the target point (green dot) for the considered survey, and combined with a selected wavelet (30 Hz) to generate (c) the equivalent PSDM filters in the wavenumber domain for specular (C1), right (C2), and left (C3) side illuminations, using a FFT on the reflectivity grid. (d) Application of the PSDM filters to the input reflectivity in the wavenumber domain, plus an inverse FFT (FFT^{-1}) produces the simulated PSDM images in the spatial domain, and (e) the resulting PSFs (point spread functions).*

3. Results

3.1 Geomechanical modeling

The initial dimensions of the DEM model are 25 X 2.6 km, in a homogeneous sequence of brittle, frictional siliciclastic sediments above, and ductile, viscous salt below (Figure 5). The final model is achieved by imposing 5 km horizontal displacement from the left wall in 1000 increments, so every increment corresponds to 5 m shortening. The assemblage contains 43,883 particles, with radii between 12.5 and 31.5 m, and density 2500 kg/m^3. The model consists of 24 layers; the upper 12 layers are the siliciclastic cover, and the lower 12 layers are salt (Figure 5). Three models were considered: Model 1 has no salt (Figure 9; initial configuration), model 2 has salt at the base (Figure 5), and model 3 has salt and syn-sedimentation (same initial configuration as model 2, Figure 5). Shear and volumetric strain were computed at different stages, using the methods described in section 2.

3.1.1 Model 1 (DEM - no salt)

This simulation has only a homogeneous brittle sedimentary sequence (Figure 9; initial configuration). Therefore, the mechanical behavior of the assemblage is purely frictional. All other parameters are identical to those previously described.

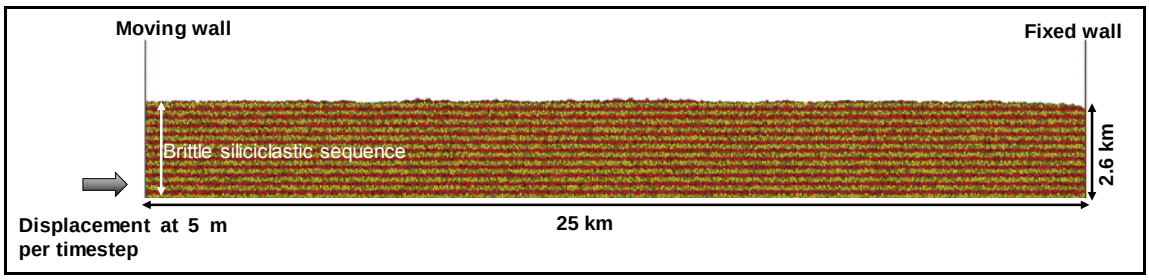

Figure 9. *Illustration of the initial configuration and boundary conditions of DEM Model 1, where the assemblage represents a homogeneous siliciclastic sequence. Displacement increases at 5 m/time step.*

3.1.1.1 Evolution of geometry and finite strain

Figure 10 shows the geometry, and Figure 11 the shear and volumetric strain of the model after 0.5, 1.25, 2.5, 3.75, and 5 km shortening. After 0.5 km shortening, the

first thrust (1) develops with a dip of ≈ 25°, forming an anticline above it (Figure 10b). At 1.25 km shortening, the thrust propagates upwards, breaching the anticline (Figure 10c). The shear and volumetric strain (Figure 11a-b) are concentrated along the thrust. At 2.5 km shortening, there is more displacement and folding on thrust 1 and a second forward thrust develops with a similar dip angle (Figure 10d). Shear and volumetric strains are high along these two thrusts and a band of lower (but not zero) shear strain close to the surface suggests the initiation of a third thrust (Figure 11c). At 3.75 km, thrust 3 with ≈ 20° dip and associated folding develops, together with more displacement and folding in thrusts 1 and 2 (Figure 10e). At this stage, shear and volumetric strain (Figure 11d) display wider strain areas for thrusts 1 and 2, which overall are under compaction (negative volumetric strain), and a narrower strain area for thrust 3, which at this stage displays dilation (positive volumetric strain). Finally, after 5 km shortening, the three thrusts exhibit significant displacement and folding (Figure 10f). From the last stage, it seems that much of the displacement and folding is on thrusts 2 and 3 (Figures 10f and 11e). Thrusts are therefore younger in the direction of transport. They become gentler as well, with thrusts 1 and 2 dipping 25°, and thrust 3 dipping 20°. Shear and volumetric strain (Figure 11) show that strain is concentrated around the thrusts. These thrust zones experience mostly compaction (Figure 11 right column). At the end of the simulation, the structure reaches a final height of ≈ 4.5 km and a width of ≈ 20 km (Figure 10f).

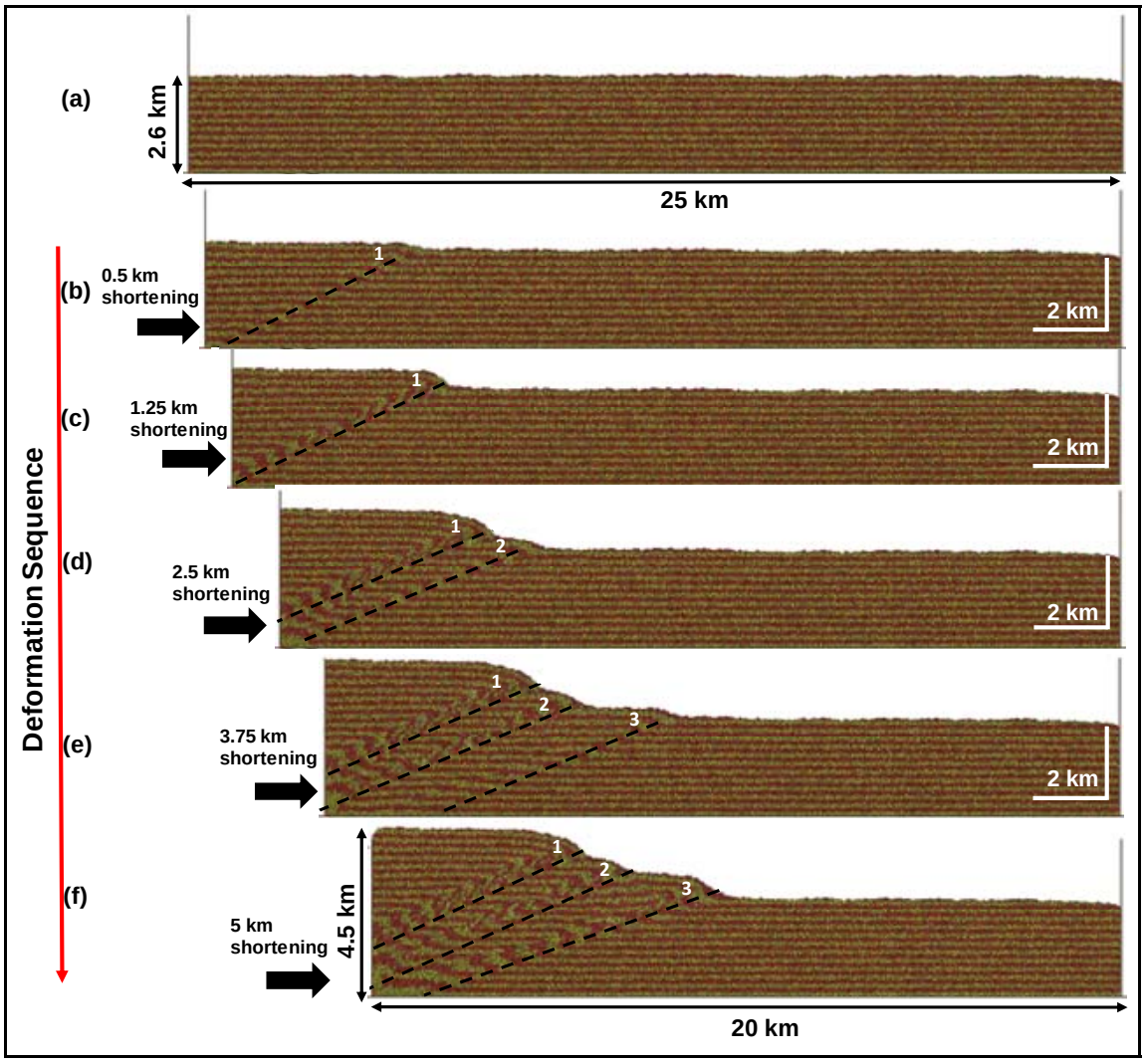

Figure 10. *(a) Initial geometry of Model 1, and new geometry after (b) 0.5, (c) 1.25, (d) 2.5, (e) 3.75, and (f) 5 km shortening.*

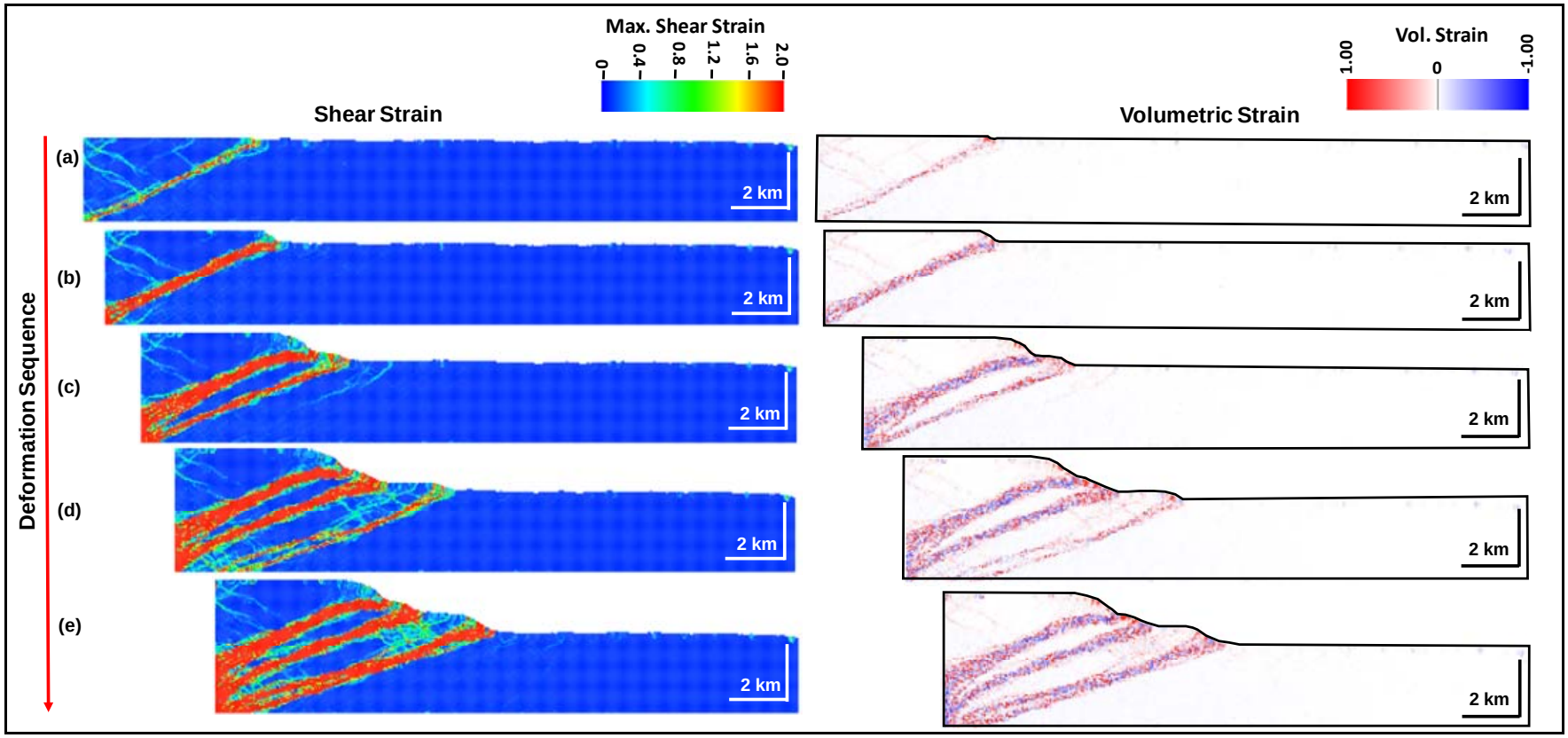

Figure 11. *Shear strain (left column), and volumetric strain (right column) of Model 1 at the stages of Figure 10. Strain was computed in 25x25m cells using a nearest neighbor algorithm with 6 particles neighbors and maximum radius 130 m (Cardozo and Allmendinger, 2009).*

3.1.2 Model 2 (with salt)

This simulation has a salt layer below a homogeneous sequence of brittle, frictional siliciclastic sediments (Figure 5; initial configuration). Hence, the mechanical behavior of the assemblage is purely frictional in the brittle sequence, and in the salt layer the viscous force is proportional to the derivative of the velocity field. All other parameters are identical to those previously described.

3.1.2.1 Evolution of geometry and finite strain

Figure 12 shows the geometry, and Figure 13 the shear and volumetric strain of the model after 0.5, 1.25, 2.5, 3.75, and 5 km shortening. After 0.5 km shortening the first thrust nucleates above the salt layer and develops through the brittle sequence with a dip of ≈ 25° forming an anticline above it (Figure 12b). At 1.25 km shortening, a back thrust (2) and a second forward thrust (3) develop with a dip of ≈ 30° (Figure 12c) along with more displacement and folding on thrust 1. The salt layer shows low deformation, but its flow associated to the overlying thrusts is clear. Shear and volumetric strains (Figure 13b) are higher, and wider along the first thrust, and narrower for thrusts 2 and 3. In the salt layer, the strains are higher along the thrusts. However, a band of lower shear strain spreads towards the right, suggesting lateral movement of the salt. At 2.5 km, there is more displacement and folding on thrust 3, and a fourth forward thrust with of ≈ 20°dip and associated anticline develops (Figure 12d). Increasing shortening led to a significantly thickening of the salt layer below the older thrusts. At 3.75 km, the fourth thrust propagates upwards, breaching the anticline formed before (Figure 12e). In addition, a fifth forward thrust and related fold develops with a dip of ≈ 25°. At this stage, shear and volumetric strain (Figure 13d) are higher and wider along the older thrusts (1, 2, 3 and 4) than in the new thrust 5. The highest shear strain zones correspond with the highest compaction, although, at certain places the thrusts are also under dilatation. Moreover, the shear strain shows the development of a band of low strain through the brittle cover, suggesting the initiation of a back-thrust and a pop-up structure. After 5 km shortening, the brittle cover is deformed by several thrusts and associated folding, over a long distance (Figure 12f). The pop-up structure develops along with more displacement and folding on thrust 4, and a seventh forward thrust with a dip of ≈ 30° and related fold

develop. The salt layer in contrast shows less localized deformation and flow associated to the overlying thrusts (Figure 12f). The shear strain zones are stronger and wider at the thrusts and associated folds at the left of the model, suggesting that the increased shortening was mainly accommodated in these areas, which overall are under contraction (Figure 13e). At the end of the simulation, the structure reaches a final height of ≈ 4.5 km and a width of ≈ 20 km (Figure 12f).

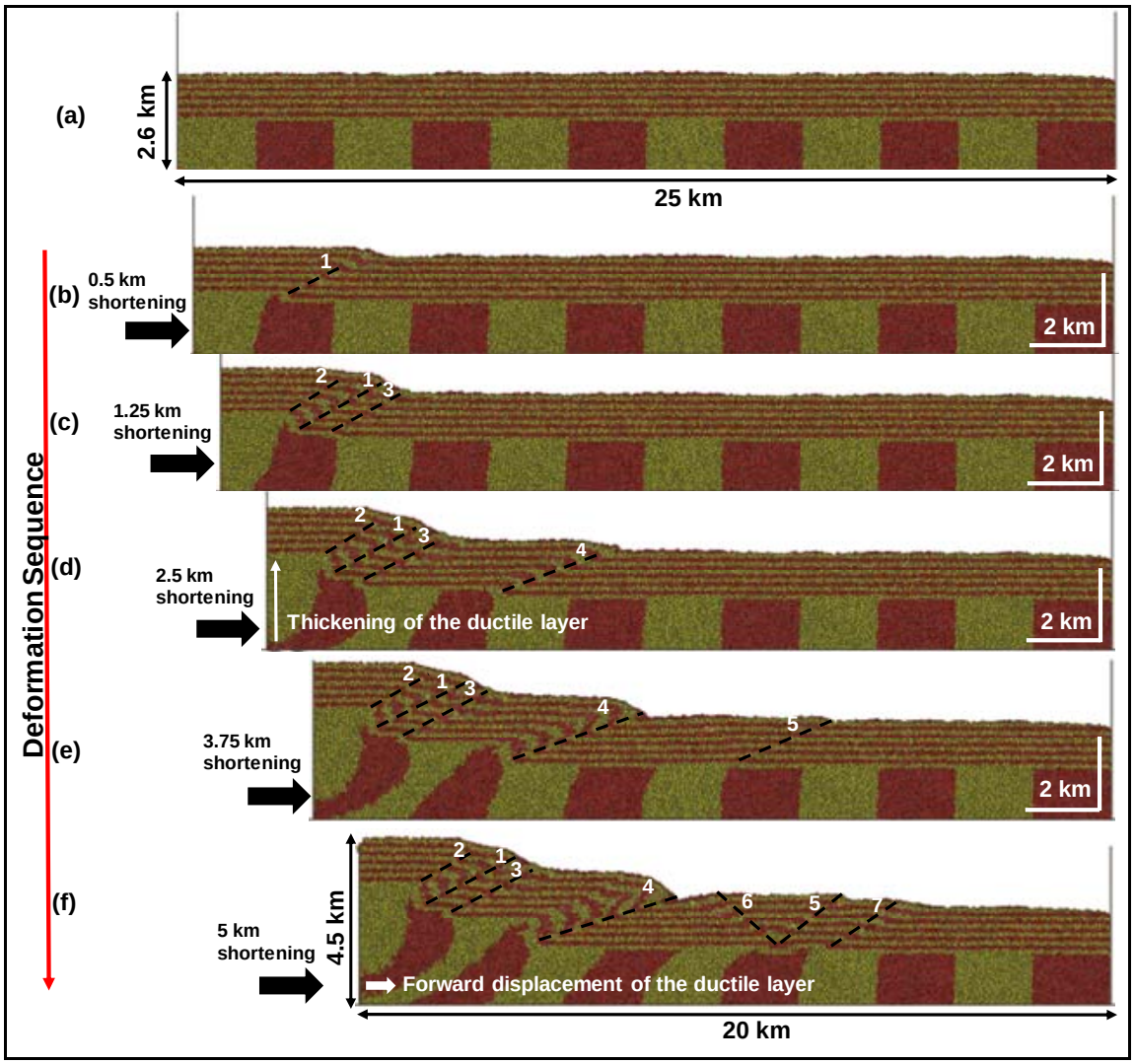

Figure 12. *(a) Initial geometry of Model 2, and new geometry after (b) 0.5, (c) 1.25, (d) 2.5, (e) 3.75, and (f) 5 km shortening.*

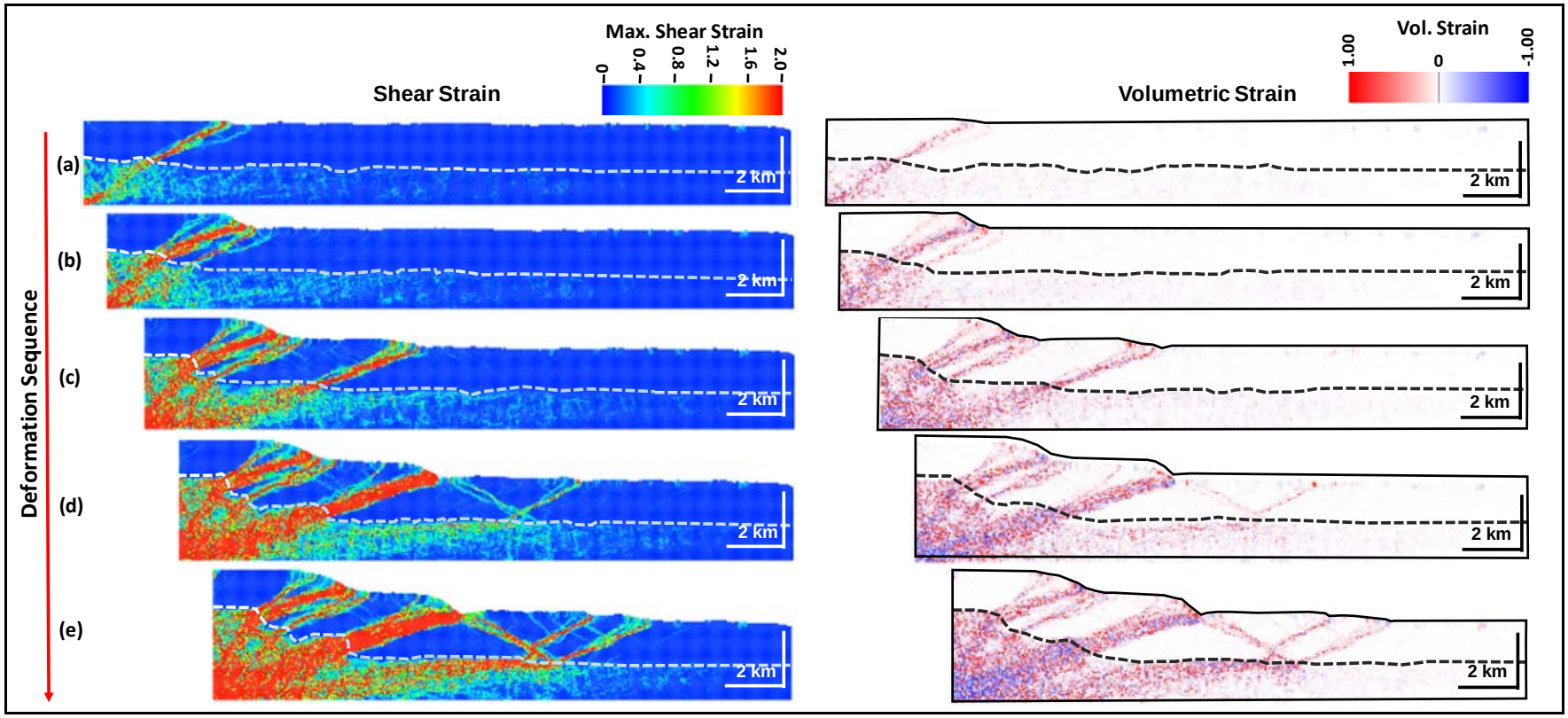

Figure 13. *Shear strain (left column), and volumetric strain (right column) of Model 2 at the stages of Figure 12. Strain was computed in 25x25m cells using a nearest neighbor algorithm with 6 particles neighbors and maximum radius 130 m (Cardozo and Allmendinger, 2009).*

3.1.3 Model 3 (with salt, and syn-sedimentation)

This simulation has the same initial configuration as Model 2 (Figure 5; initial configuration) and in addition considers a syn-sedimentation package. Syn-sedimentation covers completely the underlying structure. Hence, the sedimentation rate exceeds the uplift rate. The mechanical behavior of the assemblage is as Model 2. All other parameters are identical to those previously described.

3.1.3.1 Evolution of geometry and finite strain

Figure 14 shows the geometry, and Figure 15 the shear and volumetric strain of the model after 1, 2, and 3 km shortening. After 1 km shortening, the first forward thrust nucleates above the salt layer and develops with a dip of ≈ 30° (Figure 14b) along with a back-thrust (2), forming a pop-up structure in the pre-growth sequence. A second less steep back-thrust nucleates from the previous thrust. While deformation occurs, a syn-sedimentation package deposits. Shear and volumetric strains (Figure 15a) are high in the core of the fore-thrust and along it. Instead for the back-thrust, strain areas are narrower and lower. At 2 km shortening, there is more displacement and folding on thrust 1 and a new back-thrust (4) develops with a dip of ≈ 35° through the pre-growth sequence (Figure 14c). The salt layer shows less localized deformation that led to a considerable increase in its thickness and flow associated to the overlying structure. The geometry of the growth sequence shows folding in the sequences above the fore and back limbs, and thinning towards the fold crest. At this stage, shear and volumetric strains (Figure 15b) are higher along the first thrust, which also displays the widest strain area that is mainly under compaction. Along the back-thrusts in contrast, shear and volumetric strains show narrower strain areas, which at this stage display dilation. In the salt layer, shear and volumetric strains show the highest strain area related to the overlying fore-thrust and a band of lower strain that spreads towards the right, suggests its lateral propagation (Figure 15b). Finally, after 3 km shortening, the pre-growth sequence is deformed by a disharmonic fold that concentrates at the left side with a steeper forelimb and a complex structure in its core (Figure 14d). A last forward thrust (5) develops with a dip of ≈ 25° along with more displacement and folding on thrust 1. Growth strata are highly folded into a synclinal region above the steeper forelimb, and into an anticlinal

region above the back-limb. The salt layer in contrast shows less localized deformation and flow associated to the overlying fold. Shear and volumetric strain (Figure 15c) show that strain is significantly wider and stronger around the first thrust and the salt layer below, suggesting that most of the displacement and folding concentrates there. These zones experience mostly compaction, although a dilatation component is seen in the back-thrusts. At the end of the simulation, the structure reaches a final height of ≈ 4.2 km and a width of ≈ 22 km (Figure 14d).

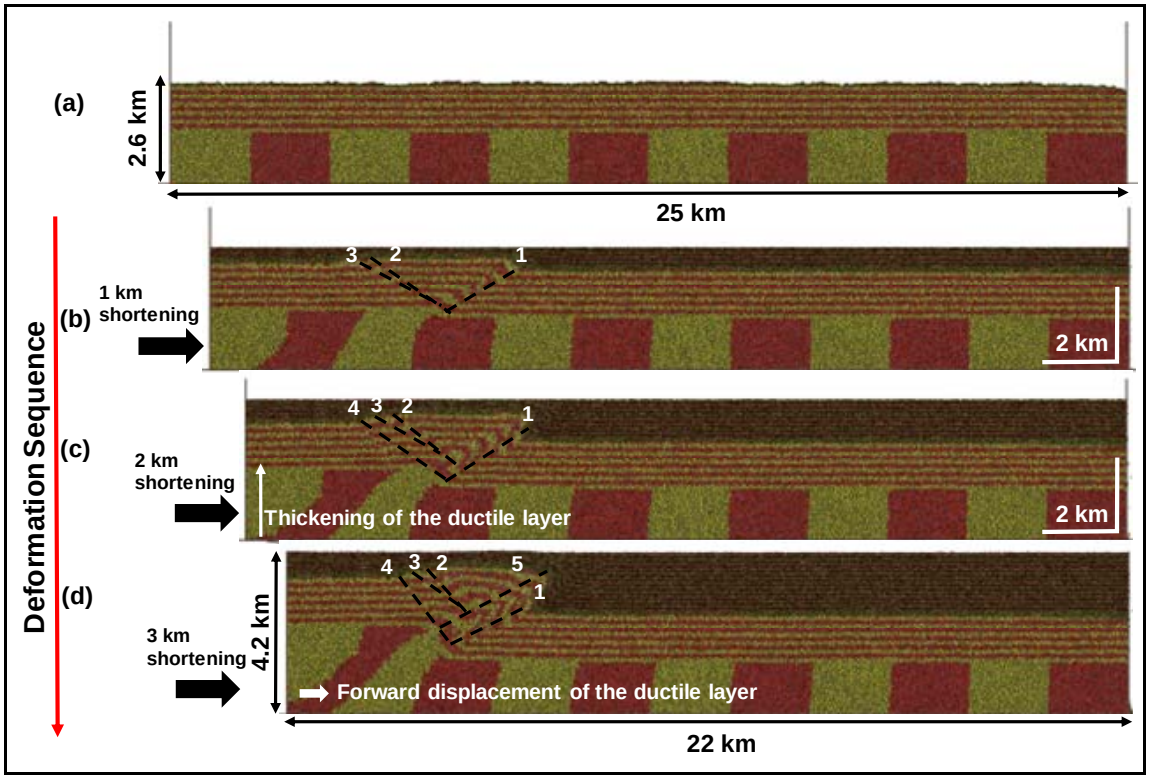

Figure 14. *(a) Initial geometry of Model 3, and new geometry after (b) 1, (c) 2, and (d) 3 km shortening.*

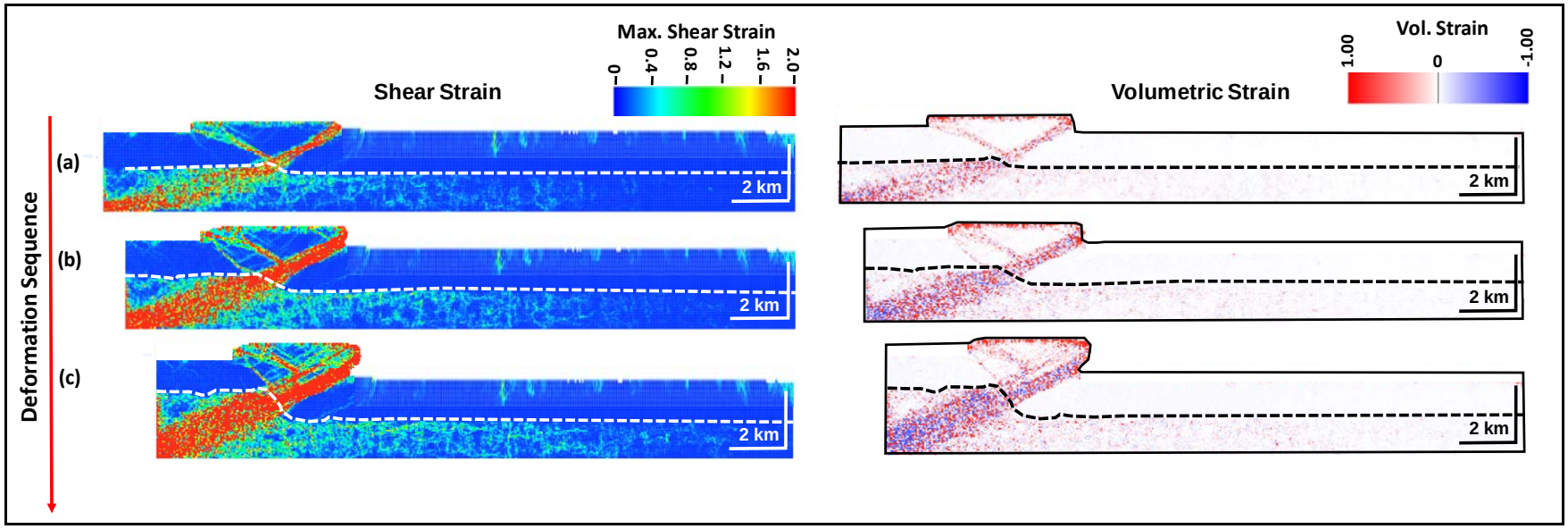

Figure 15. *Shear strain (left column), and volumetric strain (right column) of Model 3 at the stages of Figure 14. Strain was computed in 25x25m cells using a nearest neighbor algorithm with 6 particles neighbors and maximum radius 130 m (Cardozo and Allmendinger, 2009). Strain in growth strata is not shown.*

3.1.4 Discussion of geomechanical models

The modeling results (Figure 16) show the influence of the salt layer and syn-sedimentation on the evolution and resulting geometry of compressional folds. The most remarkable observation from the models is the contrast in deformation style that is conditioned by the sedimentary sequences involved (brittle, brittle-ductile and brittle-ductile-syn-sedimentation). As predicted by Davis et al., 1983, above a ductile layer the thrusts can propagate faster and further (Figure 16b) than on a brittle sequence (Figure 16a). Also, the easier propagation of the thrusts and associated folding in Model 2 (Figure 16b) results in a wide FTB with a low taper angle compared to Model 1, where the thrusts are rather locally concentrated (Figure 16a). In Model 1 the formation of the thrusts presents a preferred forward vergence. However, in Model 2 above a ductile layer, forward and backward vergent thrusts are developed. On the other hand, shortening in Model 3 including syn-sedimentation (Figure 16c), results in the development of a tight fold with a steeper forelimb and with disharmonic folding in its core within the pre-growth sequence. In addition, the growth of the fold is confined and does not propagate laterally. Therefore, the extra-load of the syn-sedimentation sequence restricts the propagation of the deformation and produces a tighter fold, compared to a set of open folds as occurs in Model 2 (Figure 16b). Furthermore, the resulting geometry of growth strata is controlled particularly by the folding development within the pre-growth sequence and the rates of uplift and sedimentation. Hence, growth strata are folded above the forelimb into a synclinal region, thins towards the fold crest, and is folded into an anticlinal region above the back-limb.

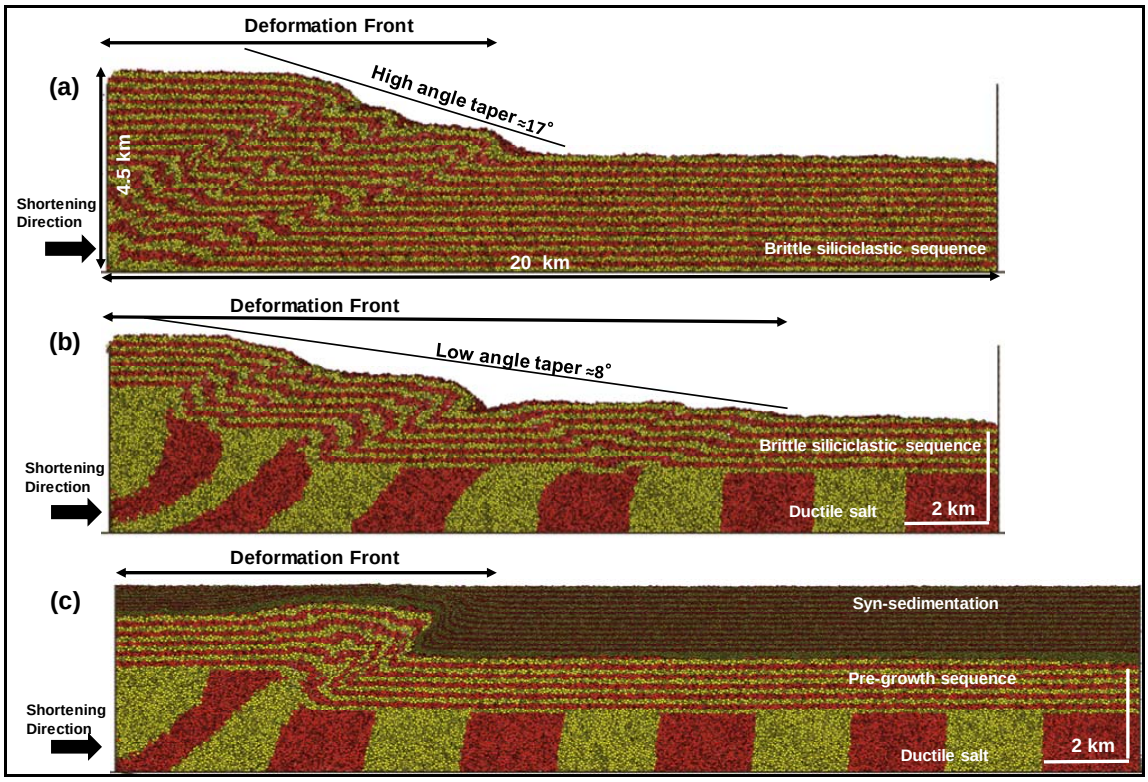

Figure 16. *Final geometries of (a) Model 1 (b) Model 2 after 5 km, and (c) Model 3 after 3 km shortening.*

3.2 Change of seismic properties

Seismic imaging requires an input reflectivity model of the compressional folds at some amount of shortening. Models at different displacement are chosen to seismic image to have an understanding of the impact of deformation on the resolution of the resulting seismic images. For Models 1 and 2, the DEM models after 1.25, 2.5, 3.75 and 5 km, and for Model 3 the DEM models after 1, 2 and 3 km shortening were selected. To compute the seismic properties in the pre-growth/growth sequences in the DEM models, initial elastic properties are assigned to the undeformed rock material corresponding to sandstone and shale (Table 1). Then, elastic properties of the pre-growth sandstone and shale are modified using simple empirical relations (Equations 1-4). Initial property values for the growth strata are kept constant, since these strata are unconsolidated and behave differently than the pre-growth strata. The initial properties of the salt are not modified as few physical changes are expected due to its ductile behavior. The changes of density and seismic velocities after 1.25, 2.5, 3.75 and 5 km shortening are shown in Figure 17 and 18 for Models 1

and 2, respectively and for Model 3 after 1, 2 and 3 km shortening in Figure 19. As predicted from the geomechanical model results, the zones most affected by volumetric strain in every model correspond to the different thrust zones and associated folding. Therefore, these zones experience more changes in wave velocities and density, resulting in more impact on the seismic images. These changes in elastic properties are more remarkable after 5 km for Models 1 and 2 (Figure 17-18d), and after 3 km shortening for Model 3 (Figure 19c).

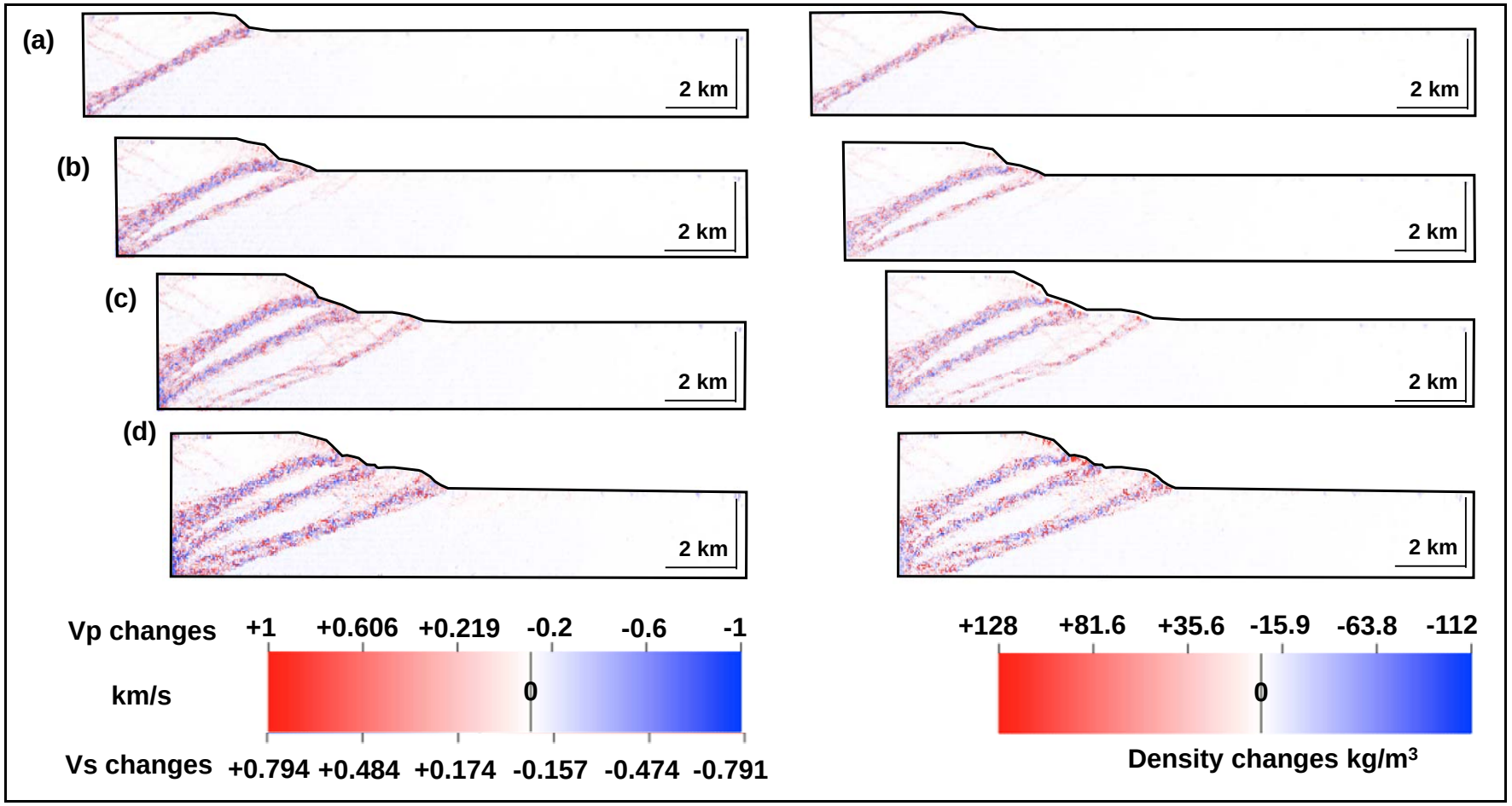

Figure 17. *Change of seismic velocities and density for Model 1 after (a) 1.25, (b) 2.5, (c) 3.75 and (d) 5 km shortening.*

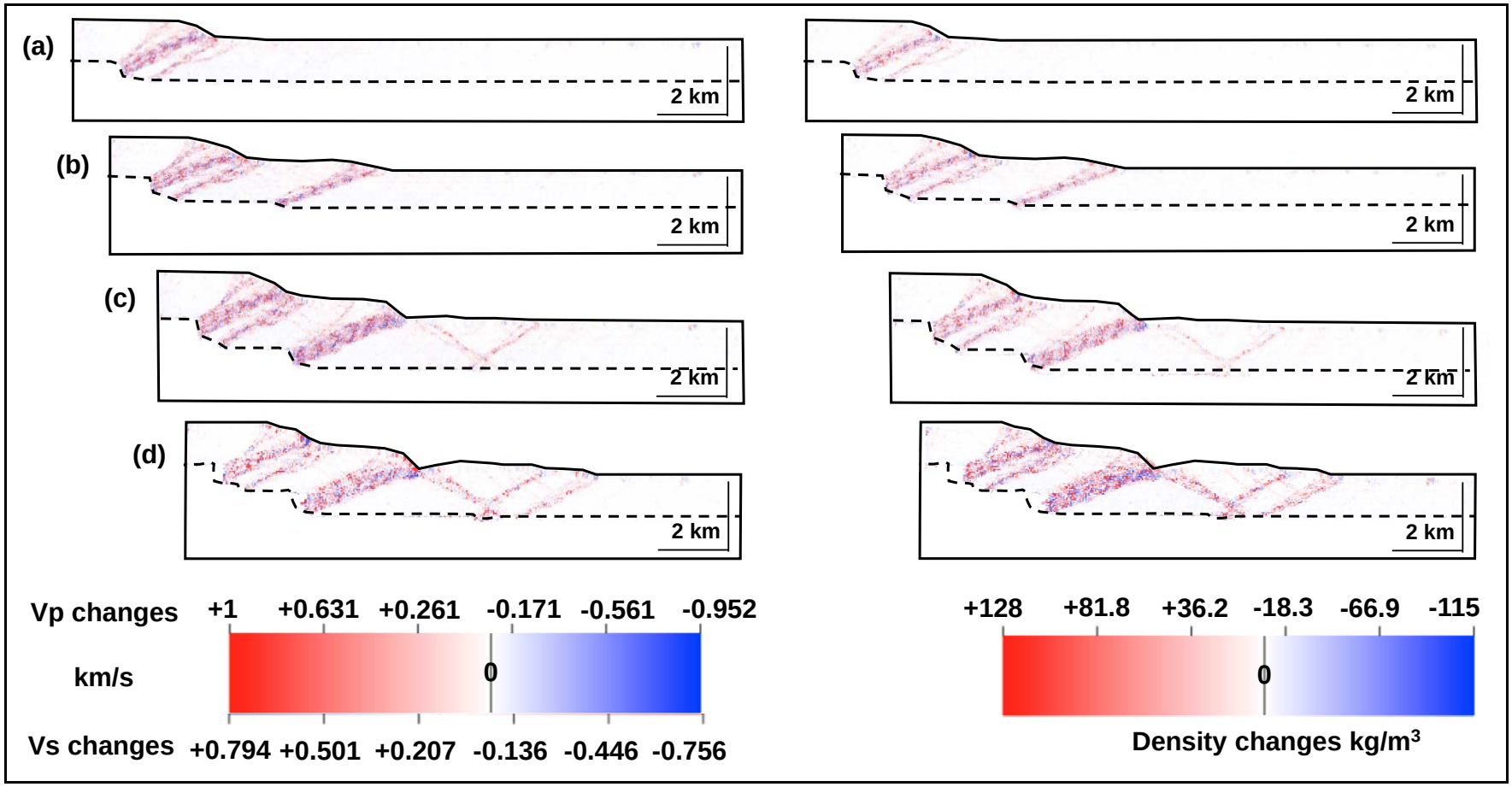

Figure 18. *Change of seismic velocities and density for Model 2 after (a) 1.25, (b) 2.5, (c) 3.75 and (d) 5 km shortening.*

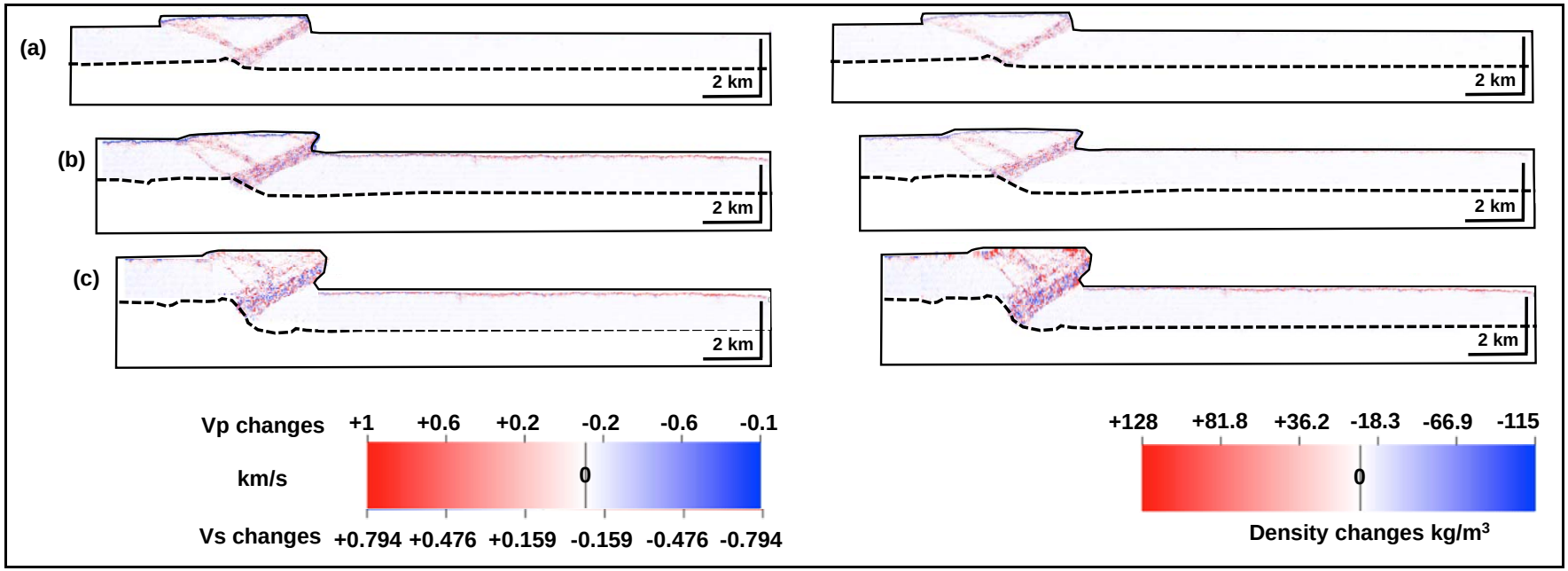

Figure 19. *Change of seismic velocities and density for Model 3 after (a) 1, (b) 2, and (c) 3 km shortening.*

3.3 Simulated seismic images

To compute the corresponding reflectivity grid with zero-incident angle (Figure 8a), the values of density and seismic velocities (Figure 17, 18 and 19) after different stages of shortening (1.25, 2.5, 3.5 and 5 km) are selected to forward model seismic images for Models 1 and 2, and after 1, 2 and 3 km shortening for Model 3, in order to understand the impact of deformation on the resulting seismic images. For seismic modeling, the brittle cover is considered as an interlayered sedimentary sequence and the interfaces corresponding to sandstone/shale, modified by thrust-related volumetric strain are input for each model (Figure 20). The shale layers are assigned low values of seismic velocities (Vp/Vs), and density (Figure 20; blue layers); while the sand layers (Figure 20; red layers) are assigned larger values (higher Vp/Vs, and density). Elastic properties for growth strata are slightly lower due to their less compaction. These elastic properties models allow computing the reflectivity grid input for seismic modeling. In order to model the seismic images, the survey consists of a 2D mono-streamer center at ≈ 10 km (center of the model – reference point), taking as an input the corresponding reflectivity grid for each model. The PSDM simulator was applied for a 1 km depth, homogeneous overburden corresponding to sandstone properties, three different illumination directions (specular, left and right side), and four wave frequencies from 10 to 40 Hz. With the PSDM simulator, it is also possible to test different model parameters (wave frequency and illumination direction) to see their impact on the resulting seismic images, and evaluate their potential for predicting the thrust zones.

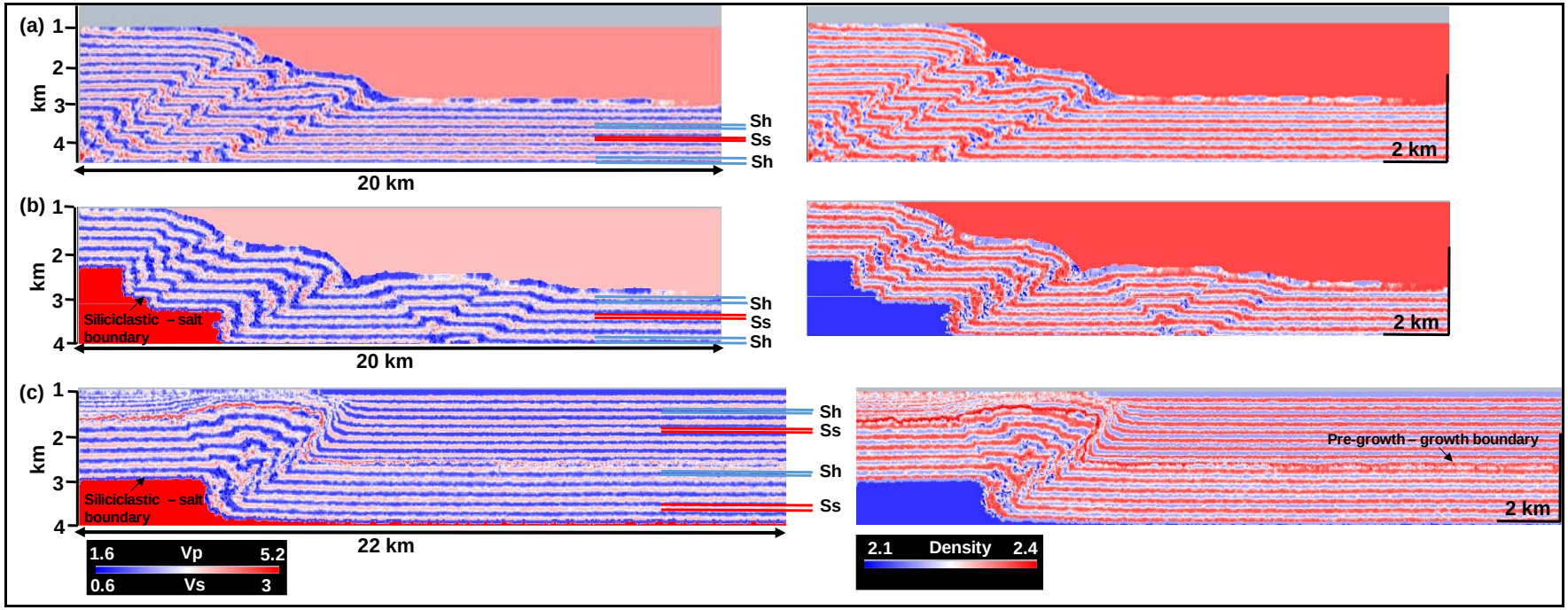

Figure 20. *Computed elastic properties Vp-Vs (left column), and density (right column) for (a) Model 1 (b) Model 2, and (c) Model 3. Note the pre-growth interlayered sedimentary sequences in Model 1 and 2, and the pre-growth/growth interlayered sequences in Model 3. Sh and Ss correspond to shale and sandstone layers, respectively.*

3.3.1 Impact of illumination direction

Illumination direction (specular, left, and right side) provides essential information of the dip and azimuth of the potentially illuminated reflectors (Figure 21), and consequently has a relevant impact on the total illuminated volume of the compressional folds in the seismic images.

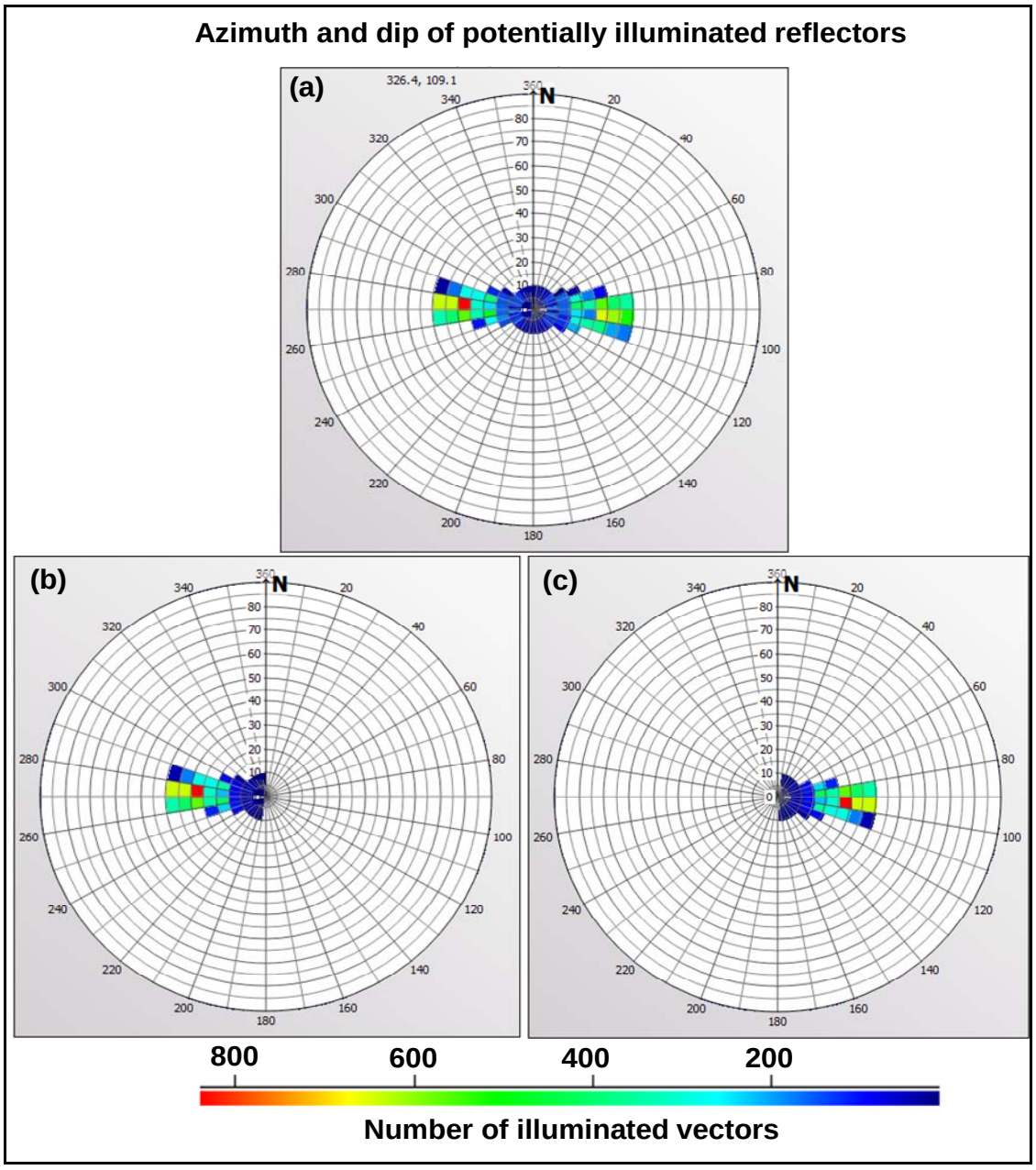

Figure 21. *Illumination direction plots showing both dip and azimuth of the potentially illuminated reflectors at the center of the target for (a) specular illumination (b) left and (c) right side illumination.*

Illumination vectors are computed at a given reference point (center of the models) (Lecomte, 2008), and ray tracing in all cases obtains illumination designs as seen in Figure 21. Specular illumination (following Snell's law) is potentially good to illuminate flat reflectors, since these reflectors are normal to the illumination vectors. Therefore, for specular illumination (Figure 21a), horizontal reflectors will control the simulated seismic images. On the other hand, in the case of left and right side illumination, the wave propagation relates to different directions, avoiding the specular energy from the flat reflectors (Figure 21b-c).

3.3.1.1 Model 1

Seismic imaging with specular illumination after 1.25 (Figure 22) and 2.5 km shortening (Figure 24), show very low amplitude values, especially at higher frequencies (30 and 40 Hz; Figure 22-24c-d) where the sedimentary sequence has less impact. Although, the thrusts give an indication on the images, their associated folds are difficult to interpret, due to the low seismic resolution. This is because in these earlier stages the model is less deformed, experienced less strain, hence less impact on the resulting seismic images. On the other hand, side illumination (right and left side) at the stages of shortening reported (1.25 km - Figure 23; 2.5 km - Figure 25), highlights directly the thrusts and their related folds. However, due to their low resolution is difficult to interpret internal details of the thrust zones through the sedimentary sequence.

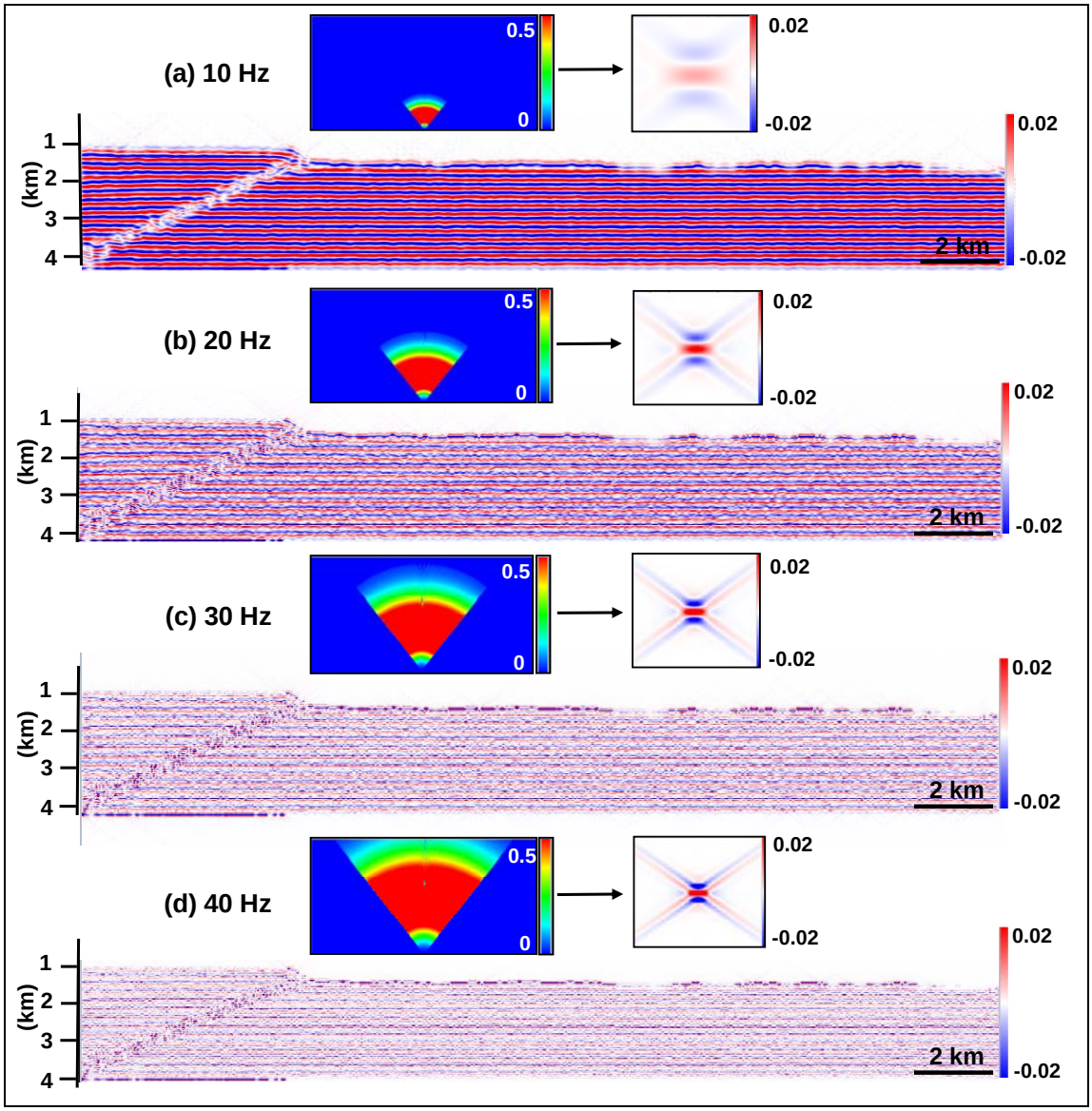

Figure 22. *PSDM seismic images of Model 1 after 1.25 km shortening with specular illumination. The seismic images were generated with different frequencies of a zero-phase Ricker pulse: (a) 10 Hz, (b) 20 Hz, (c) 30 Hz and (d) 40 Hz. At the top of every image, their equivalent PSDM filter and resulting point spread function PSF are shown.*

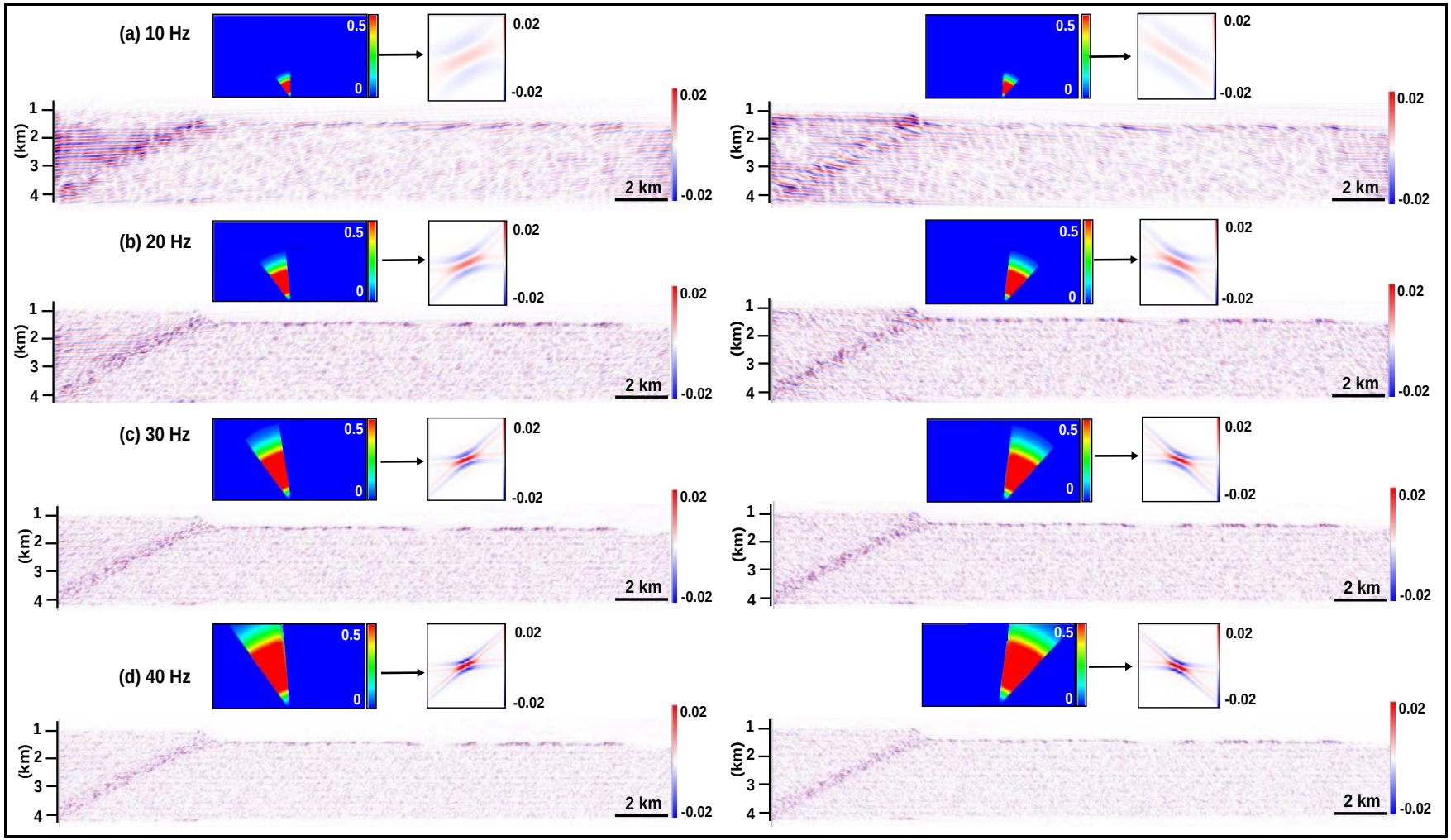

Figure 23. *PSDM seismic images of Model 1 after 1.25 km shortening with left (left column) and right (right column) side illuminations. The seismic images were generated with different frequencies of a zero-phase Ricker pulse: (a) 10 Hz, (b) 20 Hz, (c) 30 Hz and (d) 40 Hz. At the top of every image, their equivalent PSDM filter and resulting point spread function PSF are shown.*

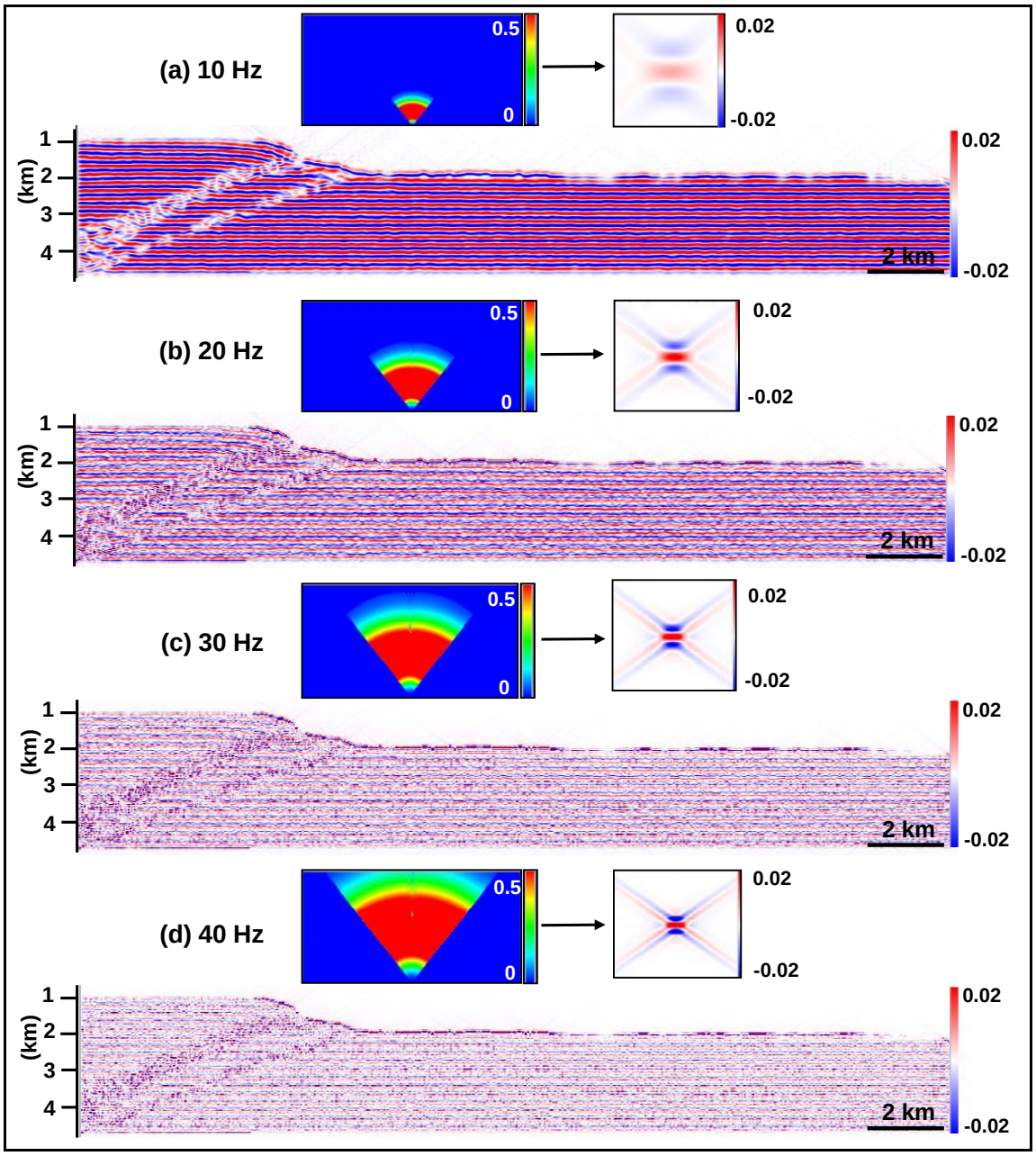

Figure 24. *PSDM seismic images of Model 1 after 2.5 km shortening with specular illumination. The seismic images were generated with different frequencies of a zero-phase Ricker pulse: (a) 10 Hz, (b) 20 Hz, (c) 30 Hz and (d) 40 Hz. At the top of every image, their equivalent PSDM filter and resulting point spread function PSF are shown.*

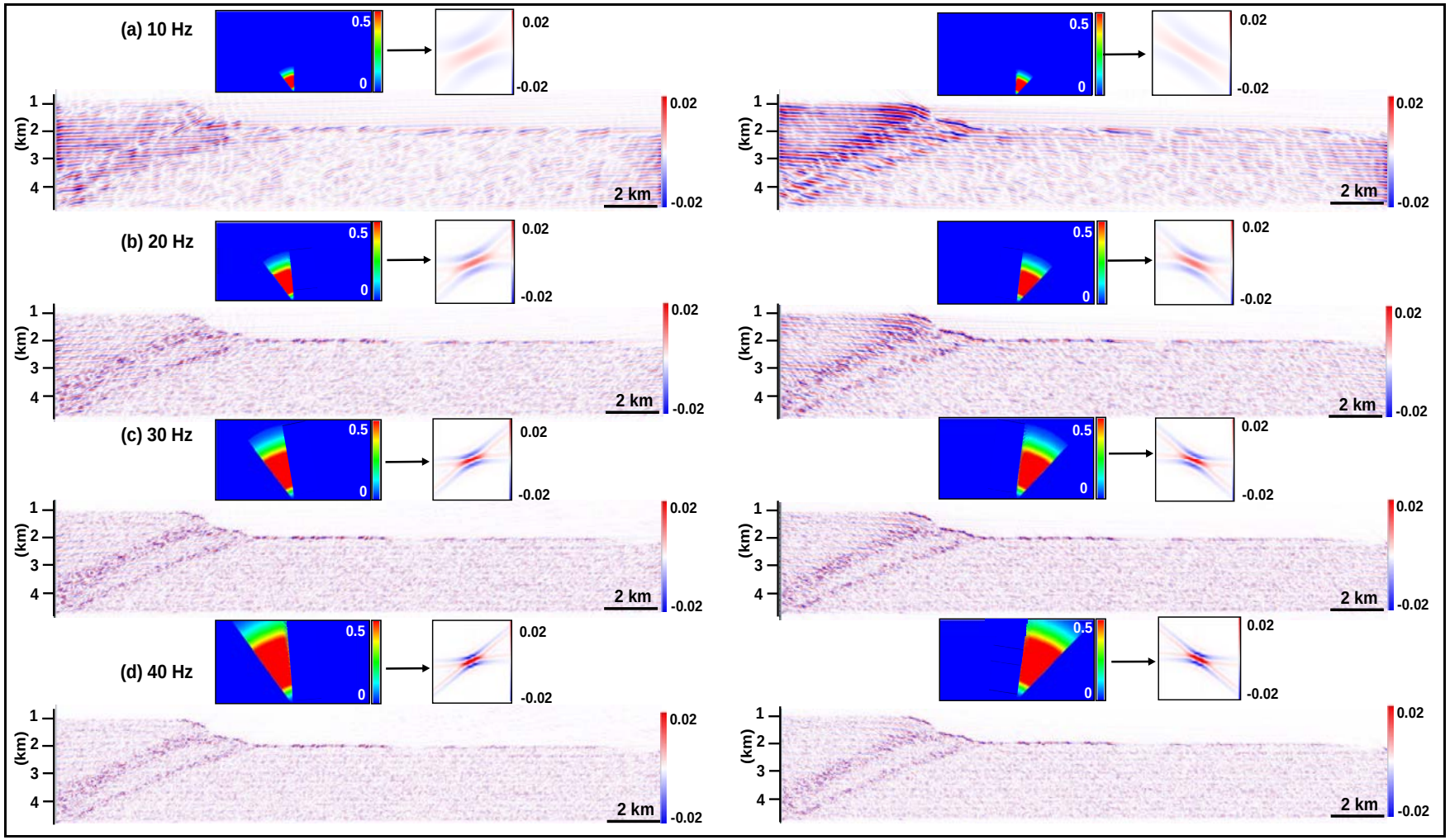

Figure 25. *PSDM seismic images of Model 1 after 2.5 km shortening with left (left column) and right (right column) side illuminations. The seismic images were generated with different frequencies of a zero-phase Ricker pulse: (a) 10 Hz, (b) 20 Hz, (c) 30 Hz and (d) 40 Hz. At the top of every image, their equivalent PSDM filter and resulting point spread function PSF are shown.*

Seismic imaging after 3.75 km shortening with specular illumination (Figure 26) highlights the improvement of seismic resolution due to the high volumetric strain experienced at this stage. The thrusts and associated folding are better observed by their higher diffraction energy on the seismic images through the sedimentary sequence, especially at higher frequencies (30 and 40 Hz; Figure 26c-d). Right and left side illuminations (Figure 27) target directly the thrust zones, allowing to interpret major internal details, due to the higher amplitudes displayed, in comparison to the earlier stages. However, the observations and interpretations (considered below) of the change of wave frequency and illumination direction are evaluated directly on the seismic images after 5 km shortening (Figure 28-33) where the model is deformed and complex enough, to investigate on seismic. Furthermore, since seismic resolution is better at this stage, it is possible to assess the potential of the different seismic images to predict internal structures and properties of the compressional folds.

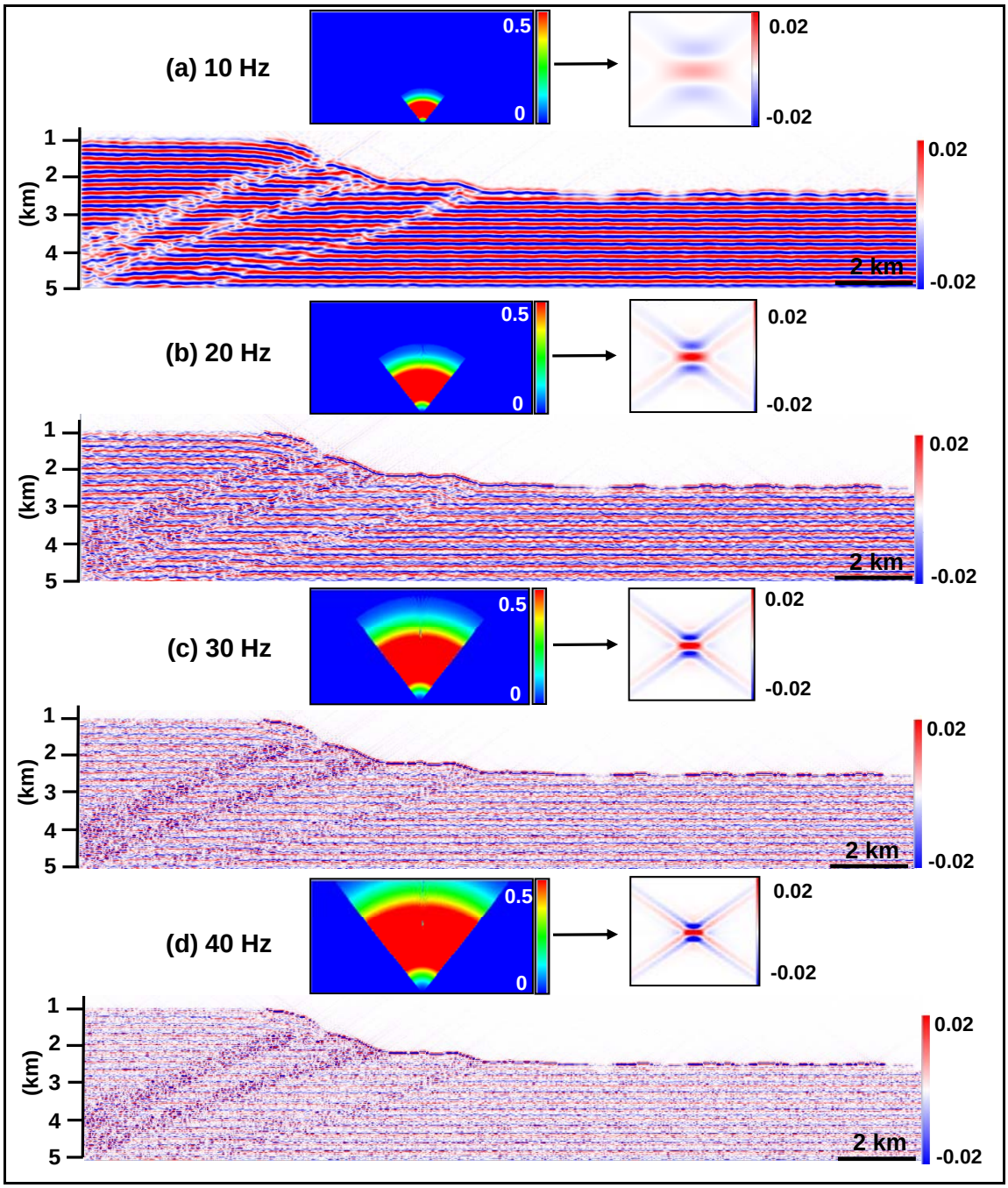

Figure 26. *PSDM seismic images of Model 1 after 3.75 km shortening with specular illumination. The seismic images were generated with different frequencies of a zero-phase Ricker pulse: (a) 10 Hz, (b) 20 Hz, (c) 30 Hz and (d) 40 Hz. At the top of every image, their equivalent PSDM filter and resulting point spread function PSF are shown.*

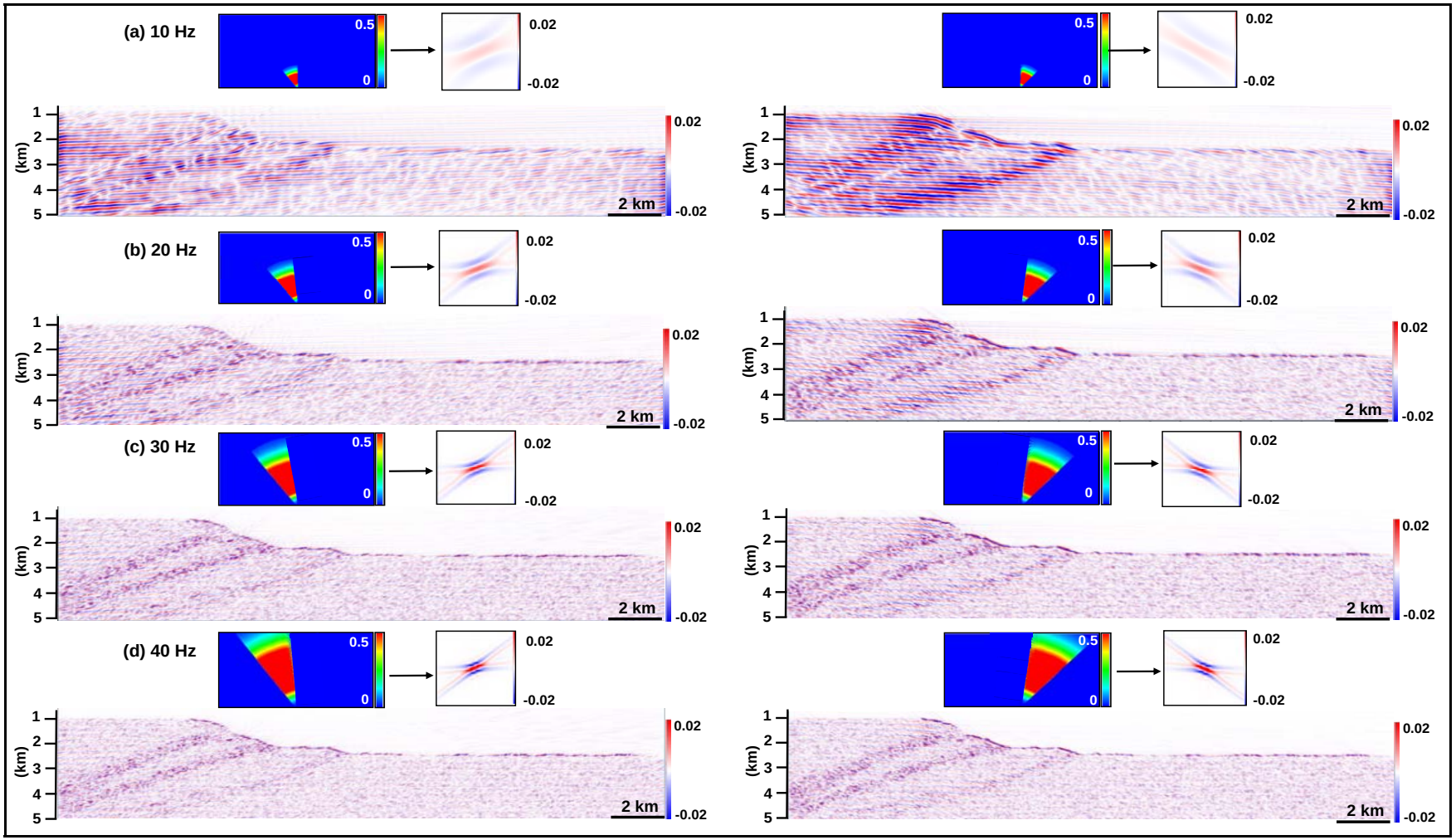

Figure 27. *PSDM seismic images of Model 1 after 3.75 km shortening with left (left column) and right (right column) side illuminations. The seismic images were generated with different frequencies of a zero-phase Ricker pulse: (a) 10 Hz, (b) 20 Hz, (c) 30 Hz and (d) 40 Hz. At the top of every image, their equivalent PSDM filter and resulting point spread function PSF are shown.*

Seismic imaging of Model 1 after 5 km shortening with specular illumination highlights flat reflectors corresponding to sandstone/shale interfaces outside of the most deformed zones (Figure 28-29). The larger thrusts are mainly visible by breaks, and offsets of the reflectors especially at 10 Hz (Figure 28-29a). At higher frequencies (20, 30 and 40 Hz; Figures 28-29b-c-d), some seismic energy associated to diffractions from the thrusts and associated folds is visible, making easier to interpret the thrusts. At higher frequencies, the interfaces in the siliciclastic sequence have less impact, in comparison to the low frequency image (Figure 28-29a). For offside illumination, seismic images were simulated for the thrust zones only. Right side illumination at 10 Hz (Figure 30-31a) gives a good indication of the fold structures, rather than thrust displacement. Higher frequencies (20, 30 and 40 Hz; Figure 30-31b-c-d) instead, target directly the zone of the hanging wall anticline of each thrust, making possible to have an internal detail of the thrust zones through the siliciclastic sequence. Illumination from the left side at 10 Hz (Figure 32-33a) gives some indication of the thrusts, due to the truncation of the flat reflectors. However, they are displayed as simple and planar structures. At higher frequencies (20, 30 and 40 Hz; Figure 32-33b-c-d), the diffracted energy from the thrust and associated folds allows a better characterization of these structures. Notably, offside illumination at high frequencies produces low amplitude for zones with low deformation. Hence, it is easier to associate the higher amplitudes with the diffracted energy emitted directly from the hanging wall anticline of each thrust, and this can be used as a guideline to interpret, and have an idea of the internal detail of the fault zones through the siliciclastic sequence. These areas of higher amplitudes are related precisely to the highest strain zones in the geomechanical model (Figure 11). Thus, these areas experienced more drastic changes in seismic velocities, and density (Figure 17d), which are reflected directly on the seismic images.

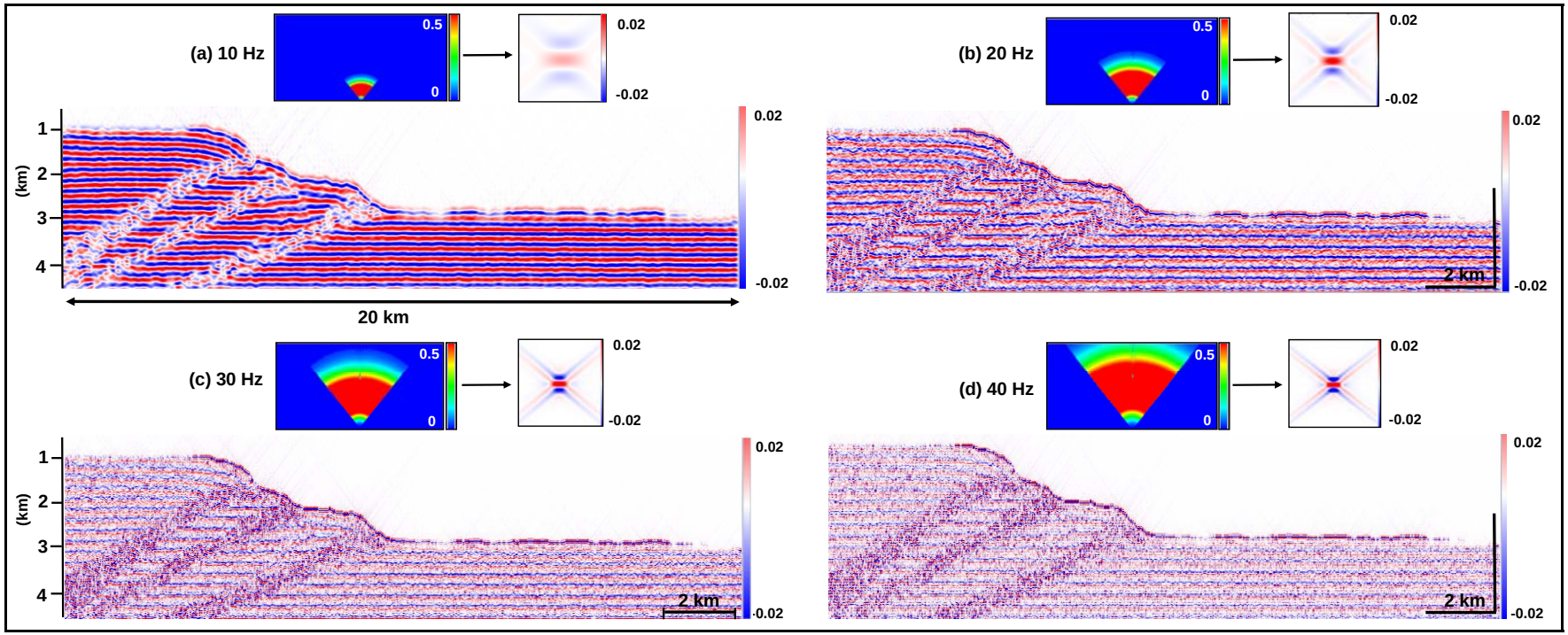

Figure 28. *PSDM seismic images of Model 1 after 5 km shortening with specular illumination (without interpretation). The seismic images were generated with different frequencies of a zero-phase Ricker pulse: (a) 10 Hz, (b) 20 Hz, (c) 30 Hz and (d) 40 Hz. At the top of every image, their equivalent PSDM filter and resulting point spread function PSF are shown.*

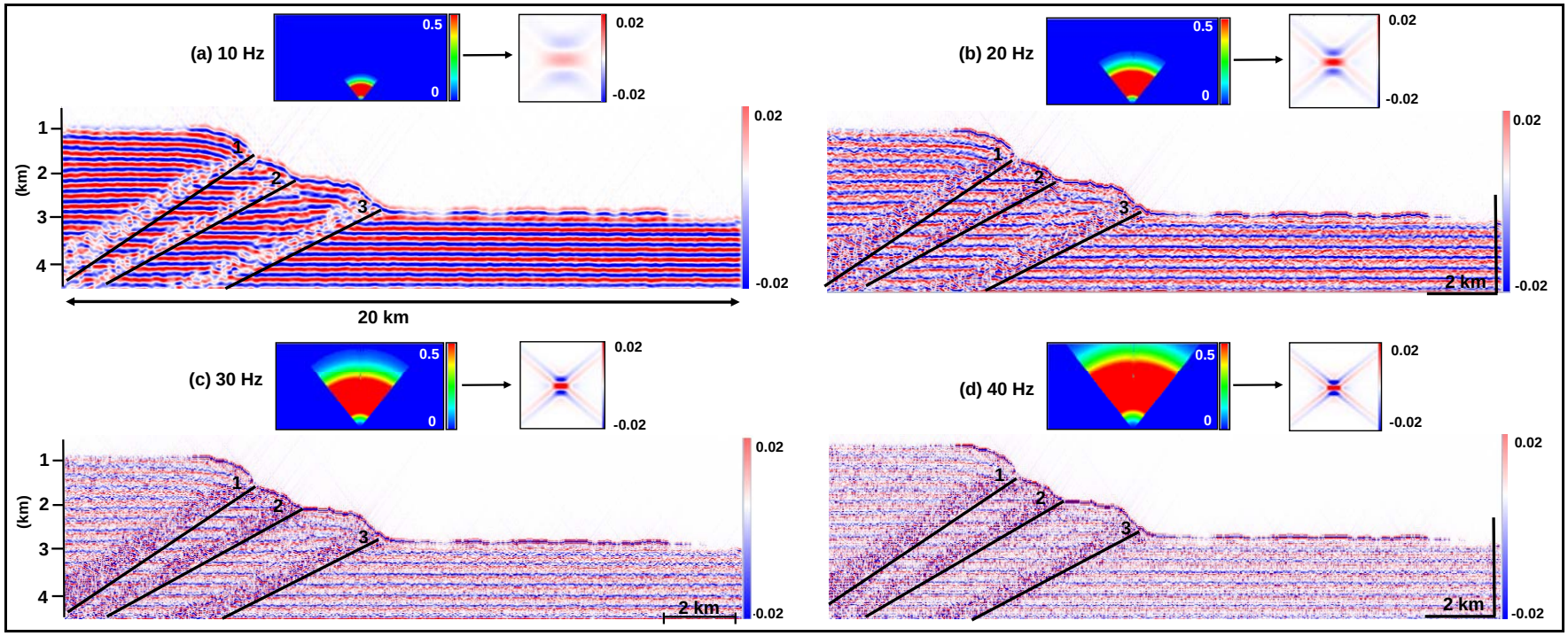

Figure 29. *Interpreted PSDM seismic images of Model 1 after 5 km shortening with specular illumination.*

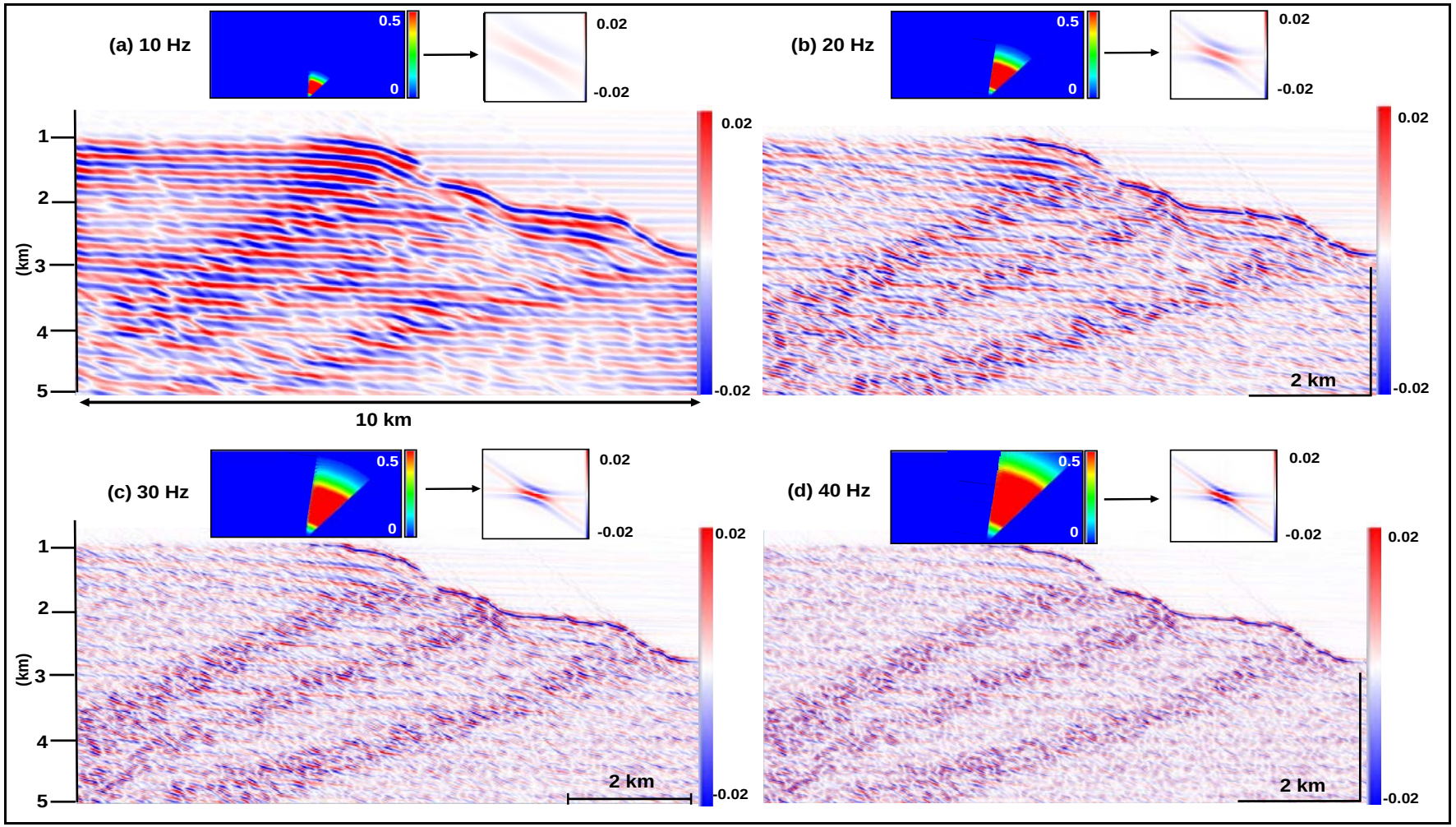

Figure 30. *PSDM seismic images of Model 1 after 5 km shortening with right-side illumination (without interpretation). The seismic images were generated with different frequencies of a zero-phase Ricker pulse: (a) 10 Hz, (b) 20 Hz, (c) 30 Hz and (d) 40 Hz. At the top of every image, their equivalent PSDM filter and resulting point spread function PSF are shown.*

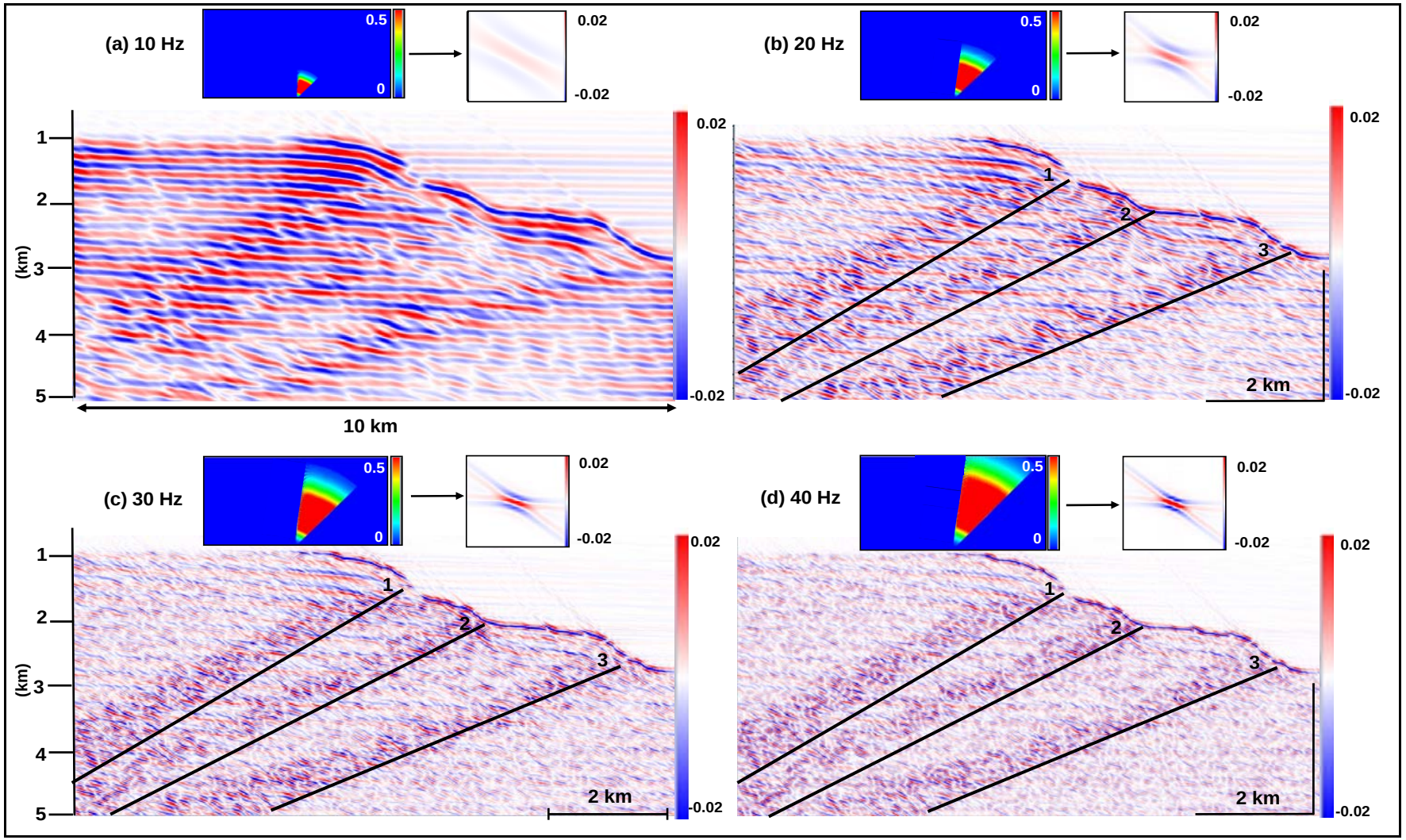

Figure 31. *Interpreted PSDM seismic images of Model 1 after 5 km shortening with right-side illumination.*

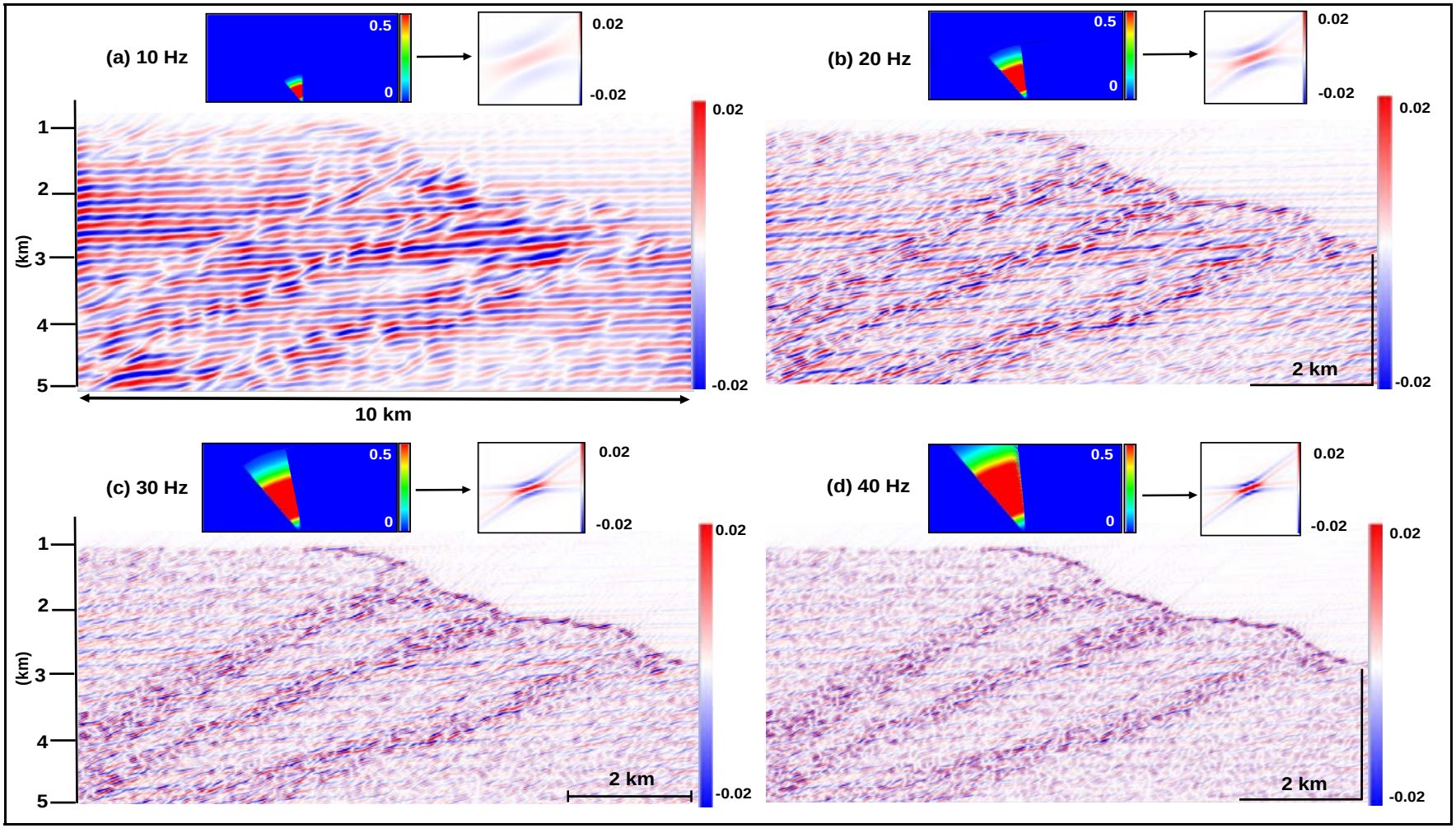

Figure 32. *PSDM seismic images of Model 1 after 5 km shortening with left-side illumination (without interpretation). The seismic images were generated with different frequencies of a zero-phase Ricker pulse: (a) 10 Hz, (b) 20 Hz, (c) 30 Hz and (d) 40 Hz. At the top of every image, their equivalent PSDM filter and resulting point spread function PSF are shown.*

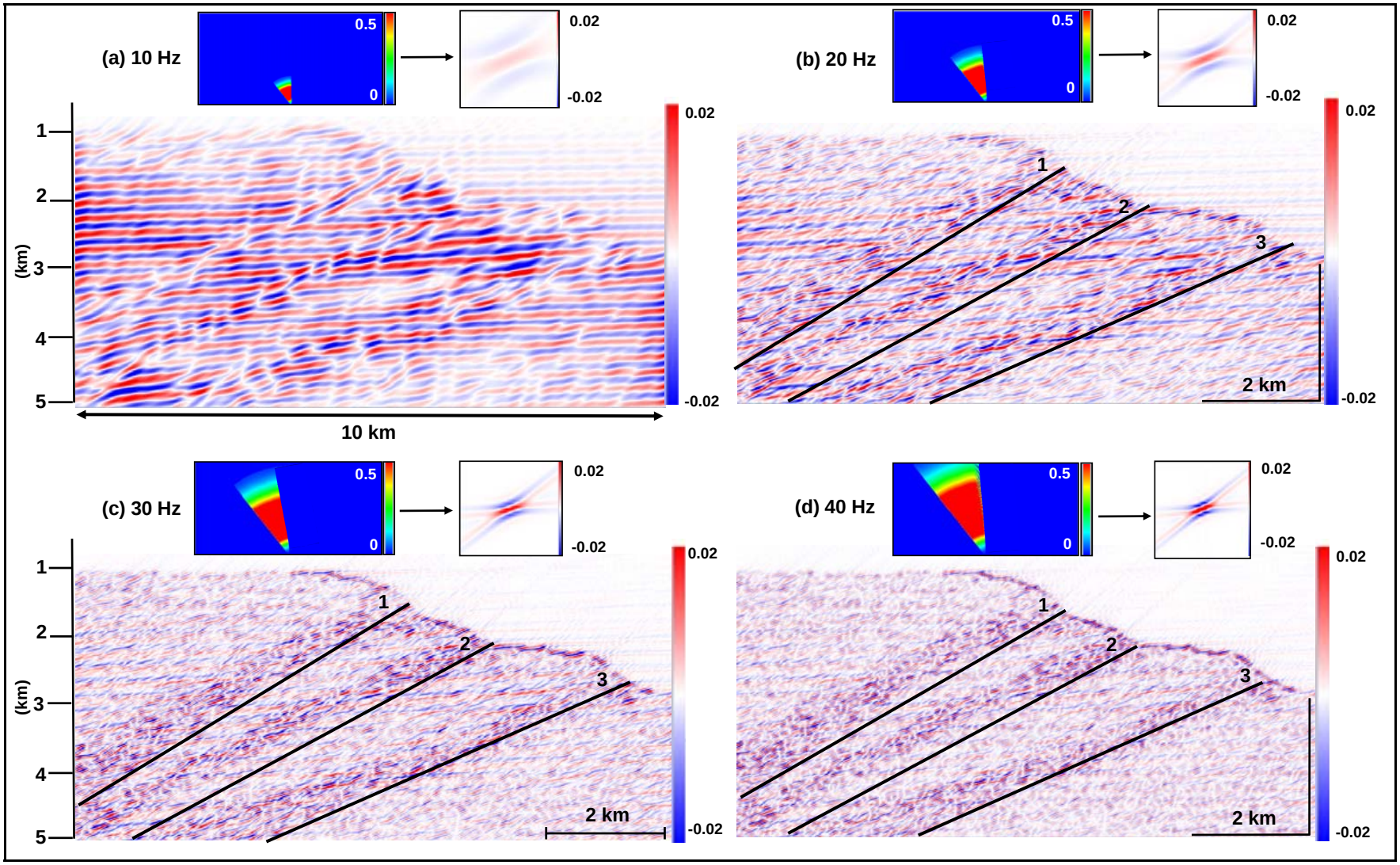

Figure 33. *Interpreted PSDM seismic images of Model 1 after 5 km shortening with left-side illumination.*

3.3.1.2 Model 2

Seismic imaging with specular illumination after 1.25 km (Figure 34) and 2.5 km (Figure 36) shortening show the general aspects of the seismic images at these stages for Model 2. The images have low resolution that do not allow major interpretations. In addition, the evolution of the compressional folds from the salt-siliciclastic contact and through the siliciclastic sequence, is in the initial phase, resulting in less impact of these zones on the seismic images. Right and left side illumination targets the thrusts and associated folding on the seismic images (1.25 km - Figure 35; 2.5 km - Figure 37). Therefore, the higher amplitudes displayed are associated directly to the thrust zones. However, the resolution is low due to the low volumetric strain experienced at these stages, leading to a low seismic characterization of these zones.

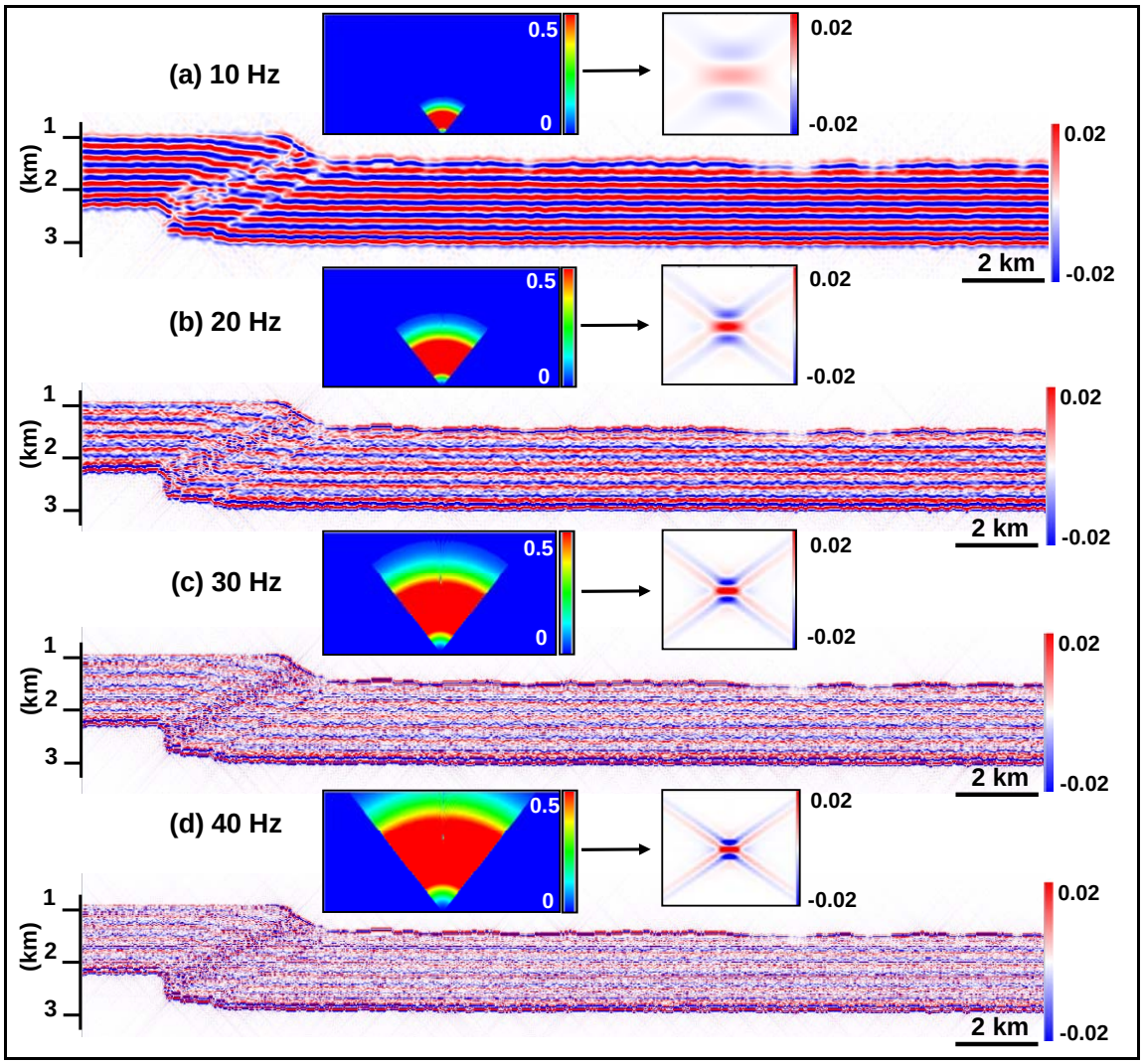

Figure 34. *PSDM seismic images of Model 2 after 1.25 km shortening with specular illumination. The seismic images were generated with different frequencies of a zero-phase Ricker pulse: (a) 10 Hz, (b) 20 Hz, (c) 30 Hz and (d) 40 Hz. At the top of every image, their equivalent PSDM filter and resulting point spread function PSF are shown.*

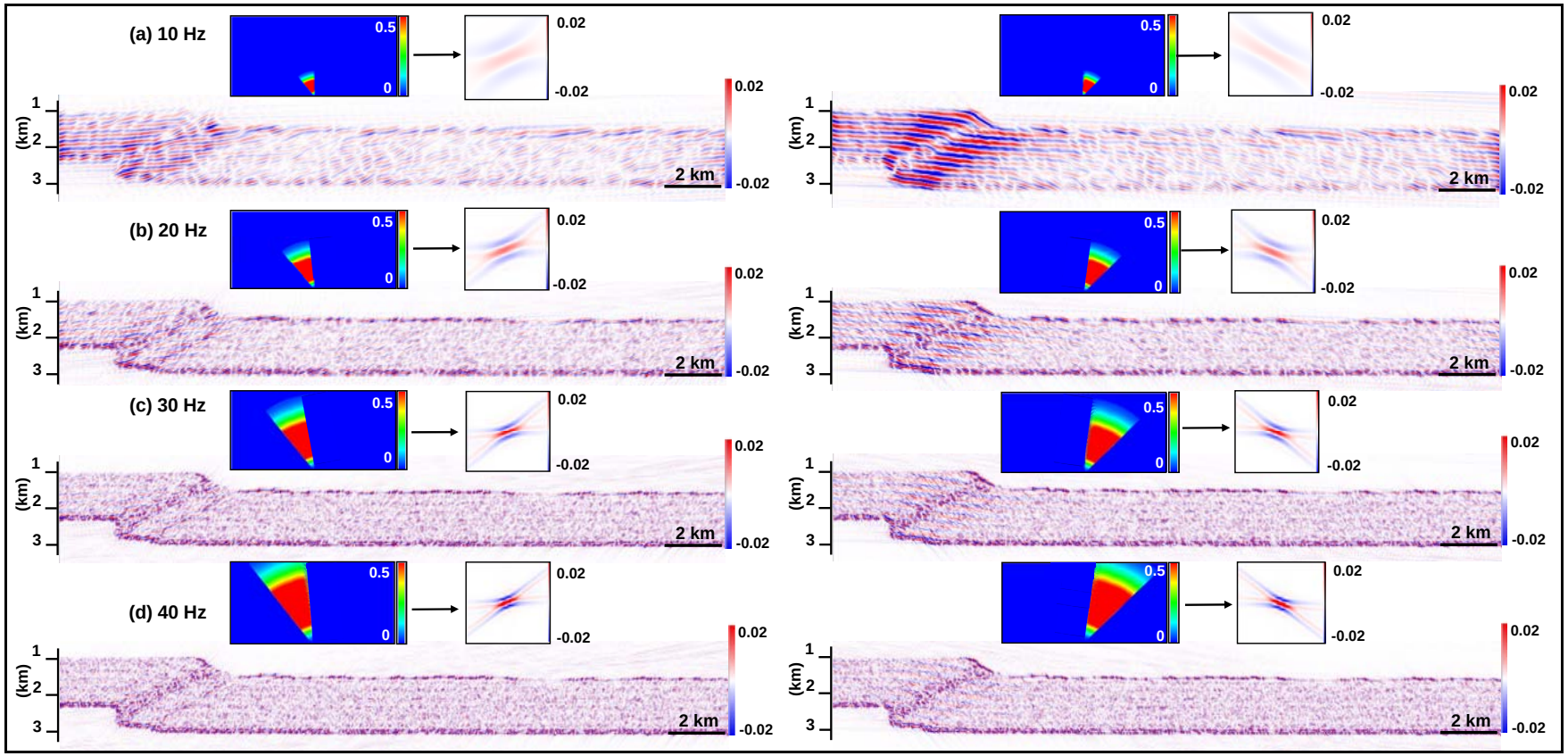

Figure 35. *PSDM seismic images of Model 2 after 1.25 km shortening with left (left column) and right (right column) side illuminations. The seismic images were generated with different frequencies of a zero-phase Ricker pulse: (a) 10 Hz, (b) 20 Hz, (c) 30 Hz and (d) 40 Hz. At the top of every image, their equivalent PSDM filter and resulting point spread function PSF are shown.*

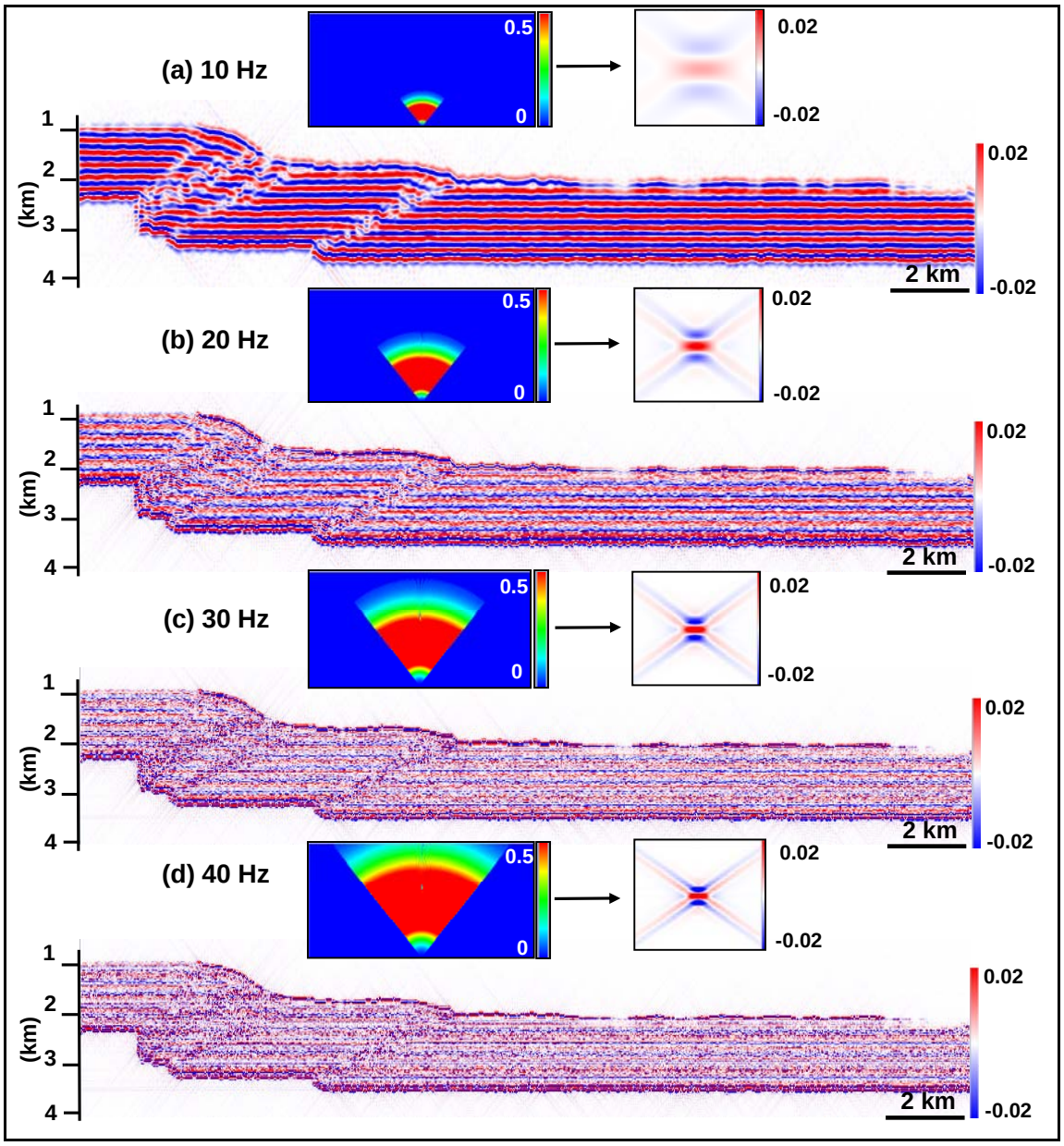

Figure 36. *PSDM seismic images of Model 2 after 2.5 km shortening with specular illumination. The seismic images were generated with different frequencies of a zero-phase Ricker pulse: (a) 10 Hz, (b) 20 Hz, (c) 30 Hz and (d) 40 Hz. At the top of every image, their equivalent PSDM filter and resulting point spread function PSF are shown.*

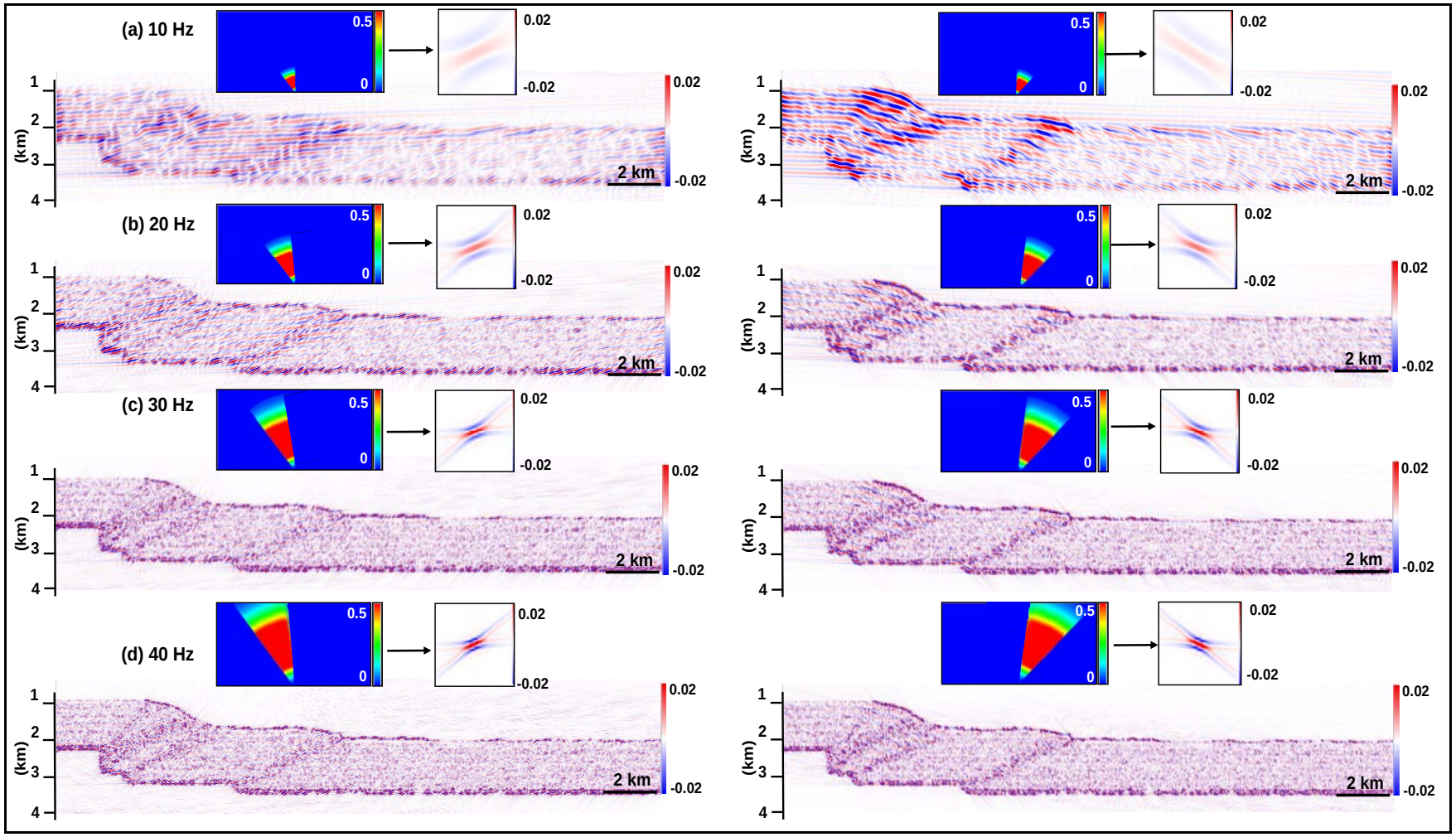

Figure 37. *PSDM seismic images of Model 2 after 2.5 km shortening with left (left column) and right (right column) side illuminations. The seismic images were generated with different frequencies of a zero-phase Ricker pulse: (a) 10 Hz, (b) 20 Hz, (c) 30 Hz and (d) 40 Hz. At the top of every image, their equivalent PSDM filter and resulting point spread function PSF are shown.*

Seismic imaging with specular illumination after 3.75 (Figure 38) and 5 km shortening (Figure 40-41) are more remarkable, due their higher resolution, in comparison to the earlier stages. Since the deformation experienced on the thrust zones through the sedimentary sequence was higher at these phases, more volumetric strain was accrued in these zones, resulting in a better resolution of the thrusts on the seismic images. Side illumination (right and left side) at these stages (3.75 km – Figure 39; 5 km – Figure 42-49) highlights the thrust and related folds by their higher amplitudes; consequently, a better characterization of these zones is obtained. However, the evaluation of the results due to the change of illumination direction and wave frequency is investigated directly on the seismic images after 5 km shortening (considered below). At this final stage, seismic resolution and seismic amplitudes allow to have a better internal detail and control of the extent of the thrust zones from the salt-siliciclastic contact through the sedimentary sequence.

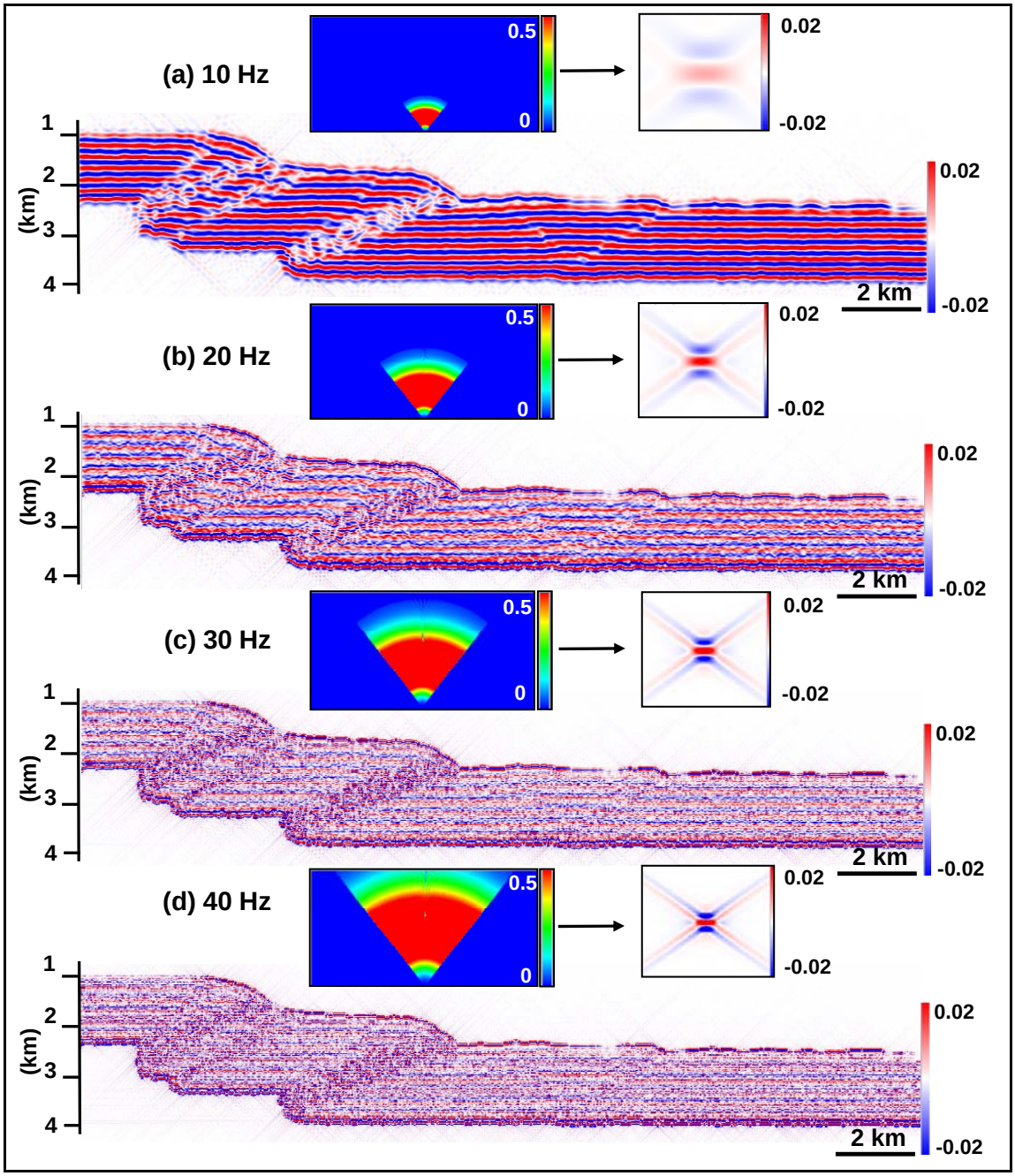

Figure 38. *PSDM seismic images of Model 2 after 3.75 km shortening with specular illumination. The seismic images were generated with different frequencies of a zero-phase Ricker pulse: (a) 10 Hz, (b) 20 Hz, (c) 30 Hz and (d) 40 Hz. At the top of every image, their equivalent PSDM filter and resulting point spread function PSF are shown.*

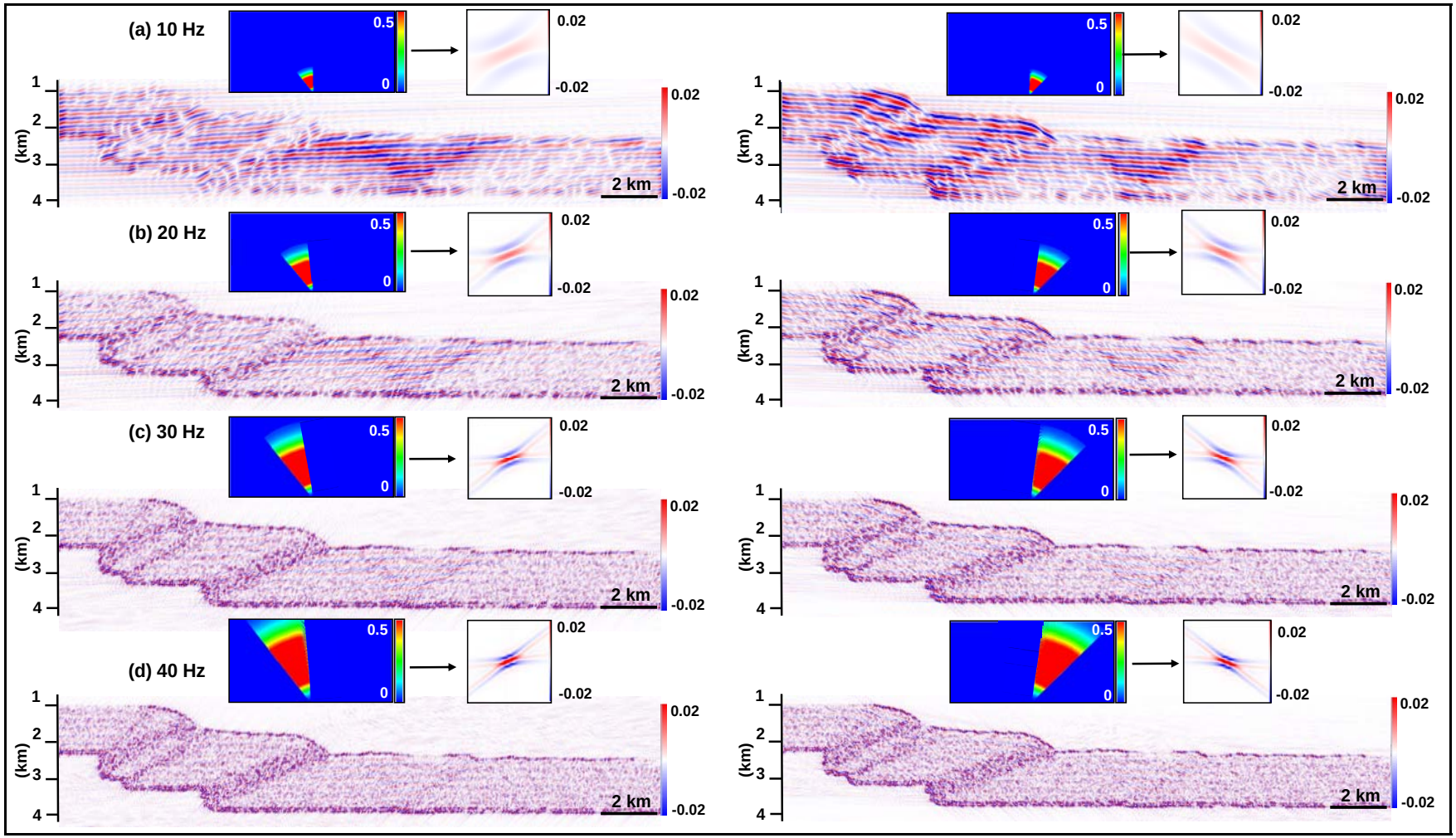

Figure 39. *PSDM seismic images of Model 2 after 3.75 km shortening with left (left column) and right (right column) side illuminations. The seismic images were generated with different frequencies of a zero-phase Ricker pulse: (a) 10 Hz, (b) 20 Hz, (c) 30 Hz and (d) 40 Hz. At the top of every image, their equivalent PSDM filter and resulting point spread function PSF are shown.*

Seismic imaging of Model 2 after 5 km shortening with specular illumination at 10 Hz (Figure 40-41a) highlights mostly flat reflectors corresponding to sandstone/shale interfaces and the salt/siliciclastic interface, giving a good indication of the overall structure. The thrusts are mainly visible due to the discontinuities generated in the flat reflectors. However, the fault related folds are hard to delimit, especially at the rear part of the model. With higher frequencies (20, 30 and 40 Hz; Figure 40-41b-c-d), the layered interfaces have less impact, and the thrusts and related folds are directly associated to higher diffraction on the seismic images. Therefore, these diffraction patterns make them easier to interpret. Right side illumination to the back of the FTB at 10 Hz (Figure 42-43a) illuminates the fold structures, but separation of the hanging and footwall sides of the thrust is difficult. Higher frequencies (20, 30 and 40 Hz; Figure 42-43b-c-d) highlight the thrusts and associated folds. Hence, it is possible to have an internal detail and better control of the extent of the thrust zones. Illumination towards the left side at 10 Hz gives some idea about the thrusts due to the truncation of the flat reflectors. However, their associated folds are difficult to evaluate (Figure 44-45a). Higher frequencies (20, 30 and 40 Hz; Figure 44-45b-c-d) show the diffracted energy from the thrusts and related folds, resulting in a better characterization. As observed in Model 1, offside illumination images at higher frequencies show high amplitudes at areas that experienced higher strain (Figure 13), which directly influences the resulting seismic images. These amplitude changes correlate with the amount of finite strain, with lower amplitudes in the less deformed zones, and higher amplitudes in the more deformed ones. Right side illumination for the front of the FTB at 10 Hz (Figure 46-47a) highlights the forelimbs of the folds. However, the information from the fore-thrusts and back-thrust related folds is not clear. Higher frequencies (20, 30 and 40 Hz; Figure 46-47b-c-d) target directly the fore-thrusts and related folds, making possible to interpret internal details of these structures. On the other hand, for left-side illumination at 10 Hz, the back-limb of the pop-up structure is highlighted rather than the forelimb (Figure 48-49a). Higher frequencies (20, 30 and 40 Hz; Figure 48-49b-c-d) result in a better characterization and higher diffracted energy from the back-thrust and related fold.

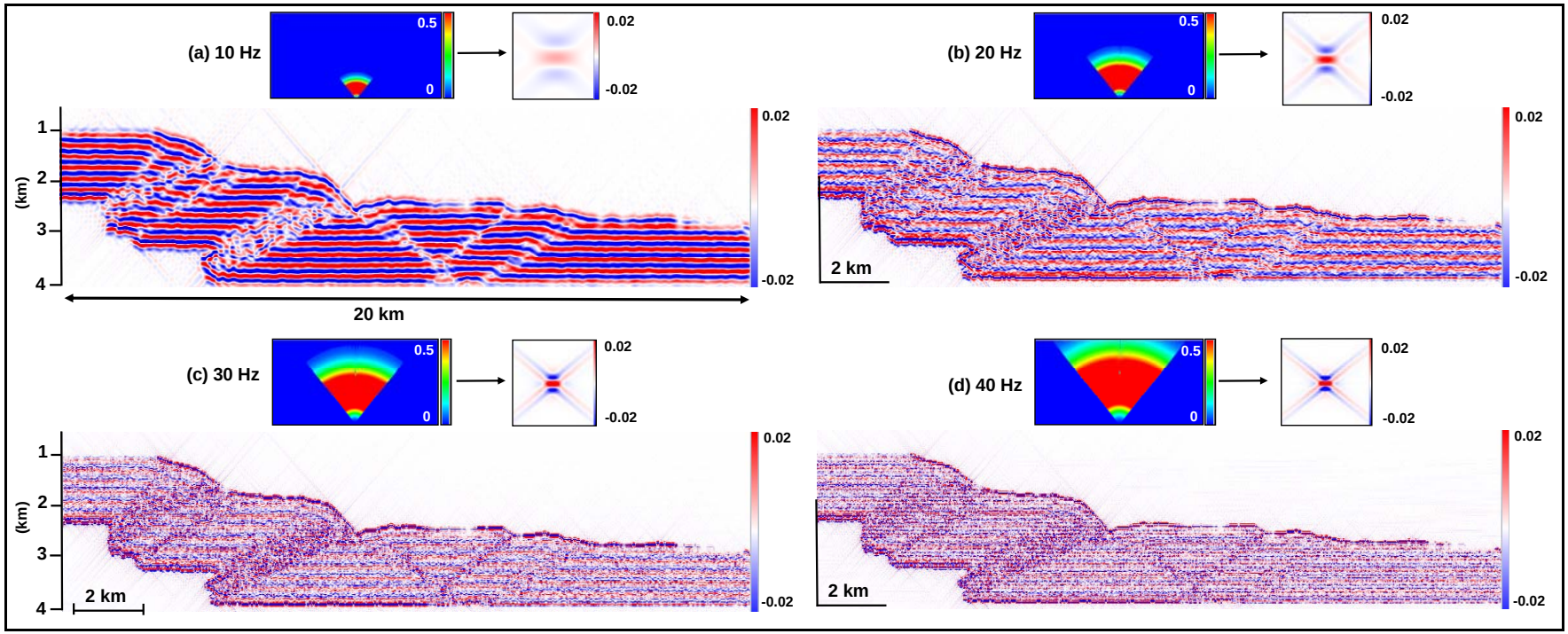

Figure 40. *PSDM seismic images of Model 2 after 5 km shortening with specular illumination (without interpretation). The seismic images were generated with different frequencies of a zero-phase Ricker pulse: (a) 10 Hz, (b) 20 Hz, (c) 30 Hz and (d) 40 Hz. At the top of every image, their equivalent PSDM filter and resulting point spread function PSF are shown.*

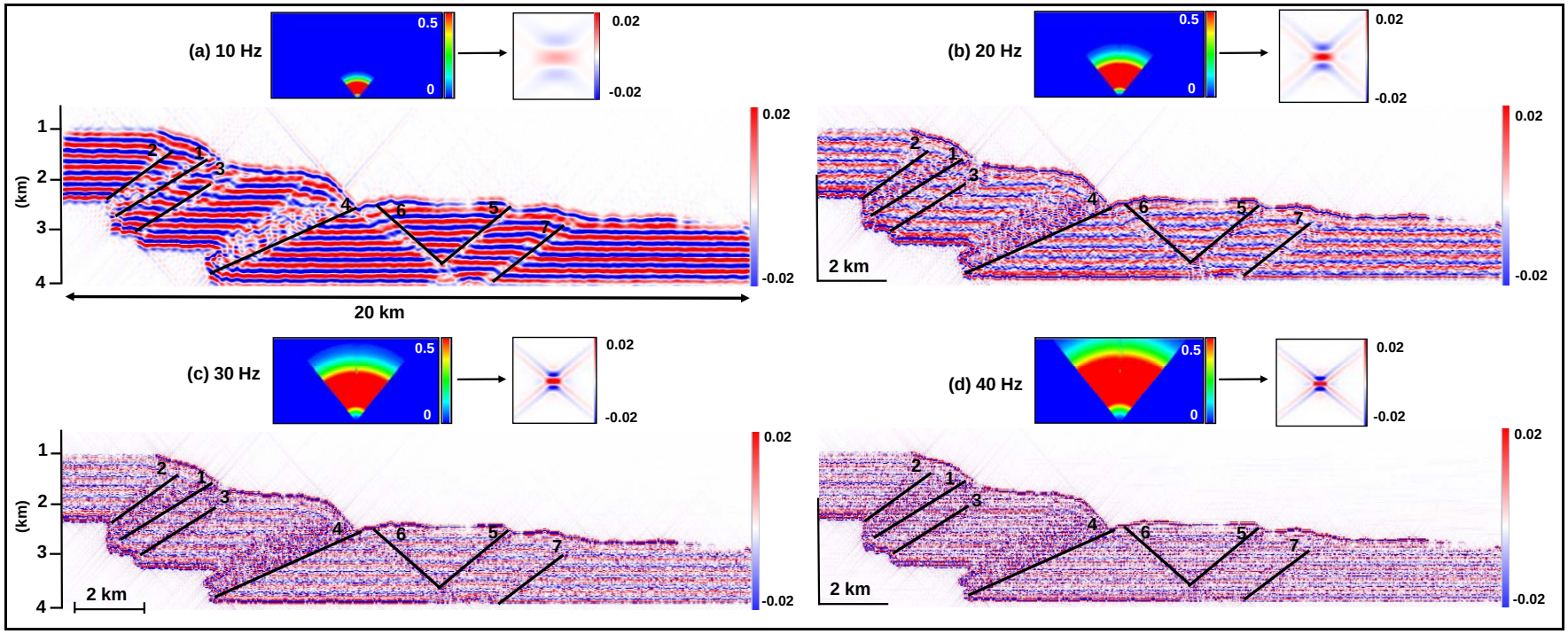

Figure 41. *Interpreted PSDM seismic images of Model 2 after 5 km shortening with specular illumination.*

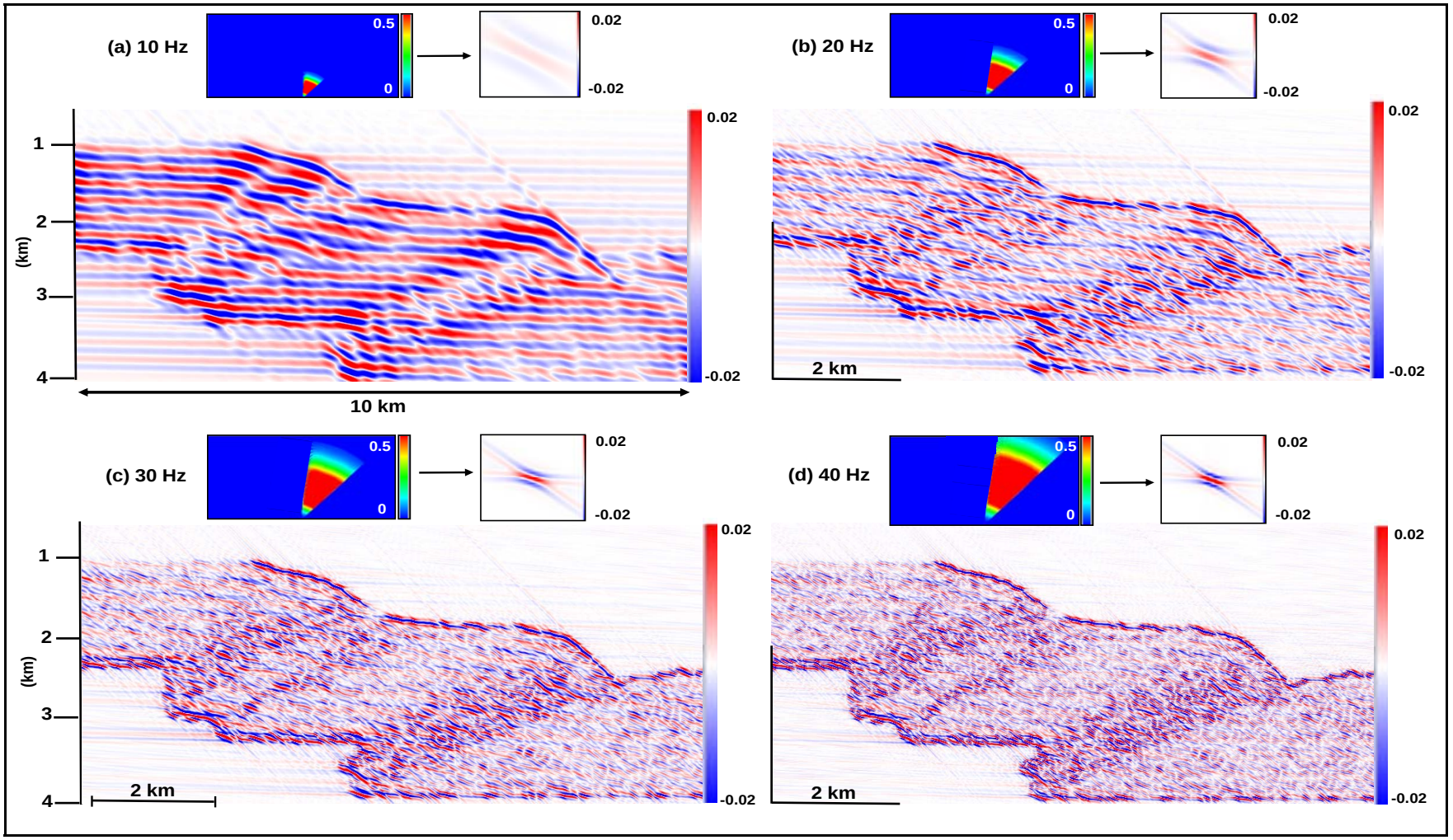

Figure 42. *PSDM seismic images of Model 2 (back of the FTB) after 5 km shortening with right-side illumination (without interpretation). The seismic images were generated with different frequencies of a zero-phase Ricker pulse: (a) 10 Hz, (b) 20 Hz, (c) 30 Hz and (d) 40 Hz. At the top of every image, their equivalent PSDM filter and resulting point spread function PSF are shown.*

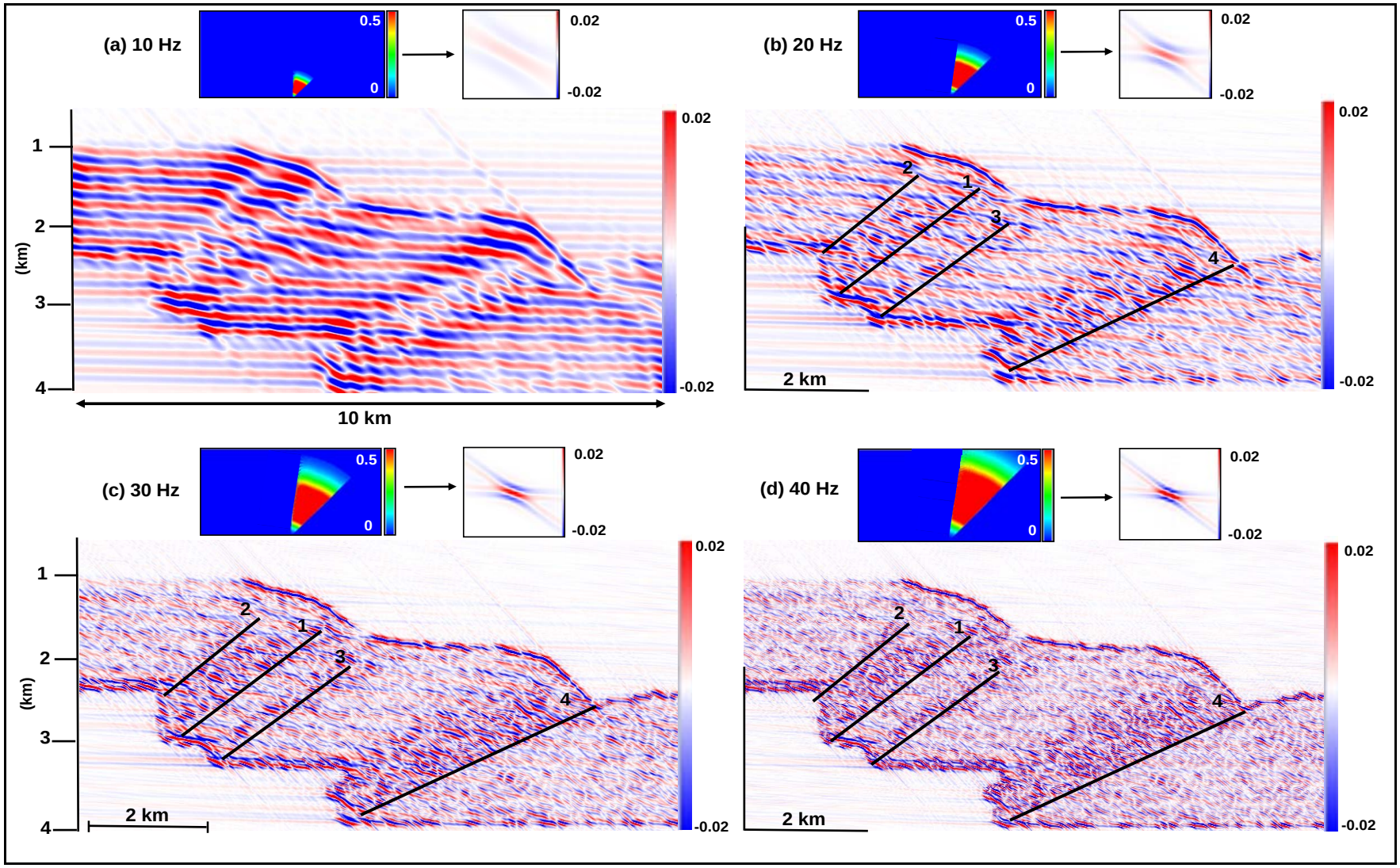

Figure 43. *Interpreted PSDM seismic images of Model 2 (back of the FTB) after 5 km shortening with right-side illumination.*

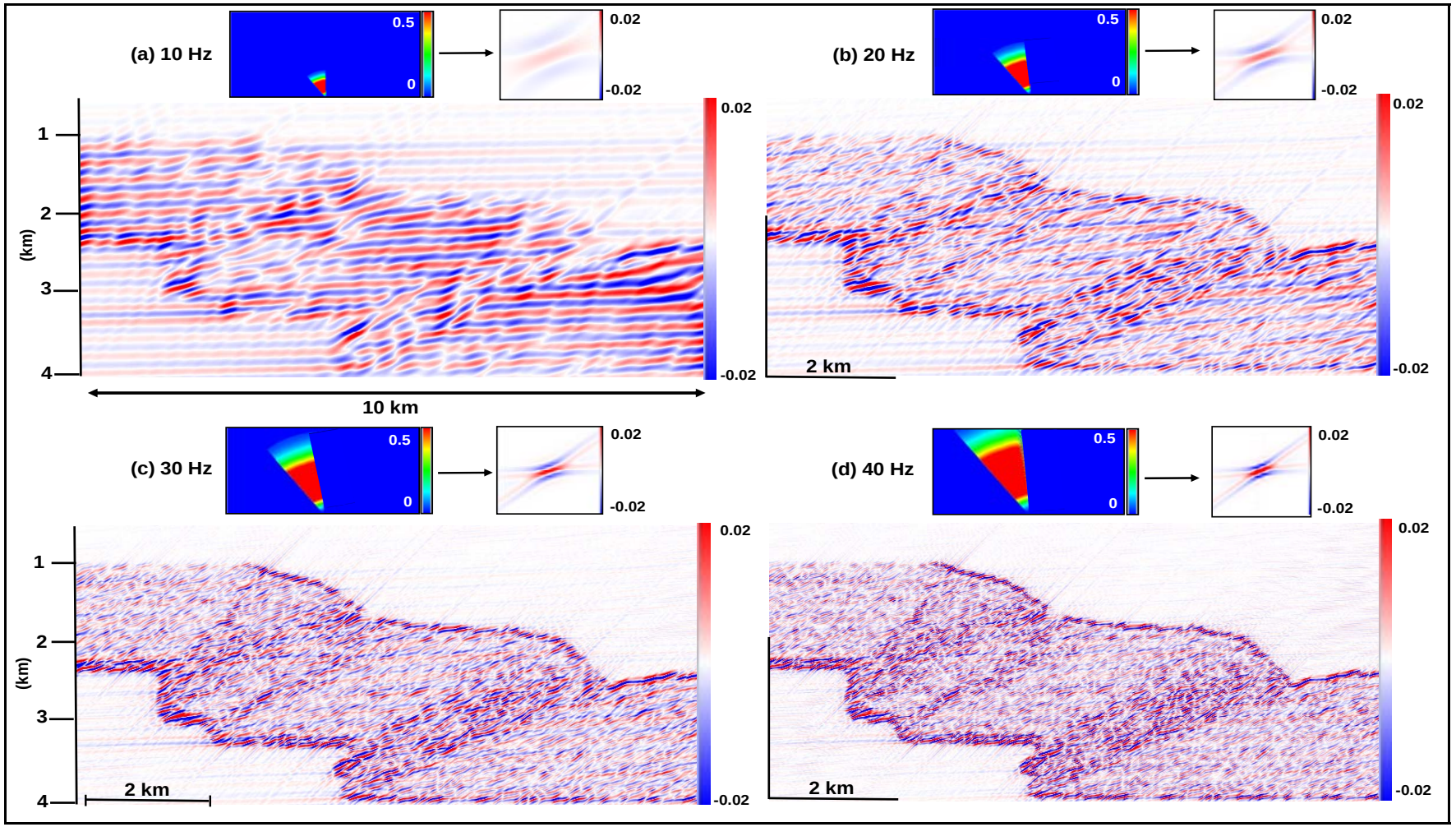

Figure 44. *PSDM seismic images of Model 2 (back of the FTB) after 5 km shortening with left-side illumination (without interpretation). The seismic images were generated with different frequencies of a zero-phase Ricker pulse: (a) 10 Hz, (b) 20 Hz, (c) 30 Hz and (d) 40 Hz. At the top of every image, their equivalent PSDM filter and resulting point spread function PSF are shown.*

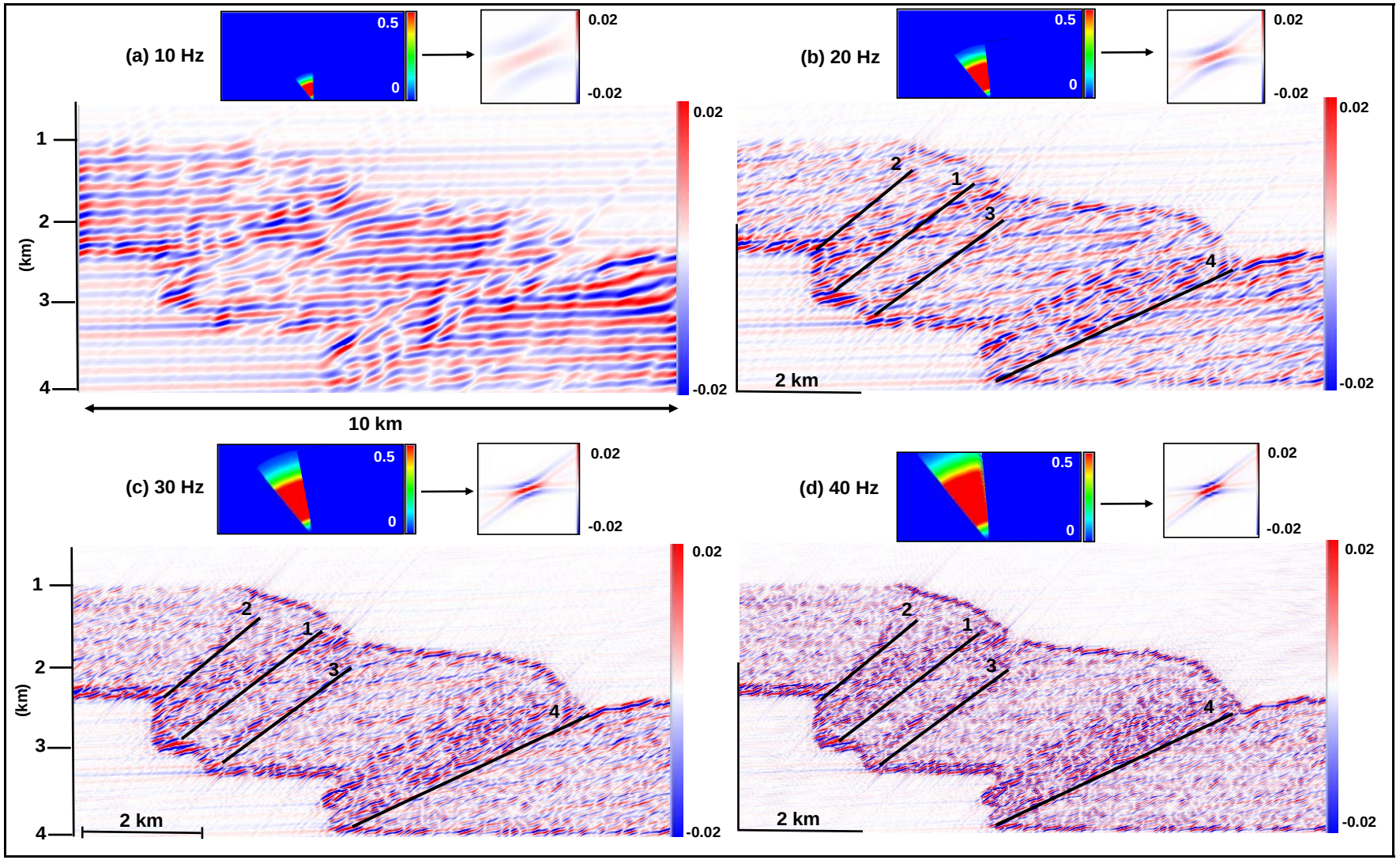

Figure 45. *Interpreted PSDM seismic images of Model 2 (back of the FTB) after 5 km shortening with left-side illumination.*

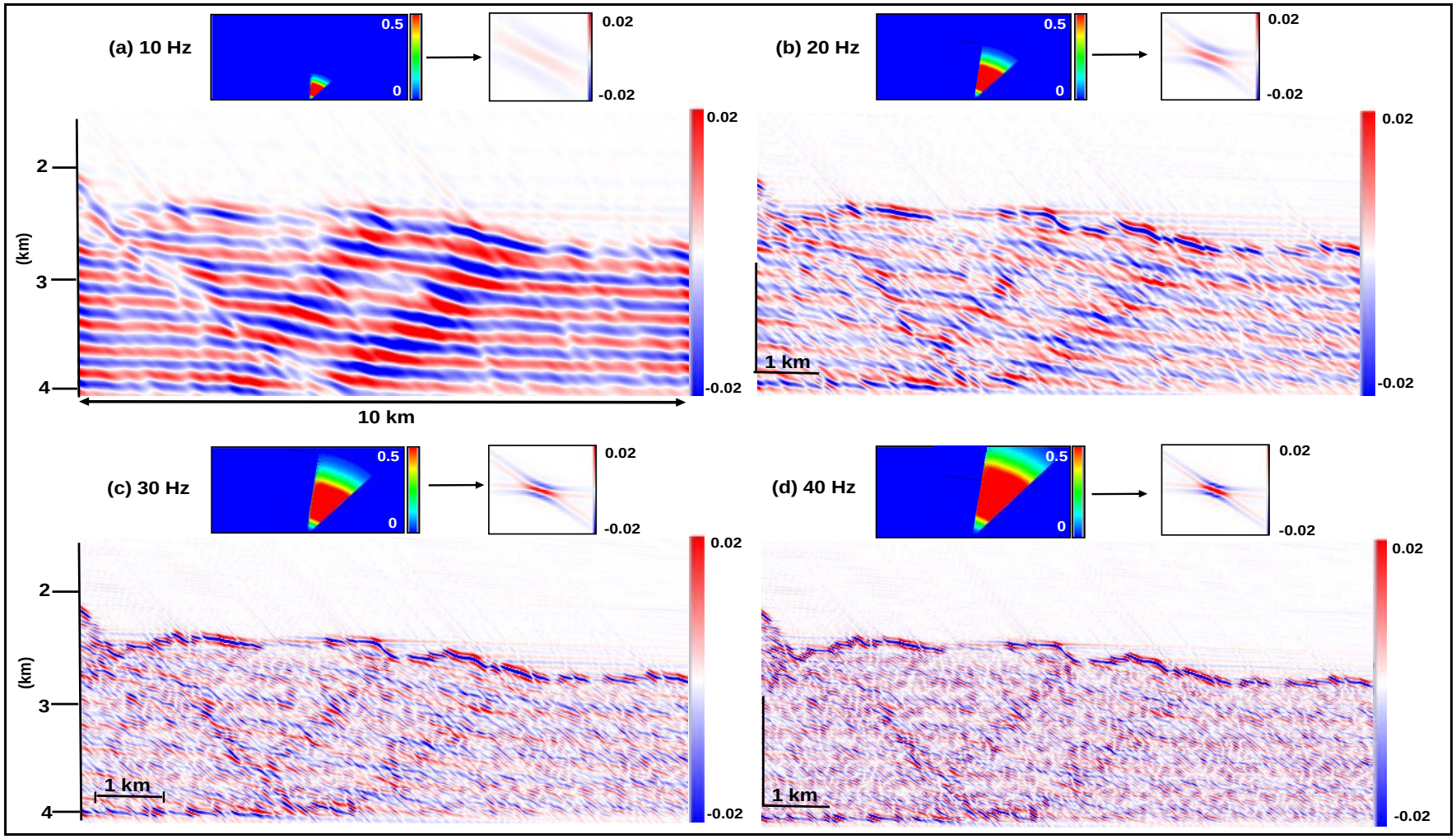

Figure 46. *PSDM seismic images of Model 2 (front of the FTB) after 5 km shortening with right-side illumination (without interpretation). The seismic images were generated with different frequencies of a zero-phase Ricker pulse: (a) 10 Hz, (b) 20 Hz, (c) 30 Hz and (d) 40 Hz. At the top of every image, their equivalent PSDM filter and resulting point spread function PSF are shown.*

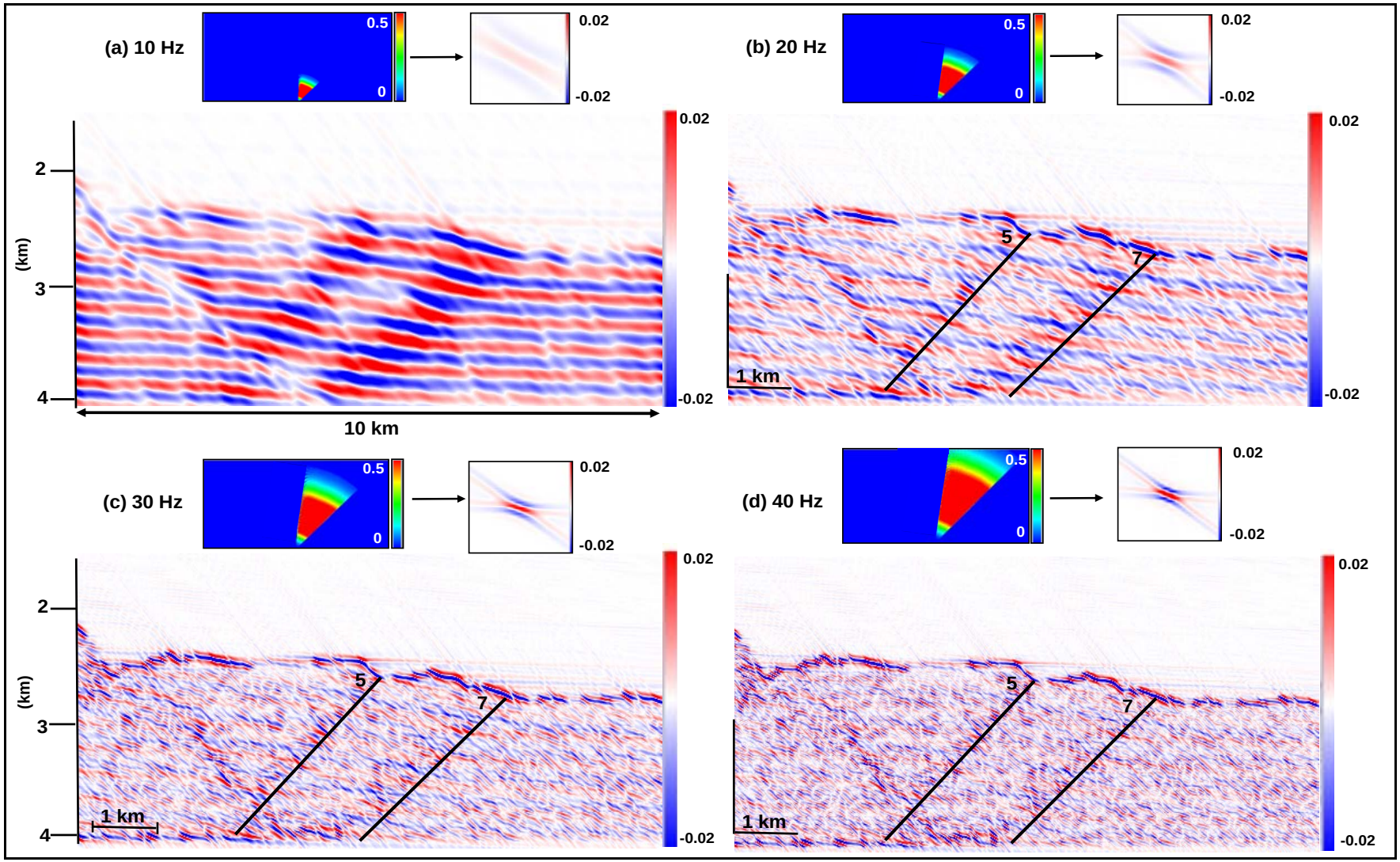

Figure 47. *Interpreted PSDM seismic images of Model 2 (front of the FTB) after 5 m shortening with right-side illumination.*

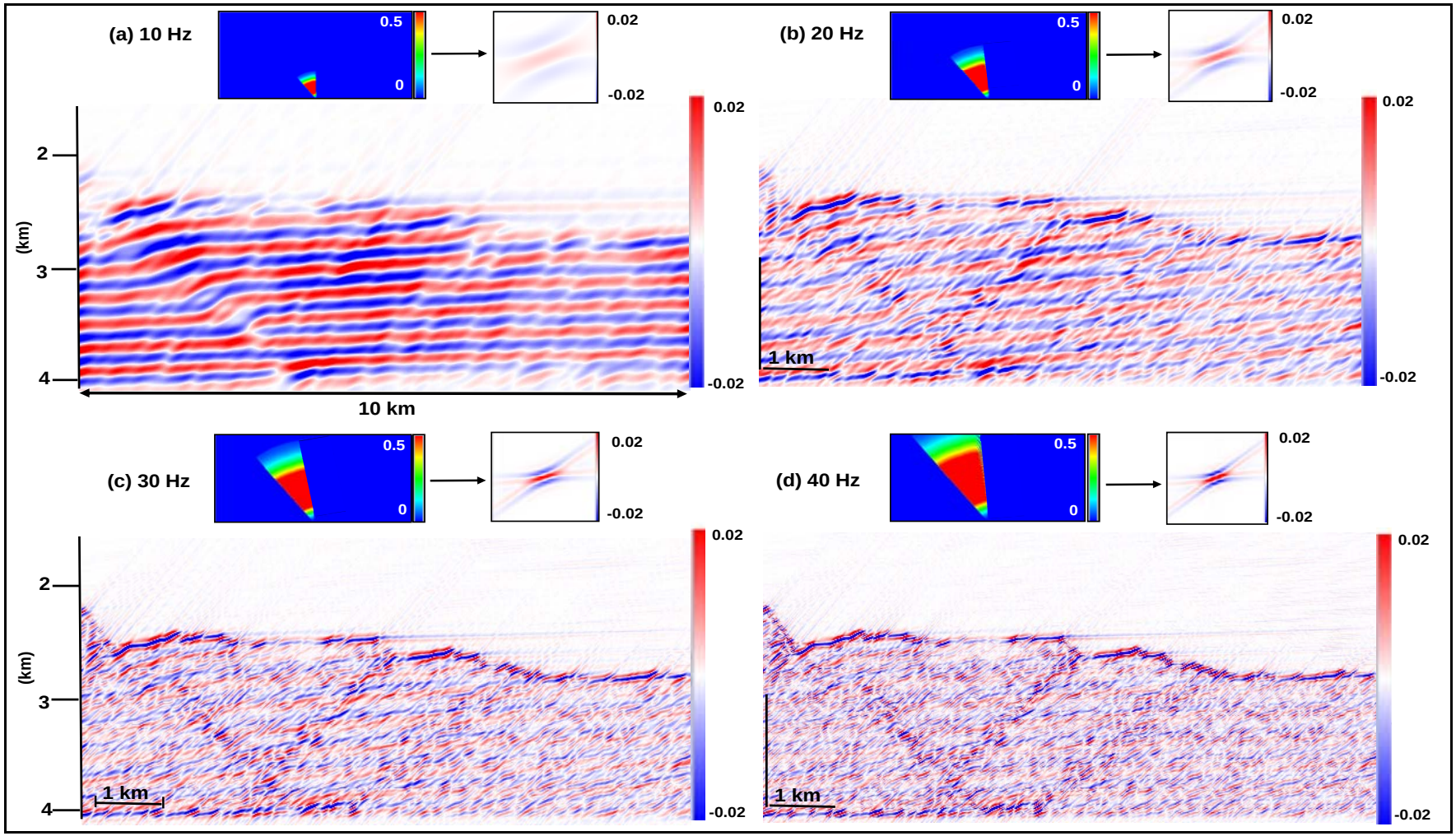

Figure 48. *PSDM seismic images of Model 2 (front of the FTB) after 5 km shortening with left-side illumination (without interpretation). The seismic images were generated with different frequencies of a zero-phase Ricker pulse: (a) 10 Hz, (b) 20 Hz, (c) 30 Hz and (d) 40 Hz. At the top of every image, their equivalent PSDM filter and resulting point spread function PSF are shown.*

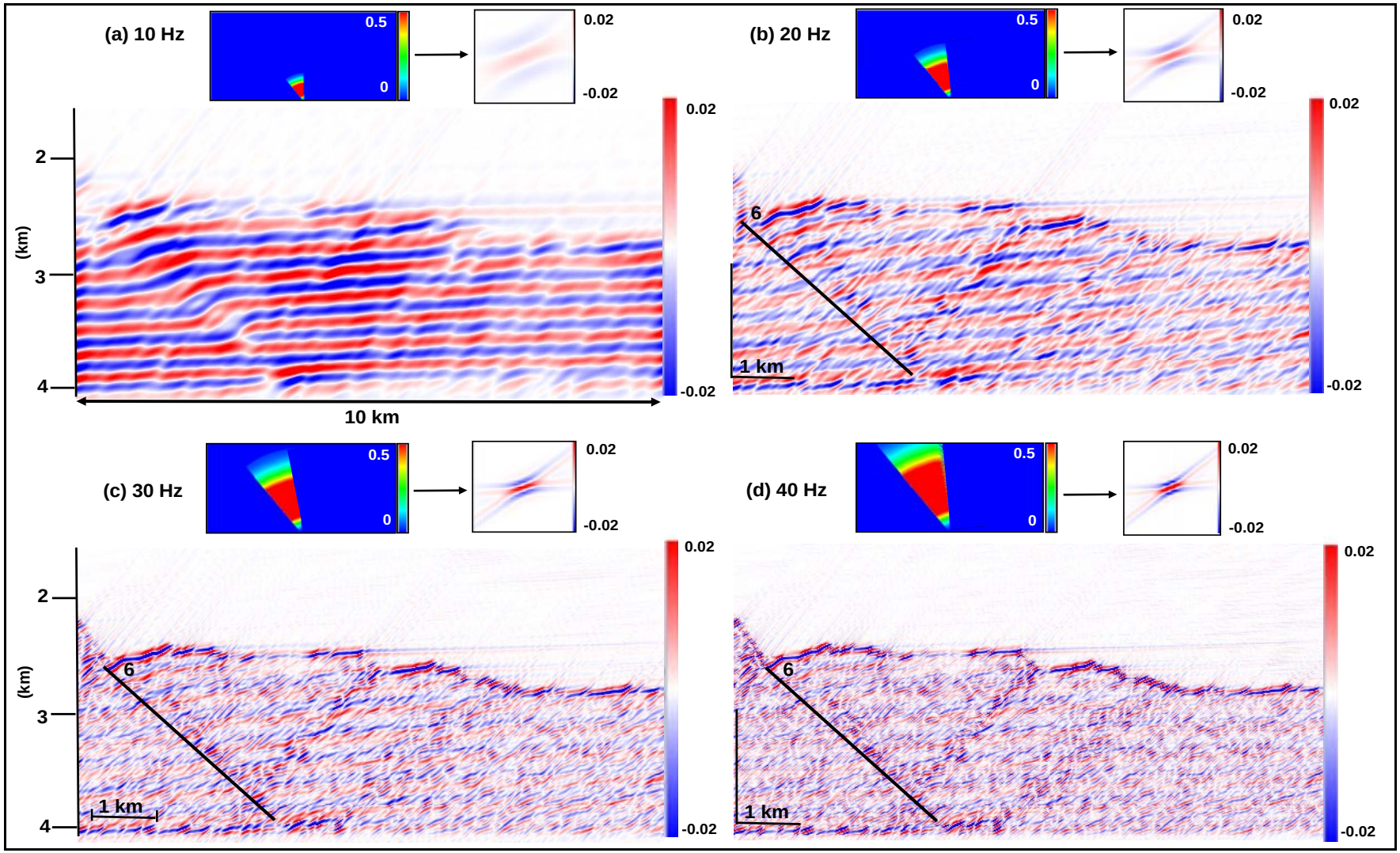

Figure 49. *Interpreted PSDM seismic images of Model 2 (front of the FTB) after 5 km shortening with left-side illumination.*

3.3.1.3 Model 3

Seismic imaging after 1 km shortening with specular illumination (Figure 50) shows images with low amplitude values for the low deformed zones in the pre-growth sedimentary sequence and the growth strata above the fold, especially at higher frequencies (30 and 40 Hz; Figure 50c-d). Besides, at these frequencies the pre-growth sedimentary sequence has no impact. Right and left side illumination (Figure 51) highlights directly zones with higher deformation corresponding to the fore- and back limbs and syn-sedimentation above the fold. However, since the evolution of the compressional fold is at the early stage, its low deformation results in less strain and therefore less impact on their seismic images, making difficult to interpret major details.

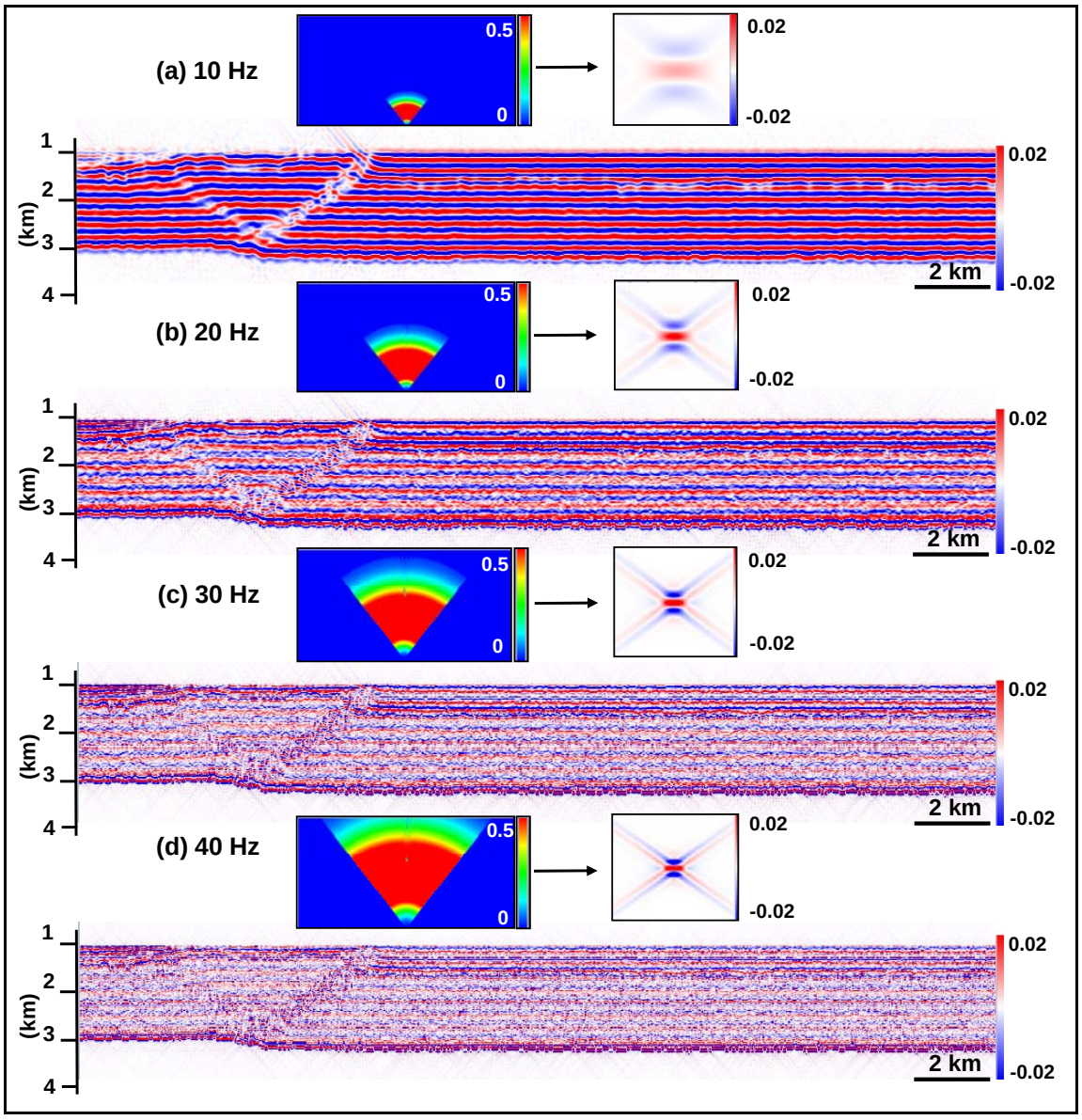

Figure 50. *PSDM seismic images of Model 3 after 1 km shortening with specular illumination. The seismic images were generated with different frequencies of a zero-phase Ricker pulse: (a) 10 Hz, (b) 20 Hz, (c) 30 Hz and (d) 40 Hz. At the top of every image, their equivalent PSDM filter and resulting point spread function PSF are shown.*

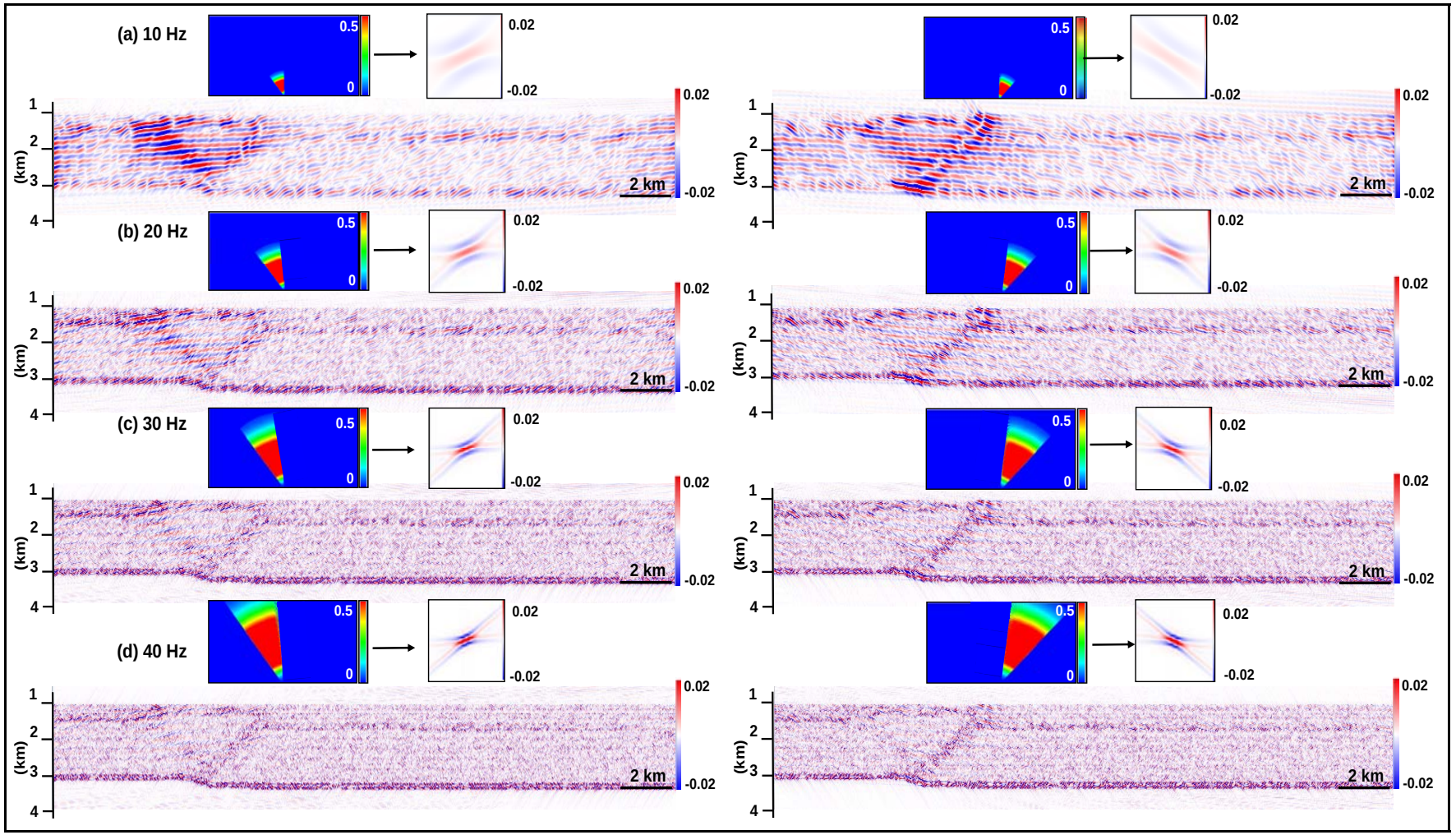

Figure 51. *PSDM seismic images of Model 3 after 1 km shortening with left (left column) and right (right column) side illuminations. The seismic images were generated with different frequencies of a zero-phase Ricker pulse: (a) 10 Hz, (b) 20 Hz, (c) 30 Hz and (d) 40 Hz. At the top of every image, their equivalent PSDM filter and resulting point spread function PSF are shown.*

On the other hand, seismic imaging after 2 km shortening with specular illumination (Figure 52) allows to have a better overview of the structure, which at this stage is more deformed, therefore more volumetric strain is accrued in the compressional fold and growth strata above it, resulting in higher resolution of these zones in the seismic images. Right and left side illumination (Figure 53) targets directly the fore- and back limbs of the fold in the pre-growth sequence and the organization and geometry of the growth strata above them. Therefore, it is possible to interpret significant details. However, the most important observations are interpreted in the seismic images after 3 km shortening, since their resolutions are higher due to the higher strain experienced at this stage.

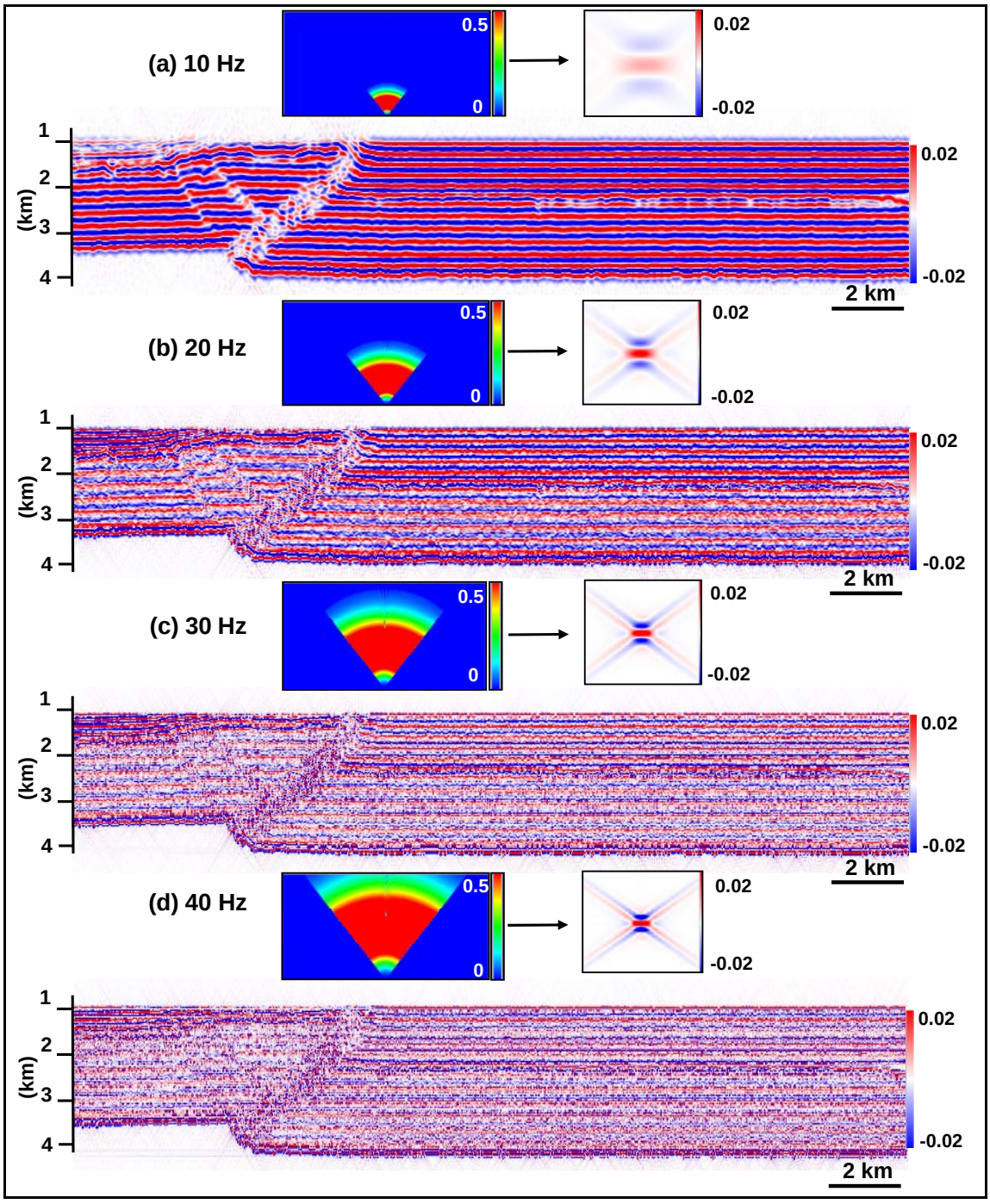

Figure 52. *PSDM seismic images of Model 3 after 2 km shortening with specular illumination. The seismic images were generated with different frequencies of a zero-phase Ricker pulse: (a) 10 Hz, (b) 20 Hz, (c) 30 Hz and (d) 40 Hz. At the top of every image, their equivalent PSDM filter and resulting point spread function PSF are shown.*

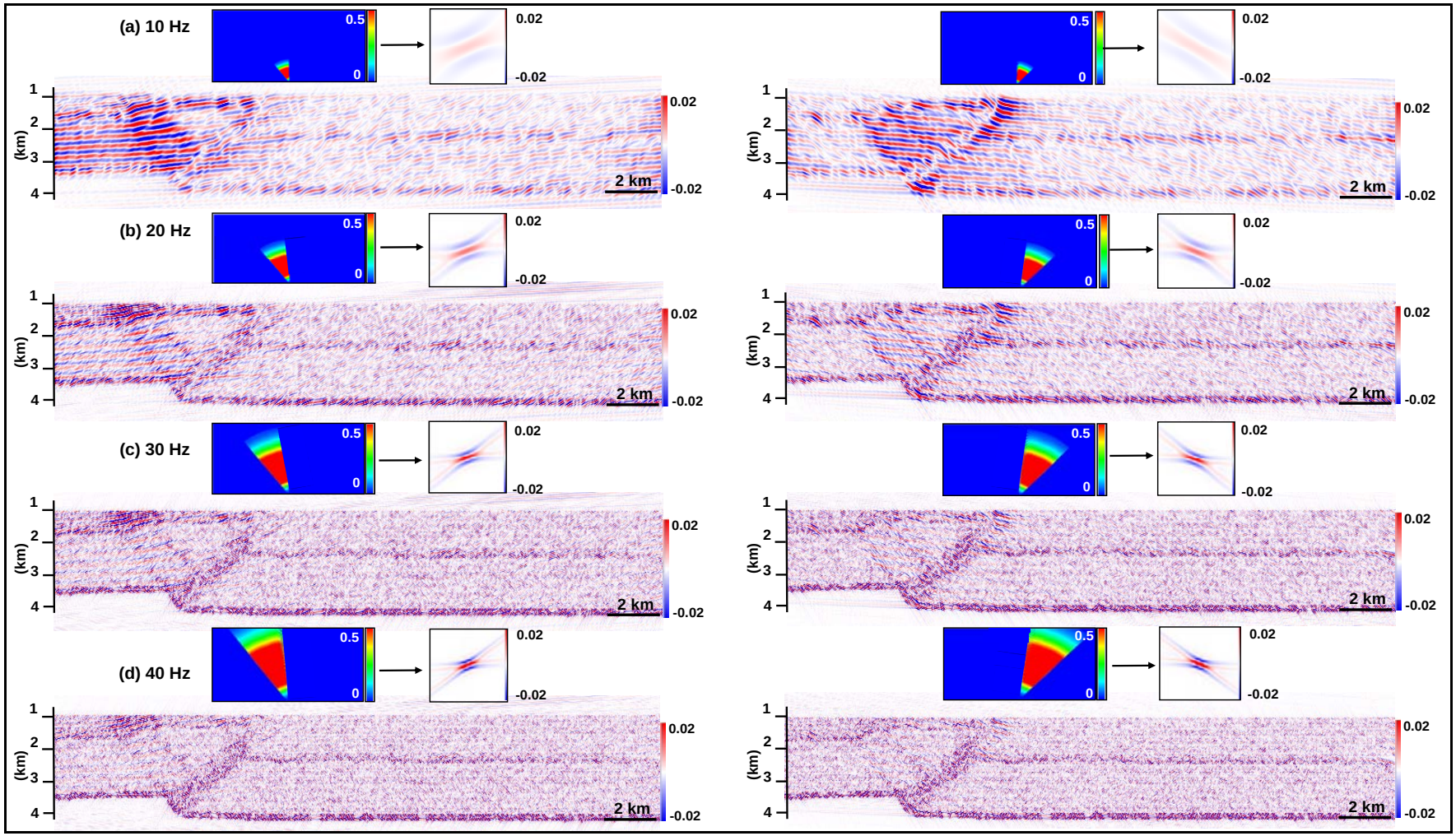

Figure 53. *PSDM seismic images of Model 3 after 2 km shortening with left (left column) and right (right column) side illuminations. The seismic images were generated with different frequencies of a zero-phase Ricker pulse: (a) 10 Hz, (b) 20 Hz, (c) 30 Hz and (d) 40 Hz. At the top of every image, their equivalent PSDM filter and resulting point spread function PSF are shown.*

Seismic imaging of Model 3 after 3 km shortening with specular illumination at 10 Hz (Figure 54-55-56a) enhances the horizontal reflectors corresponding to the pre-growth/growth sandstone/shale interfaces, outside of the complex deformed zones. Besides, the salt-siliciclastic, and the pre-growth/growth interfaces are identified. The thrusts are recognized due to the breaks and discontinuities generated in the flat reflectors. However, the steepest forelimb of the fold is hard to interpret. At higher frequencies (20, 30 and 40 Hz; Figure 54-55-56b-c-d) the diffraction energy from the steeper forelimb, results in a better characterization and the growth package above the fold is best represented (Figure 55b-c-d). As observed in Model 1 and 2 with higher frequencies, the pre-growth sandstone/shale interfaces have less impact, while in the syn-sedimentation package the different reflectivities are more remarkable. Offside illumination images only the complex fold. Right side illumination at 10 Hz (Figure 57-58a) highlights the forelimb of the fold, rather than the fore-thrusts. However, the syn-sedimentation package above the forelimb is poorly resolved. Instead higher frequencies (20, 30 and 40 Hz; Figure 57-58b-c-d) target directly the steepest hanging wall of the larger fore-thrust, from the salt-siliciclastic contact and through the pre-growth siliciclastic sequence. Besides, some diffracted energy from the back-thrusts in the core of the fold makes easier to interpret the thrusts. Furthermore, this illumination shows better the geometrical organization of the growth strata above the forelimb and towards the crest. On the other hand, left side illumination at 10 Hz (Figure 59-60a) targets directly the back-limb of the fold. Higher frequencies (20, 30 and 40 Hz; Figure 59-60b-c-d) highlight the back-thrusts and associated folds, besides the geometry and folding of the syn-sedimentation package above the back-limb. Furthermore, the diffracted energy from the steeper hanging wall of the fore-thrust can be identified, allowing better control of this area through the pre-growth sequence. Offside illumination gives high amplitude values for the most deformed zones in the fold, and syn-sedimentation sequence above, compared with the low amplitude values of the low-deformed zones around. Therefore, this illumination allows having an internal detail and better evaluation of the fore-back thrusts and related folds and syn-sedimentation above them.

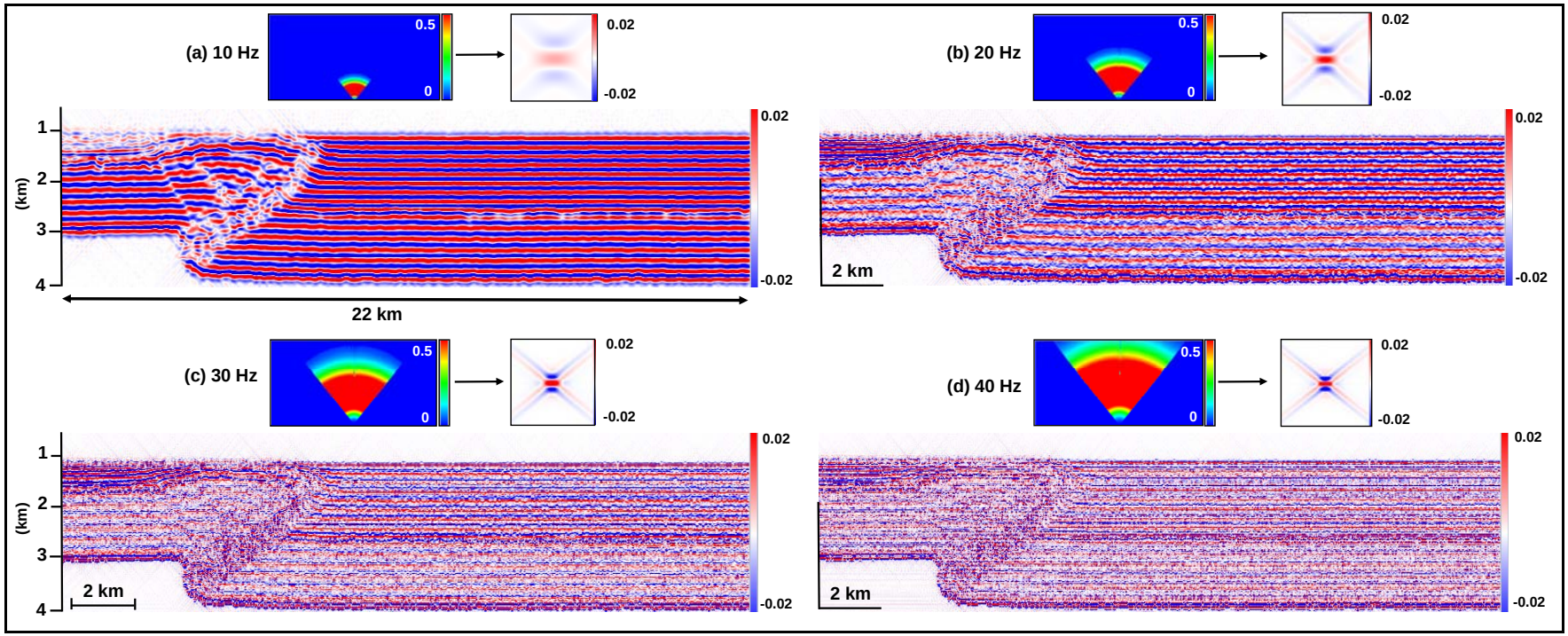

Figure 54. *PSDM seismic images of Model 3 after 3 km shortening with specular illumination (without interpretation). The seismic images were generated with different frequencies of a zero-phase Ricker pulse: (a) 10 Hz, (b) 20 Hz, (c) 30 Hz and (d) 40 Hz. At the top of every image, their equivalent PSDM filter and resulting point spread function PSF are shown.*

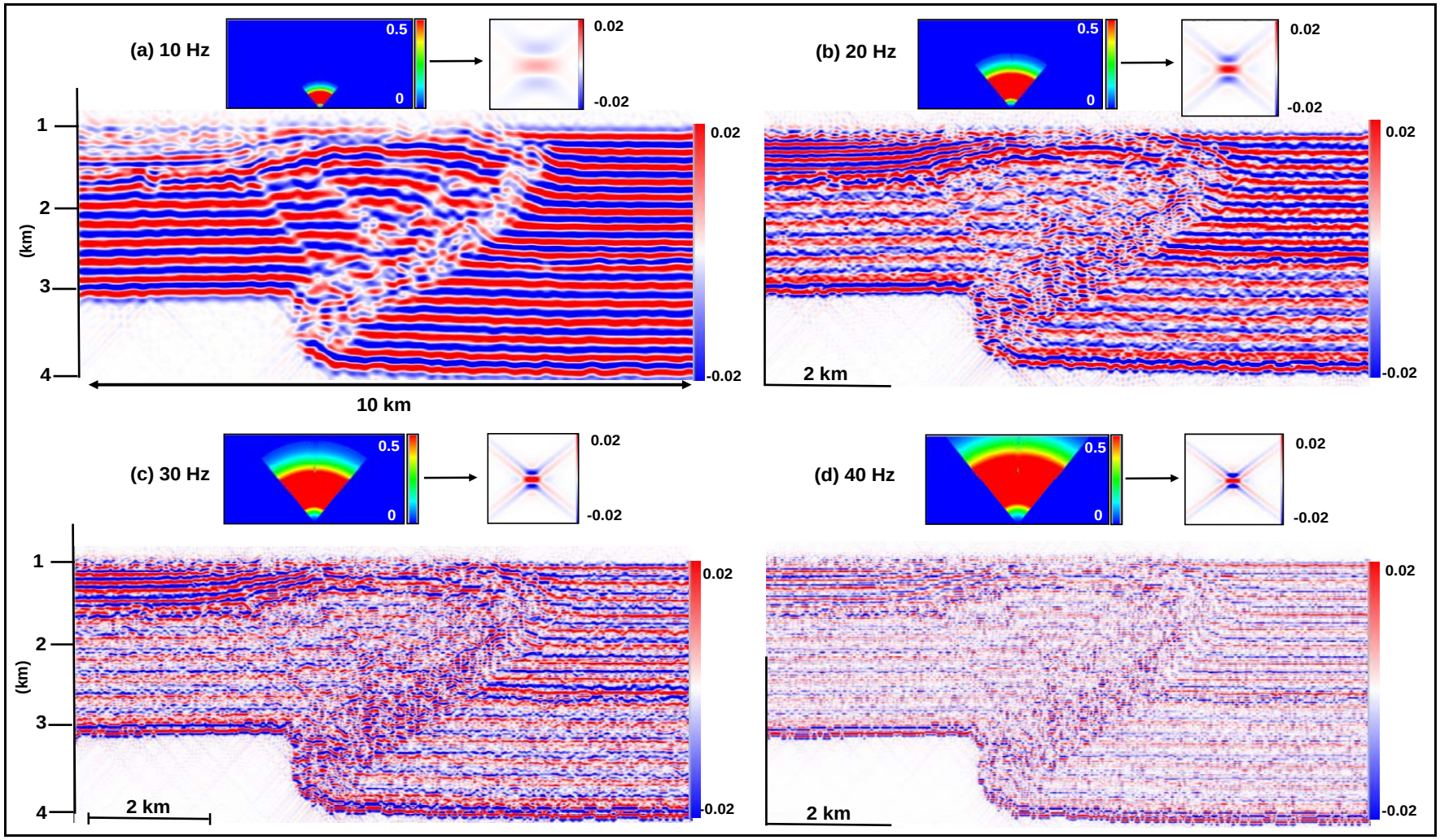

Figure 55. *PSDM seismic images of Model 3 after 3 km shortening with specular illumination (without interpretation) detailing the growth strata above the fold.*

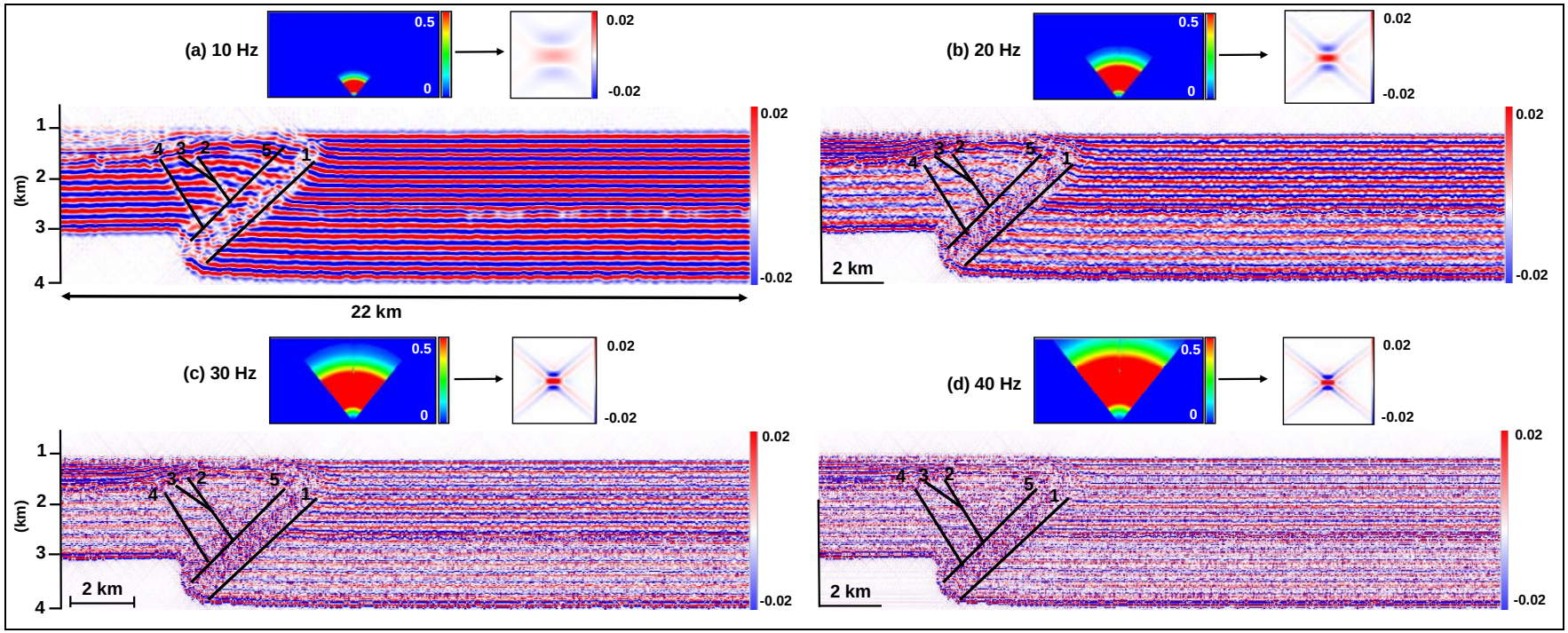

Figure 56. *Interpreted PSDM seismic images of Model 3 after 3 km shortening with specular illumination.*

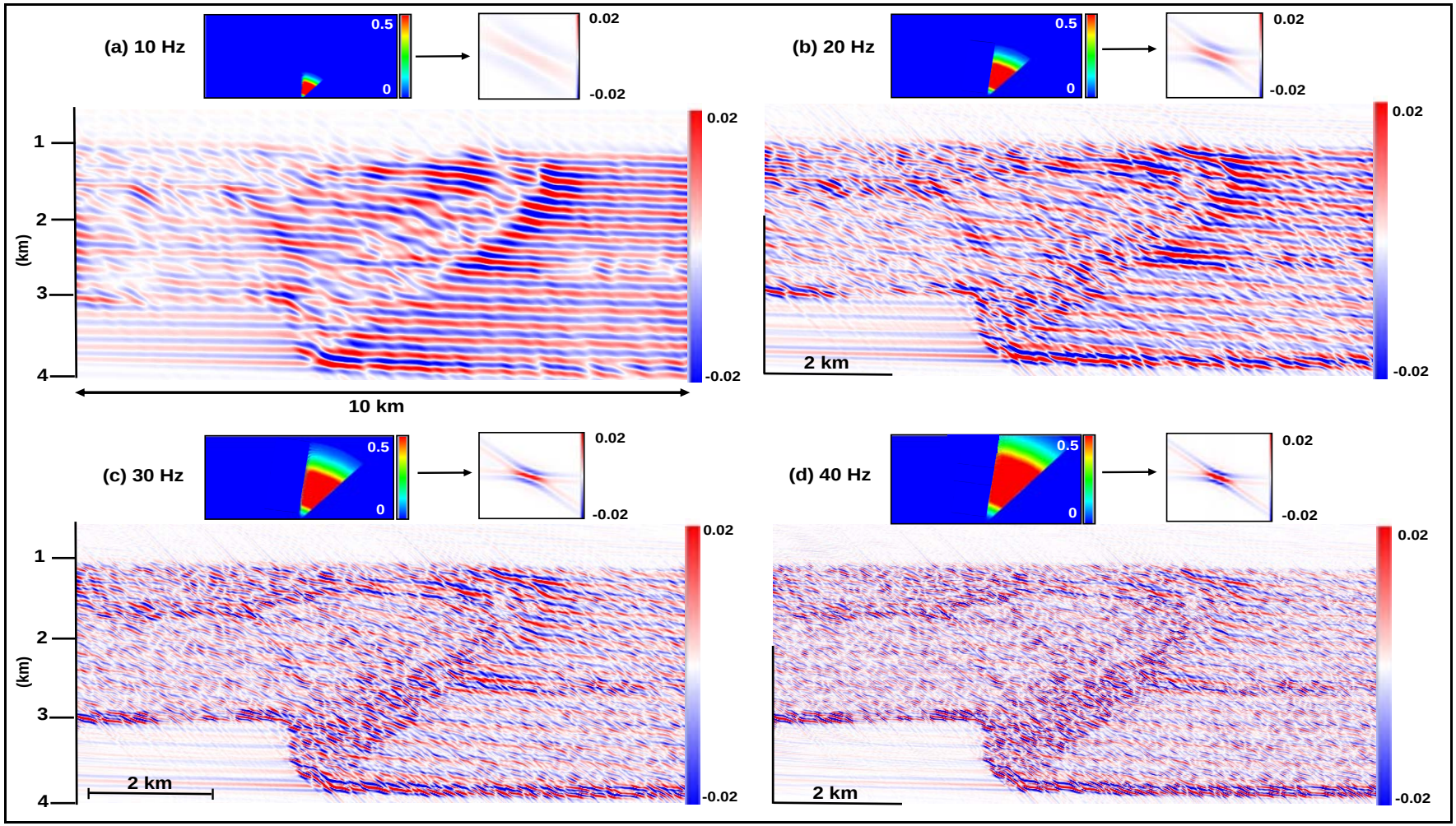

Figure 57. *PSDM seismic images of Model 3 (back of the FTB) after 3 km shortening with right-side illumination (without interpretation). The seismic images were generated with different frequencies of a zero-phase Ricker pulse: (a) 10 Hz, (b) 20 Hz, (c) 30 Hz and (d) 40 Hz. At the top of every image, their equivalent PSDM filter and resulting point spread function PSF are shown.*

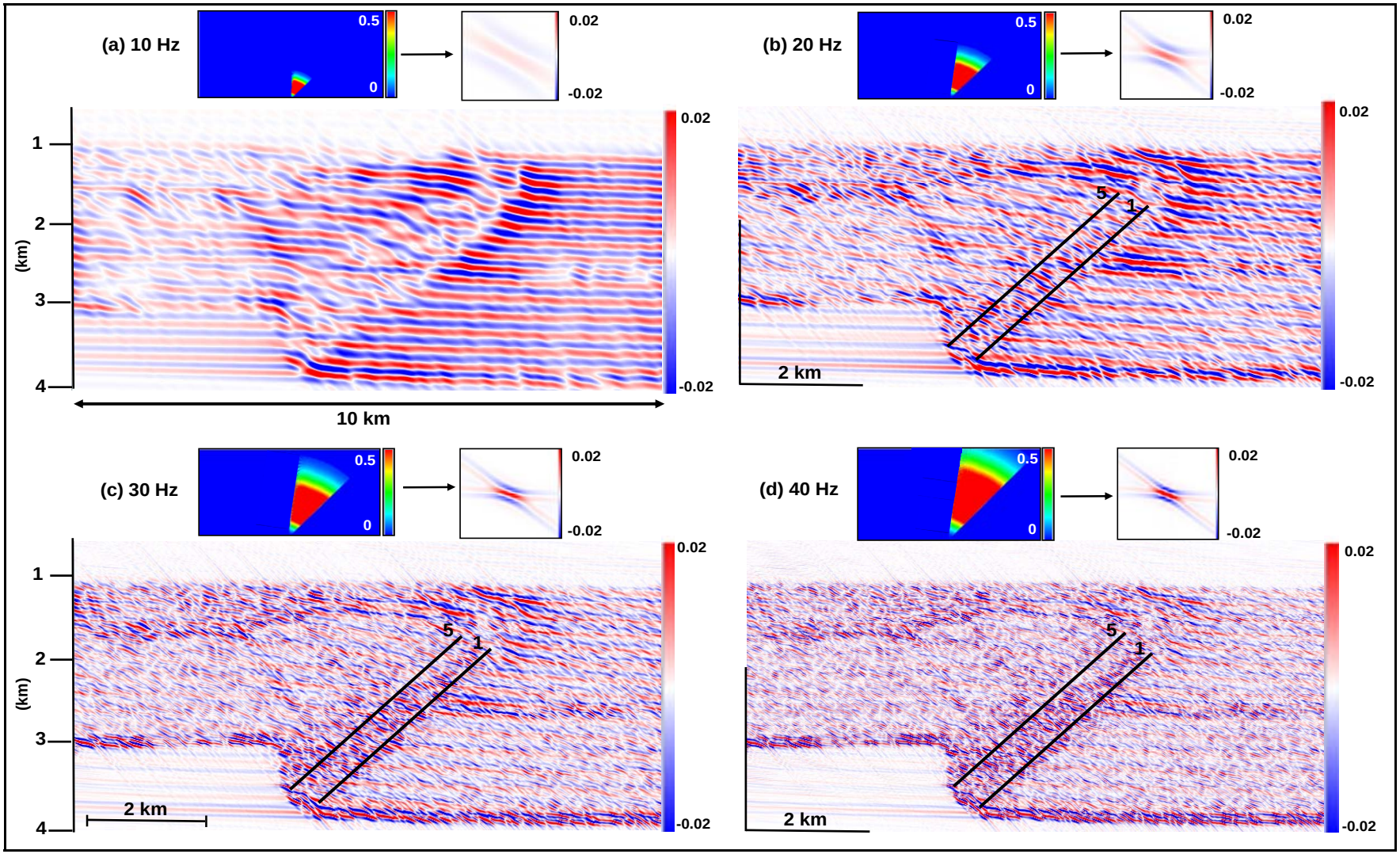

Figure 58. *Interpreted PSDM seismic images of Model 3 (back of the FTB) after 3 km shortening with right-side illumination.*

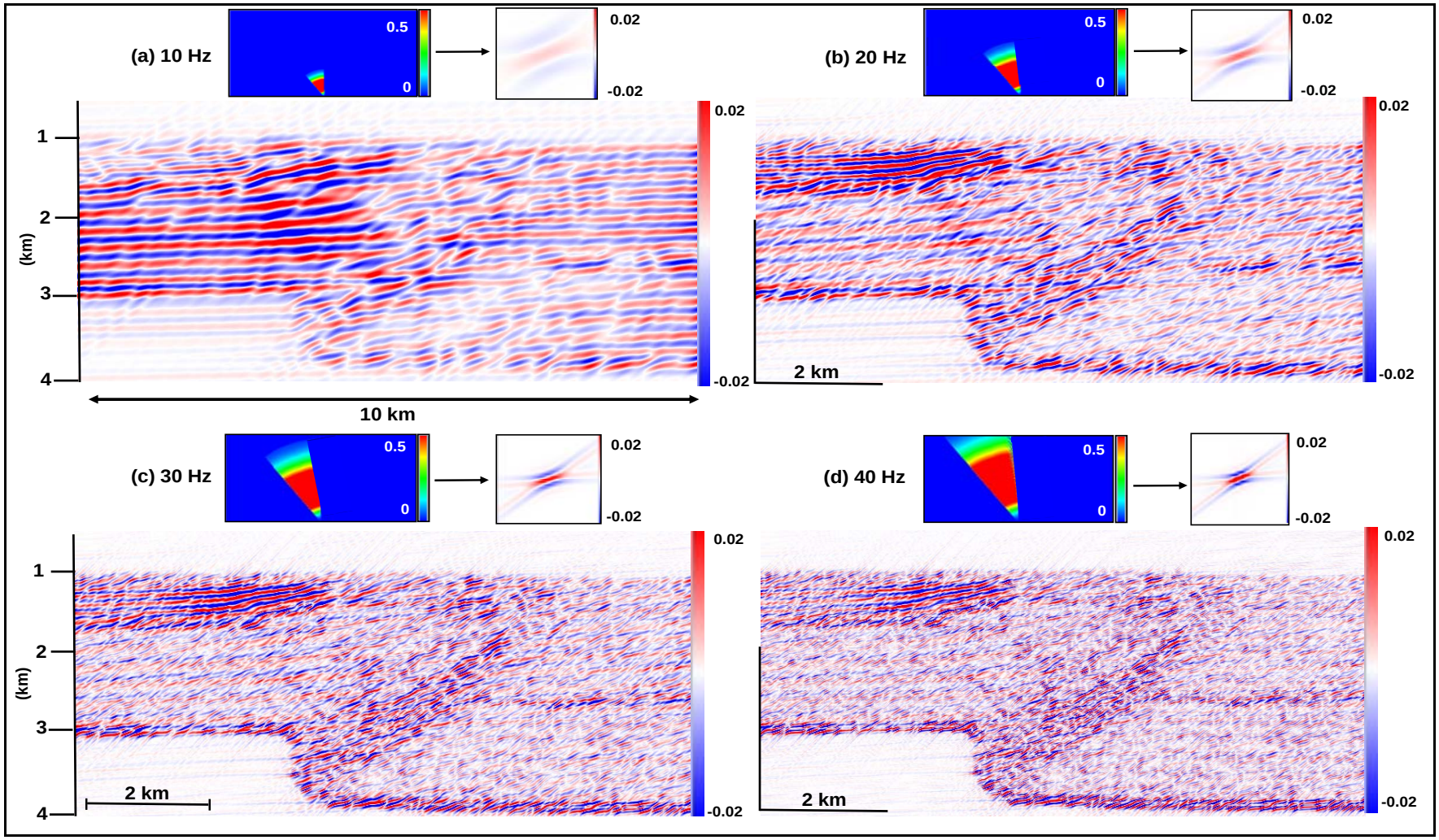

Figure 59. *PSDM seismic images of Model 3 (back of the FTB) after 3 km shortening with left-side illumination (without interpretation). The seismic images were generated with different frequencies of a zero-phase Ricker pulse: (a) 10 Hz, (b) 20 Hz, (c) 30 Hz and (d) 40 Hz. At the top of every image, their equivalent PSDM filter and resulting point spread function PSF are shown.*

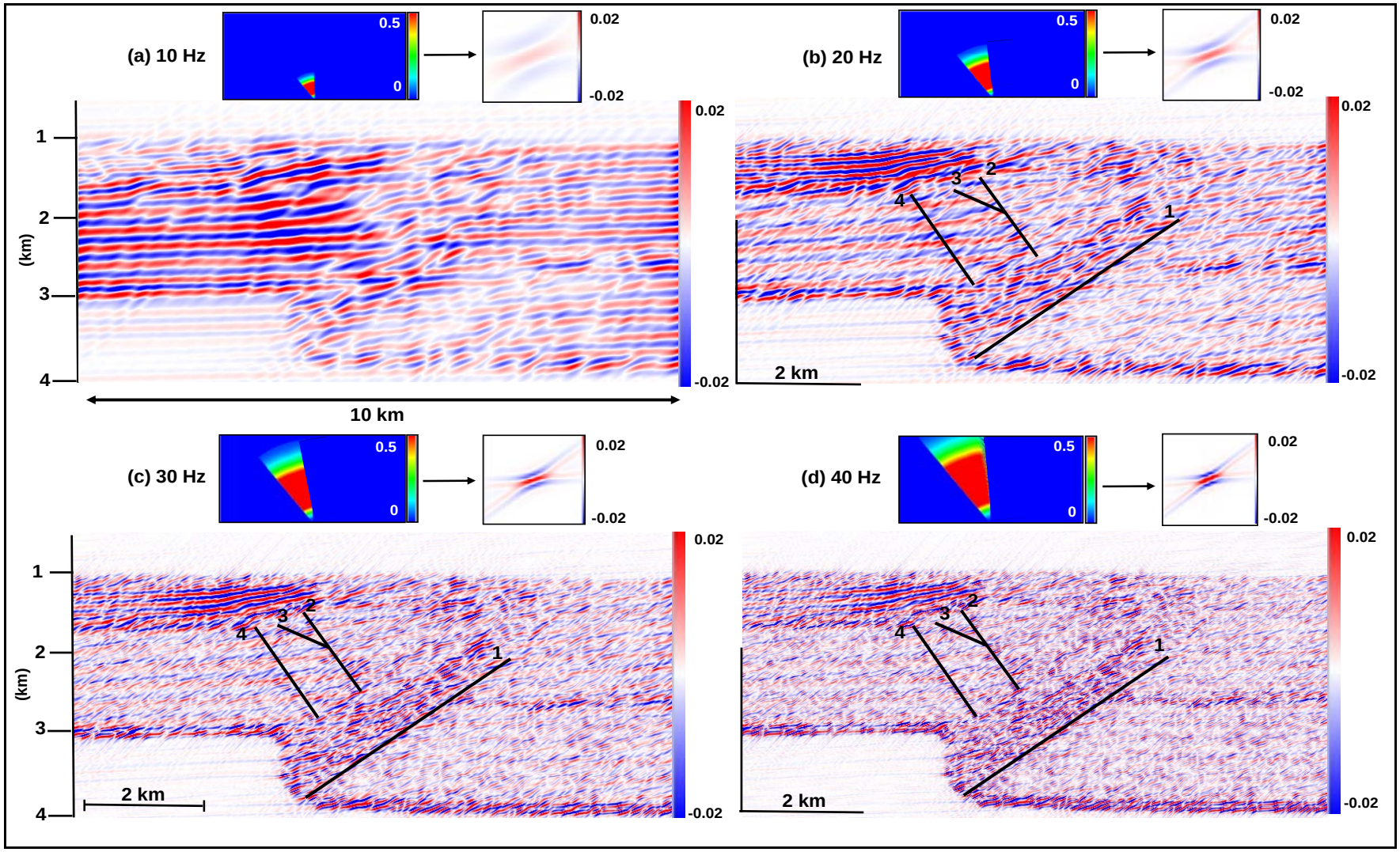

Figure 60. *Interpreted PSDM seismic images of Model 3 (back of the FTB) after 3 km shortening with left-side illumination.*

3.3.2 Impact of frequency

The seismic images at different frequencies allow seeing the variation of seismic resolution of the thrust and associated folding, and syn-sedimentation. Therefore, wave frequency becomes a fundamental parameter to capture the structural and sedimentary details, and to better interpret salt-influenced compressional folds in seismic data. Low wave frequency (10 Hz) highlights mostly horizontal reflectors corresponding to sandstone/shale interfaces in the pre-growth/growth sequence, the siliciclastic/salt, and the pre-growth/growth interfaces. Therefore, at this frequency an overview of the structure can be obtained. On the other hand, high wave frequency (20, 30 and 40 Hz) results in a better characterization and higher diffracted energy from the larger thrusts and associated folding. Hence, the geometry and internal detail of these structures is more remarkable. Additionally, at high wave frequencies the growth strata unconformity, the folding of the syn-sedimentation package above the fore-back limbs, and the thinning of growth strata towards the pre-growth crest are best represented. Furthermore, it highlights the different geometrical relations between the pre-growth and growth sequences, which become important markers that indicate the folding kinematics. On the forelimb, the lowest growth strata layers are offlapping the pre-growth sequence, and the topmost strata are progressively onlapping the fold crest towards the back-limb where no contacts are seen with the pre-growth sequence. In addition, higher wave frequency enhances the growth strata wedges above the limbs characterized by sequences of layers with a gradual reduction of the dip upwards. Also, higher wave frequencies present high amplitude values for the highly deformed thrust related zones and syn-sedimentation sequence above, making them easier to interpret.

4. Discussion simulated seismic images

Seismic imaging of compressional folds influenced by a salt layer and syn-sedimentation has been modeled to assess the impact of these variables in the resulting seismic images. The seismic modeling results constitute an important approach to evaluate which acquisition design, and processing parameters (illumination direction and wave frequency) are required for a better seismic characterization of these structures. The change of illumination direction and frequency introduced in the different seismic images nearly exemplifies the reality of seismic acquisition and processing. The parameters considered here deal already with survey geometry, wave type, background model, and overburden, and all of them have a great impact on the resulting seismic images. The different structures in the compressional folds influenced by a salt-layer (Model 2), and syn-sedimentation (Model 3) are best illuminated with the following combination (frequency and illumination direction):

1. **Thrust evaluation**: with specular illumination and 30 Hz the thrusts and associated folding are directly associated to higher diffraction on the seismic images, making them easier to interpret. However, the change of illumination direction (right/left side) results in a better definition of the thrust zones, making possible to interpret internal details and have better control of their associated deformed structures. Right side illumination targets directly the fore-thrusts and associated folds, while left side illumination highlights the back-thrusts. Additionally, offside illumination at 30 Hz produces images with high amplitudes for the thrusts and related folds. Hence, it is easier to associate the higher amplitudes with the higher diffracted energy emitted directly from these structures.

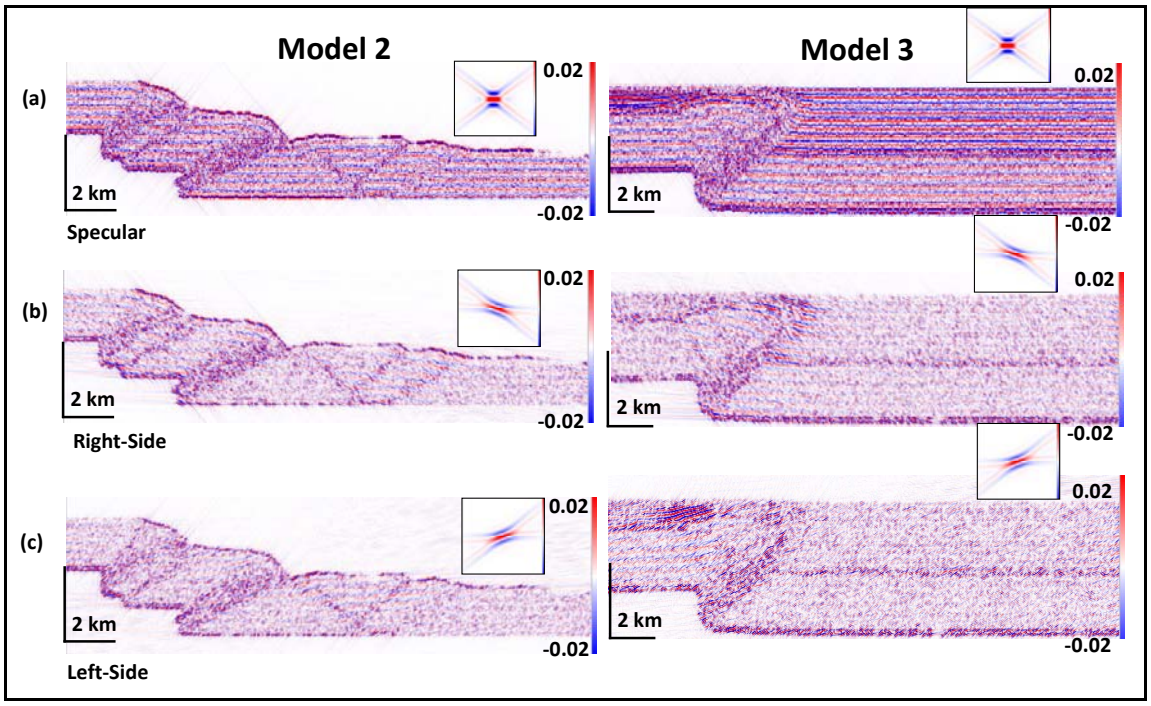

Figure 61. *Simulated PSDM seismic images at 30 Hz for Model 2 (first column) and Model 3 (second column) for (a) specular (b) right and (c) left side illumination.*

2. **Folds:** right side illumination at 10 or 30 Hz highlights the forelimbs, while left side illumination at the same frequencies targets the back-limbs (Figures 62 and 63).

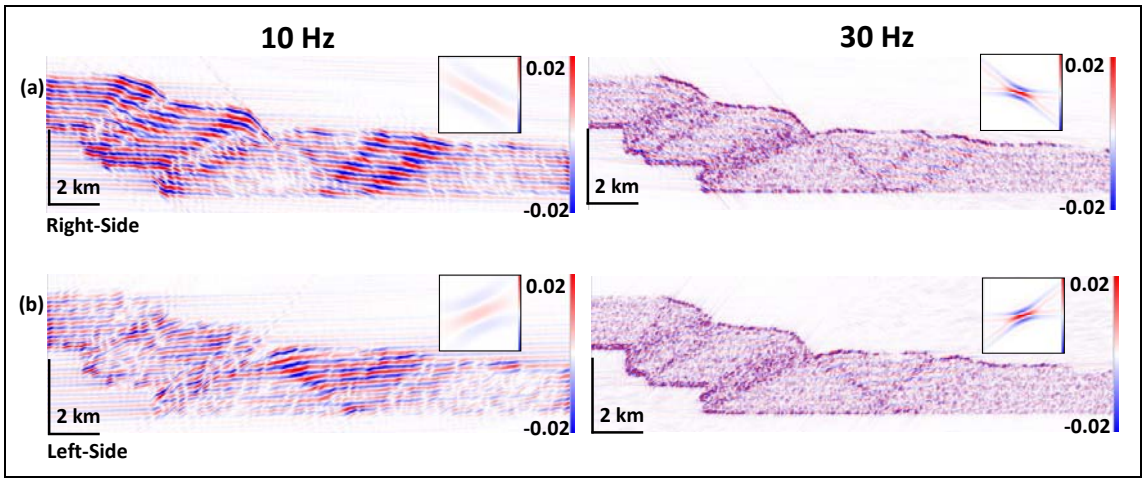

Figure 62. *Simulated PSDM seismic images for Model 2 at 10 Hz (first column) and 30 Hz (second column) for (a) right and (b) left side illumination.*

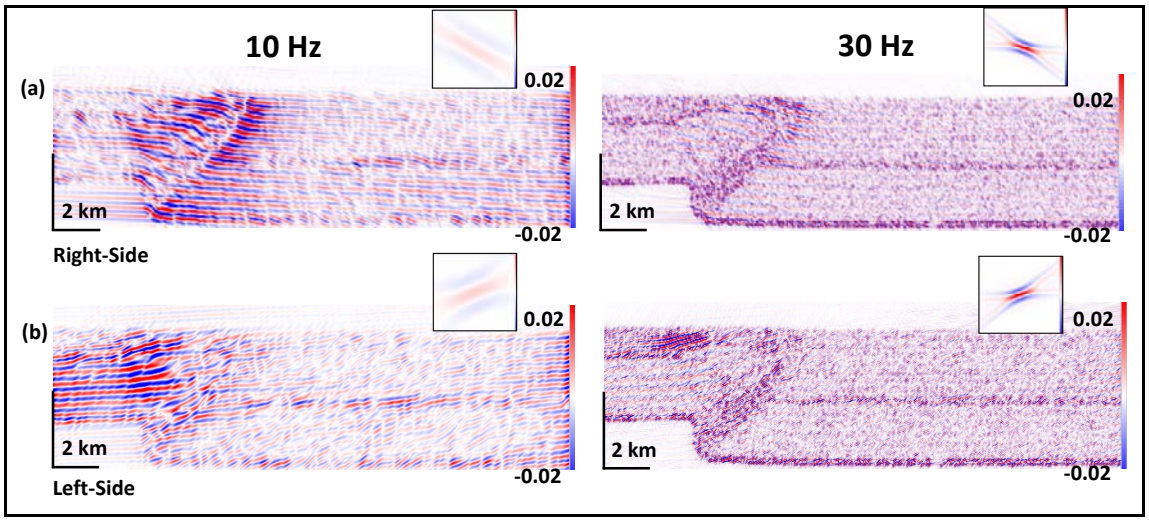

Figure 63. *Simulated PSDM seismic images for Model 3 at 10 Hz (first column) and 30 Hz (second column) for (a) right and (b) left side illumination.*

3. **Sandstone-Shale interfaces - Salt-Siliciclastic - Pre-growth-growth interfaces**: specular illumination at 10 Hz highlights the horizontal reflectors corresponding to the sandstone/shale interfaces in the pre-growth/growth sequences. Furthermore, the salt/siliciclastic, and the pre-growth/growth interfaces can be identified. Therefore, a good illustration of the structure and the sedimentary sequences involved is obtained (Figure 64).

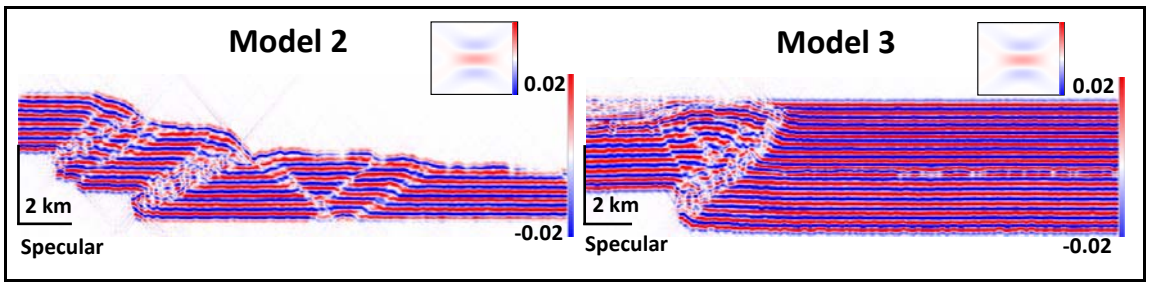

Figure 64. *Simulated PSDM seismic images with specular illumination at 10 Hz for Model 2 (first column) and Model 3 (second column).*

4. **Growth Strata**: specular illumination at 30 Hz highlights the growth strata package above the fold and the growth strata unconformity. However, the change of illumination direction (right/left side) results in a better characterization of the geometrical relationships between the pre-growth and growth sequences and the growth strata wedges. Right-side illumination at 30 Hz targets directly the onlapping and internal organization of the syn-sedimentation sequence above the

forelimb and towards the fold crest in Model 3. Instead, left-side illumination at the same frequency highlights the growth sequence above the back-limb. Furthermore, this design of parameters gives high amplitude values for these zones, which allows emphasizing the internal detail of the growth strata wedges.

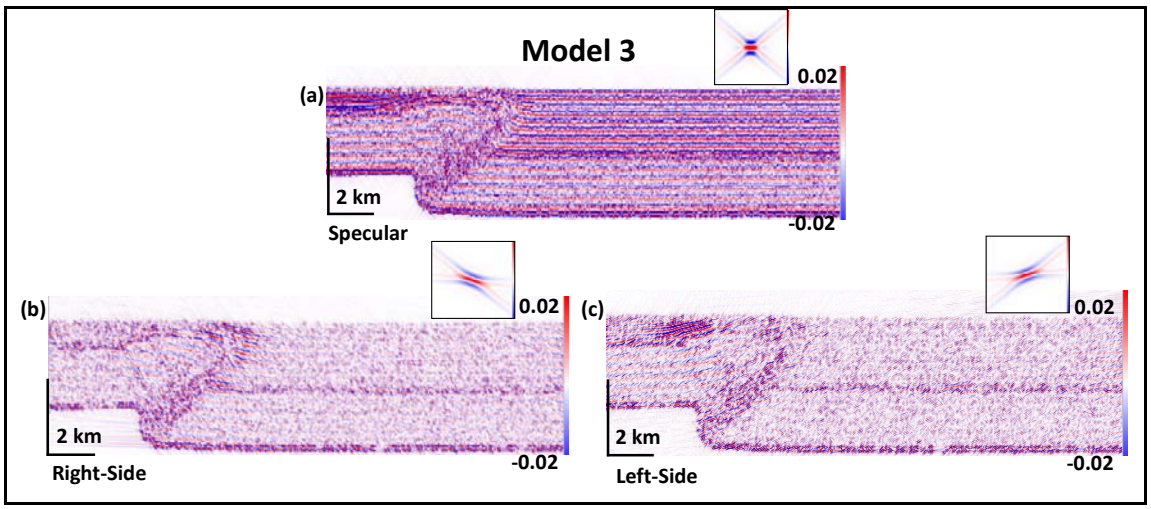

Figure 65. *Simulated PSDM seismic images at 30 Hz with (a) specular, (b) right and (c) left side illumination for Model 3.*

These combinations of two seismic parameters (illumination direction and wave frequency) give some guidelines into how seismic acquisition and processing should be handled in order to have a better control in seismic imaging and interpretation of salt-influenced compressional folds.

5. Conclusions

An integrated workflow was applied to study the evolution of salt-influenced compressional folds and their impact on seismic imaging. The mechanics and kinematics of salt-influenced compressional folds was investigated with the DEM models, which made possible to understand their structural evolution under different geological conditions such as lithology contrast, detachment rheology and syn-sedimentation. The deformation style of the compressional folds was strongly conditioned by the sedimentary sequences involved, and each assemblage produced realistic although different FTB geometries that could be used as an input to the workflow. Finite strain computation in the DEM models was used as a reliable parameter that allowed transferring the data from the geomechanical model to the seismic model, and updating the seismic properties of the DEM models based on finite strain. Since the structure and properties of the FTB were known from the DEM models, it was possible to run sensitivity analysis (illumination direction and wave frequency) with the PSDM simulator to reproduce the best properties and internal details of the structures and hence, have a better characterization of them in the seismic images. Therefore, the change of these two seismic parameters had a large impact on the resulting simulated seismic images. In all models, specular illumination highlighted the horizontal reflectors, giving an overview of the structures. Instead, right side illumination highlighted directly the fore-thrusts and associated folds, while left side illumination targeted the back-thrusts, making possible to interpret internal details of these structures. Furthermore, side illumination at 30 Hz better represented the syn-sedimentation unconformity and the geometry and internal organization of the growth strata above the fold in Model 3. On the other hand, low frequency images (10 Hz) highlighted mostly the horizontal reflectors corresponding to the sandstone/shale interfaces and the siliciclastic/salt interface, while high frequency images (30 Hz) resulted in a better characterization and higher diffracted energy from the larger thrusts and associated folding. Seismic imaging at different amount of lateral shortening, allowed seeing the impact of deformation in the resolution of the resulting seismic images. Hence, the seismic resolution in the simulated seismic images correlated with the amount of finite strain in the geomechanical models, with lower resolution (lower amplitudes) in the less deformed stages, and higher resolutions (higher amplitudes) in the more deformed ones (later stages).

Furthermore, higher amplitudes in the seismic images were associated directly to the thrusts and related folding and syn-sedimentation, which allowed to have a better characterization of these structures. This study constitutes an important approach to evaluate which acquisition design, and processing parameters (illumination direction and wave frequency) are required for a better seismic characterization of the salt influenced compressional folds, and can be used as a guideline in how seismic acquisition and processing should be handled for a proper imaging and thereby interpretation of these structures. Eventually, the workflow discussed here could be a key tool to identify and evaluate imaging problems in FTB. This methodology can be used to study other types of complex geological structures in 2D or 3D, assessing other different seismic parameters, complex scenarios such as lateral variation in overburden, and deeper structures, as those conventional seismic currently deal with.

References

Benesh, N. P., Plesch, A., Shaw, J. H., & Frost, E. K. (2007). Investigation of growth fault bend folding using discrete element modeling: Implications for signatures of active folding above blind thrust faults. *Journal of Geophysical Research: Solid Earth*, *112*(B3).

Botter, C., Cardozo, N., Hardy, S., Lecomte, I., Escalona, A., Cooke, N., & Paton, G. (2014, June). From geomechanical modelling to seismic imaging of 3D faults. In *76th EAGE Conference and Exhibition 2014*.

Botter, C., Cardozo, N., Hardy, S., Lecomte, I., & Escalona, A. (2014). From mechanical modeling to seismic imaging of faults: A synthetic workflow to study the impact of faults on seismic. *Marine and Petroleum Geology*, *57*, 187-207.

Burbidge, D. R., & Braun, J. (2002). Numerical models of the evolution of accretionary wedges and fold-and-thrust belts using the distinct-element method. *Geophysical Journal International*, *148*(3), 542-561.

Butler, R. W., Coward, M. P., Harwood, G. M., & Knipe, R. J. (1987). Salt control on thrust geometry, structural style and gravitational collapse along the Himalayan mountain front in the Salt Range of northern Pakistan. *Dynamical geology of salt and related structures. Academic Press, London*, 339-418.

Camerlo, R.H., (1998). Geometric and kinematic evolution of detachment folds, Monterrey Salient, Sierra Madre Oriental, Mexico. Ms. Thesis, University of Texas at Austin, 399pp.

Cardozo, N., Allmendinger, R. W., & Morgan, J. K. (2005). Influence of mechanical stratigraphy and initial stress state on the formation of two fault propagation folds. *Journal of Structural Geology*, *27*(11), 1954-1972.

Cardozo, N., & Allmendinger, R. W. (2009). SSPX: A program to compute strain from displacement/velocity data. *Computers & Geosciences*, *35*(6), 1343-1357.

Cobbold, P., Rossello, E., & Vendeville, B. (1989). Some experiments on interacting sedimentation and deformation above salt horizons. *Bulletin de la Société géologique de France*, (3), 453-460.

Costa, E., & Vendeville, B. C. (2002). Experimental insights on the geometry and kinematics of fold-and-thrust belts above weak, viscous evaporitic décollement. *Journal of Structural Geology*, *24*(11), 1729-1739.

Cotton, J. T., & Koyi, H. A. (2000). Modeling of thrust fronts above ductile and frictional detachments: Application to structures in the Salt Range and Potwar Plateau, Pakistan. *Geological Society of America Bulletin*, *112*(3), 351-363.

Coward, M. P., De Donatis, M., Mazzoli, S., Paltrinieri, W., & Wezel, F. C. (1999). Frontal part of the northern Apennines fold and thrust belt in the Romagna-Marche area (Italy): Shallow and deep structural styles. *Tectonics*, *18*(3), 559-574.

Cundall, P. A., & Strack, O. D. (1979). A discrete numerical model for granular assemblies. *Geotechnique*, *29*(1), 47-65.

Davis, D., Suppe, J., & Dahlen, F. A. (1983). Mechanics of fold-and-thrust belts and accretionary wedges. *Journal of Geophysical Research: Solid Earth*, *88*(B2), 1153-1172.

Davis, D. M., & Engelder, T. (1985). The role of salt in fold-and-thrust belts. *Tectonophysics*, *119*(1), 67-88.

Davis, D. M., & Engelder, T. (1987). Thin-skinned deformation over salt. *Dynamical geology of salt and related structures*, 301-337.

Davis, D. M., & Lillie, R. J. (1994). Changing mechanical response during continental collision: active examples from the foreland thrust belts of Pakistan. *Journal of Structural Geology*, *16*(1), 21-34.

Dixon, J. M., & Liu, S. (1992). Centrifuge modelling of the propagation of thrust faults. In *Thrust tectonics* (pp. 53-69). Springer Netherlands.

Egholm, D. L., Clausen, O. R., Sandiford, M., Kristensen, M. B., & Korstgård, J. A. (2008). The mechanics of clay smearing along faults. *Geology*, *36*(10), 787-790.

Finch, E., Hardy, S., & Gawthorpe, R. (2003). Discrete element modelling of contractional fault-propagation folding above rigid basement fault blocks. *Journal of Structural Geology*, *25*(4), 515-528.

Finch, E., Hardy, S., & Gawthorpe, R. (2004). Discrete-element modelling of extensional fault-propagation folding above rigid basement fault blocks. *Basin research*, *16*(4), 467-488.

Fischer, M. P., & Jackson, P. B. (1999). Stratigraphic controls on eformation patterns in fault-related folds: a detachment fold example from the Sierra Madre Oriental, northeast Mexico. *Journal of Structural Geology*, *21*(6), 613-633.

Fossen, H. (2010). *Structural geology*. Cambridge University Press.

Gjøystdal, H., Iversen, E., Lecomte, I., Kaschwich, T., Drottning, Å., & Mispel, J. (2007). Improved applicability of ray tracing in seismic acquisition, imaging, and interpretation. *Geophysics*, *72*(5), SM261-SM271.

Goffey, G. P., Craig, J., Needham, T., & Scott, R. (2010). Fold–thrust belts: overlooked provinces or justifiably avoided?. *Geological Society, London, Special Publications*, *348*(1), 1-6.

Gray, G. G., Morgan, J. K., & Sanz, P. F. (2014). Overview of continuum and particle dynamics methods for mechanical modeling of contractional geologic structures. *Journal of Structural Geology*, *59*, 19-36.

Hardy, S., & Finch, E. (2005). Discrete-element modelling of detachment folding. *Basin Research*, *17*(4), 507-520.

Hardy, S., & Finch, E. (2006). Discrete element modelling of the influence of cover strength on basement-involved fault-propagation folding. *Tectonophysics*, *415*(1), 225-238.

Hardy, S., & Finch, E. (2007). Mechanical stratigraphy and the transition from trishear to kink-band fault-propagation fold forms above blind basement thrust faults: a discrete-element study. *Marine and Petroleum Geology*, *24*(2), 75-90.

Hardy, S., McClay, K., & Muñoz, J. A. (2009). Deformation and fault activity in space and time in high-resolution numerical models of doubly vergent thrust wedges. *Marine and Petroleum Geology*, *26*(2), 232-248.

Hardy, S. (2013). Propagation of blind normal faults to the surface in basaltic sequences: Insights from 2D discrete element modelling. *Marine and Petroleum Geology*, *48*, 149-159.

Harrison, J. C., & Bally, A. W. (1988). Cross-sections of the Parry Islands fold belt on Melville Island, Canadian Arctic Islands: implications for the timing and kinematic history of some thin-skinned décollement systems. *Bulletin of Canadian Petroleum Geology*, *36*(3), 311-332.

Harrison, J. C. (1995). Tectonics and kinematics of a foreland folded belt influenced by salt, Arctic Canada.

Holt, R. M., Fjær, E., Nes, O. M., & Stenebraten, J. F. (2008). Strain sensitivity of wave velocities in sediments and sedimentary rocks. In *The 42nd US Rock Mechanics Symposium (USRMS)*. American Rock Mechanics Association.

Hudec, M. R., & Jackson, M. P. (2012). De Re Salica: Fundamental principles of salt tectonics. *Regional Geology and Tectonics: Phanerozoic Passive Margins, Cratonic Basins and Global Tectonic Maps: Phanerozoic Passive Margins, Cratonic Basins and Global Tectonic Maps*, 19.

Huiqi, L., McClay, K. R., & Powell, D. (1992). Physical models of thrust wedges. In *Thrust tectonics* (pp. 71-81). Springer Netherlands.

Jackson, M. P. A., & Talbot, C. J. (1991). *A glossary of salt tectonics*. Bureau of Economic Geology, University of Texas at Austin.

Jackson, M. P., Vendeville, B. C., & Schultz-Ela, D. D. (1994). Structural dynamics of salt systems. *Annual Review of Earth and Planetary Sciences*, *22*, 93-117.

Jaumé, S. C., & Lillie, R. J. (1988). Mechanics of the Salt Range-Potwar Plateau, Pakistan: A fold-and-thrust belt underlain by evaporites. *Tectonics*, *7*(1), 57-71.

Koyi, H. (1988). Experimental modeling of role of gravity and lateral shortening in Zagros mountain belt. *AAPG Bulletin*, *72*(11), 1381-1394.

Koyi, H. (1998). Modeling the role of gravity and lateral shortening in the Zagros mountain belt. *American Association of Petroleum Geologists Bulletin*, *72*, 1381-1394.

Laubscher, H. P. (1961). Die fernschubhypothese der jurafaltung. *Eclogae Geologicae Helvetiae*, *54*(1), 222-282.

Laubscher, H. P. (1977). Fold development in the Jura. *Tectonophysics*, *37*(4), 337-362.

Lecomte, I. (2008). Resolution and illumination analyses in PSDM: A ray-based approach. *The Leading Edge*, *27*(5), 650-663.

Letouzey, J., Colletta, B., Vially, R., & Chermette, J. C. (1995). Evolution of salt-related structures in compressional settings, in Jackson, M. P. A., Roberts, D. G., and Snelson, S., eds., Salt tectonics: A global perspective: American Association of Petroleum Geologists Memoir 65, p. 41–60.

Marrett, R. A. (1999). Stratigraphy and structure of the Jurassic and Cretaceous platform and basin systems of the Sierra Madre Oriental: a field book and related papers. *South Texas Geological Society*, 121.

Mascle, J., Huguen, C., Benkhelil, J., Chamot-Rooke, N., Chaumillon, E., Foucher, J. P., ... & Woodside, J. (1999). Images may show start of European-African plate collision. *EOS, Transactions American Geophysical Union*, *80*(37), 421-428.

Mavko, G., Mukerji, T., & Dvorkin, J. (2009). *The rock physics handbook: Tools for seismic analysis of porous media*. Cambridge university press.

Mitra, S., & Fisher, G. W. (1992). *Structural geology of fold and thrust belts*. Johns Hopkins Univ Pr.

Mora, P., & Place, D. (1993). A lattice solid model for the nonlinear dynamics of earthquakes. *International Journal of Modern Physics C*, *4*(06), 1059-1074.

Philippe, Y., Colletta, B., Deville, E., & Mascle, A. (1996). The Jura fold-and-thrust belt: a kinematic model based on map-balancing. *Mémoires du Muséum national d'histoire naturelle*, *170*, 235-261.

Rowan, M. G., Peel, F. J., & Vendeville, B. C. (2004). Gravity-driven fold belts on passive margins.

Schöpfer, M. P., Childs, C., & Walsh, J. J. (2006). Localisation of normal faults in multilayer sequences. *Journal of Structural Geology*, *28*(5), 816-833.

Schöpfer, M.P.J., Childs, C., Walsh, J.J., Manzocchi, T. & Koyi, H.A. (2007a). Geometrical analysis of the refraction and segmentation of normal faults in periodically layered sequences. Journal of Structural Geology 29, 318-335.

Schöpfer, M.P.J., Childs, C. & Walsh, J.J. (2007b). 2D Distinct Element modeling of the structure and growth of normal faults in multilayer sequences. Part 1: Model

calibration, boundary conditions and selected results. Journal of Geophysical Research 112, B10401.

Sigernes, L. T. W. (2004). Rock Physics of extensional Faults and their seismic imaging Properties.

Skurtveit, E., Torabi, A., Gabrielsen, R. H., & Zoback, M. D. (2013). Experimental investigation of deformation mechanisms during shear-enhanced compaction in poorly lithified sandstone and sand. *Journal of Geophysical Research: Solid Earth*, *118*(8), 4083-4100.

Stephanescu, M., Dicea, O., & Tari, G. (2000). Influence of extension and compression on salt diapirism in its type area, East Carpathians Bend area, Romania. *Geological Society, London, Special Publications*, *174*(1), 131-147.

Strayer, L. M., & Suppe, J. (2002). Out-of-plane motion of a thrust sheet during along-strike propagation of a thrust ramp: a distinct-element approach. *Journal of Structural Geology*, *24*(4), 637-650.

Strayer, L. M., Erickson, S. G., & Suppe, J. (2004). Influence of growth strata on the evolution of fault-related folds—distinct-element models.

Vidal-Royo, O., Hardy, S., & Muñoz, J. A. (2011). The roles of complex mechanical stratigraphy and syn-kinematic sedimentation in fold development: insights from discrete-element modelling and application to the Pico del Águila anticline (External Sierras, Southern Pyrenees). *Geological Society, London, Special Publications*, *349*(1), 45-60.

Von Huene, R. (1997). Mediterranean Ridge structure: results from IMERSE. *Eos, Transactions American Geophysical Union*, *78*(15), 155.